FACULTY OF SCIENCE AND TECHNOLOGY

MASTER'S THESIS

Study programme / specialisation: Marine and Offshore Technology	Spring semester, 2023 Open
Author: Onur Aydemir	
Supervisor at UiS: Prof. Muk Chen Ong Co-supervisor: Dr. Hui Cheng	
Thesis title: Numerical Investigations on the Layout Design of Open Cage Fish Farm	
Credits: 30 ECTS	
Keywords: Wake effect, Dynamic porous media model, Screen model, Fluid-structure interaction, Finite volume method, Finite element method Aquaculture structure, Fish farm.	Pages: 94 Stavanger, June 15. 2023

Approved by the Dean 30 Sep 21
Faculty of Science and Technology

Abstract

Aquaculture, one of the fastest-growing food production method, has become Norway's second-largest export industry in the past decades. In Norway, the high-value fish like Atlantic Salmon are usually raised in multi-cage fish farms. In the design of these fish farms, the unknown flow velocities within the farm make it difficult to estimate the drag forces on individual cages, thereafter the loads on mooring system. Additionally, as fish farms move to open seas for better environments, fish cages face increased loads from larger waves and faster currents, leading to higher tension in mooring lines and reduced cultivation volume. Addressing these challenges is crucial for optimizing aquaculture system design.

This thesis mainly focuses on the two key issues: the environmental load on downstream fish cages and the structural responses of two different layout designs of fish farms.

The first part of the thesis investigates wake effects on drag forces on fish cages using CFD and a porous medium model. Different cage placements and solidities are considered in the investigation. One interesting finding is that downstream fish cages can experience higher drag forces than upstream cages, particularly when positioned between $\alpha = 30°$ and $\alpha = 70°$. Additionally, higher solidity will increase drag forces on fish cages. These findings can improve the understanding of the wake effects inside of multi-cage fish farms.

The second part of this thesis presents investigates the fluid-structure interaction in fish farms using a coupling algorithm that combines OpenFOAM and Code_Aster. This part mainly focuses on the structural responses and flow fields of a 2×3 Array layout and a new Honeycomb layout design. The study compares flow characteristics, anchor line tensions, drag forces, and cultivation volumes under different flow angles. Results suggest that the Honeycomb layout offers a smaller covered area in the sea, reduced environmental loads, and improved operational efficiency, making it an advantageous approach for fish farming.

Acknowledgements

I would like to express my heartfelt gratitude to my main supervisor and mentor, Prof. Muk Chen Ong, for his unwavering guidance and support throughout my entire master's study. His consistent direction and inspiration motivated me to strive for excellence.

I would also like to extend my appreciation to my co-supervisor, Dr. Hui Cheng, for his invaluable motivation and mentoring. His prompt responses and willingness to address my questions played a crucial role in my research progress. I am sincerely grateful for the time and effort he dedicated to providing me with guidance and feedback. His dedication to academic work has been truly inspiring.

I would also like to acknowledge Theodor Ivesdal for his IT support in the school cluster, which was instrumental in facilitating my research.

Lastly, I am deeply grateful to my family for their unconditional support and encouragement throughout my study. Their constant presence and belief in me have been invaluable.

As I reflect on this journey, I am reminded of the wise words of Atatürk: "The supreme guide in life is science." This quote has always served as a guiding light, inspiring me to pursue knowledge and embrace the power of scientific inquiry. It has fueled my passion for research and motivated me to explore new frontiers in my field of study.

Contents

List of Figures

List of Tables

Chapter 1

Introduction

1.1 Background and motivation

Aquaculture has grown in importance as a result of a variety of factors, including rising seafood demand, diminishing wild fish sources, and technological and production breakthroughs (Skettring, 2023; ASC-Aqua, 2023). Despite the economic and nutritional advantages of aquaculture, there are still several difficulties with it, including disease outbreaks, environmental effects, and social and economic problems in developing nations (EarthournEtwork, 2023). Aquaculture is a important source of protein and necessary nutrients for people, especially in underdeveloped countries where fish is a key source of animal protein. Additionally, aquaculture helps to the economic growth of coastal communities, alleviating poverty and boosting food security as a substantial employer and source of revenue (FAO, 2018).

The importance of aquaculture is growing as a result of its capacity to sustainably supply the rising worldwide demand for fish. The world population has been steadily growing, increasing from 1 billion in 1800 to around 8 billion today (Roser *et al.,* 2013). By expanding from 5% in 1970 to 49% in 2020, aquaculture's contribution to world fish production has become increasingly significant in meeting this need (FAO, 2022). Per capita consumption of aquatic animal foods grew by about 1.4 percent per year, from 9.0 kg (live weight equivalent) in 1961 to 20.5 kg in 2019 (FAO, 2022).

According to the report by FAO (2022), fisheries and aquaculture sector will produce an additional 24 million tonnes from 2020, or 14% more, to reach 202 million tonnes by 2030 (Figure 1-1). However, compared to the prior decade (2010-2020), when it experienced a growth of 23% or 33 million tonnes, the growth rate and absolute level of increase are predicted to decline.

The aquaculture industry, which is anticipated to increase to 106 million tonnes in 2030, reflecting an overall gain of 22% or approximately 19 million tonnes from 2020, is the primary driver of the expansion in worldwide fisheries and aquaculture production. In 2027, it is expected to surpass 100 million tonnes for the first time. It is estimated that, in the overall worldwide production of fisheries and aquaculture for both food and non-food use, the proportion of farmed species will increase from 49% in 2020 to 53% in 2030. (Figure 1-1). (FAO, 2022). Thus, the expansion of aquaculture offers the best prospects for meeting global food demand and reducing poverty.

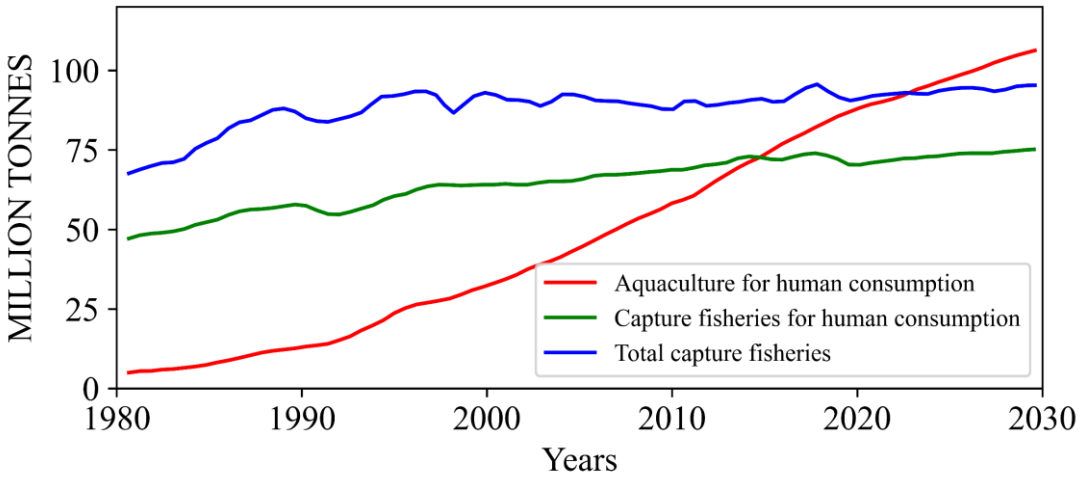

Figure 1- 1: World capture fisheries and aquaculture production, 1980-2030 (FAO, 2022).

The aquaculture sector in Norway is predominantly focused on finfish production, particularly Atlantic salmon (Salmo Salar). From the smolt stage until it reaches the ideal harvesting weight of 4-5 kilograms, this fish is usually farmed in sea-based fish cages. Atlantic salmon presently ranks first among cage-reared fish species, accounting for 51% of global cage aquaculture production. Norway alone accounts for more than half of global Atlantic salmon output (Tacon *et al.,* 2007). In 2018, global Atlantic salmon production was roughly 2.5 million tons, accounting for approximately 2.9% of total global aquaculture production. By 2022, it is expected to approach three million tons (Ernst & Young AS, 2019).

Norwegian Atlantic salmon farming is mostly based on sea cage farming, which involves raising fish in net pens or cages in open ocean habitats such as fjords or coastal locations. The Norwegian Ministry of Trade, Industry, and Fisheries established 13 Atlantic salmon aquaculture production zones in 2017 (Overton *et al.*, 2019). This allows for high-volume fish

production within constrained spatial limits, providing both efficiency and cost-effectiveness when compared to land-based systems.

The Norwegian aquaculture industry faces multiple challenges, including disease control, environmental effects, feed sustainability, climate change, and social and economic consequences (Bergheim, 2012). Disease outbreaks not only result in significant financial losses but also have a negative influence on fish welfare. However, the industry is actively taking measures to address these risks, such as implementing immunizations, enhancing biosecurity standards, and improving monitoring and surveillance methods (Bergheim, 2012).

The key challenges in the Norwegian salmon farming sector include limiting fish escape into the wild, controlling sea lice infestation, reducing water usage, and improving feed sustainability (Bergheim, 2012).

Aquaculture operations encounter the difficulty of potentially detrimental consequences on wild fish populations, sediment ecosystems, and water quality due to waste and chemical discharges (The Nature Conservancy, 2017; The Ocean Foundation, 2022). To mitigate these effects and align with sustainable practices, the industry is under pressure to adopt methods that promote environmental, economic, and social sustainability. These practices include exploring alternative feed sources and seeking more sustainable supplies of fishmeal and fish oil. Additionally, the industry can act as ecosystem observers and report on environmental changes (The Nature Conservancy, 2017; The Ocean Foundation, 2022).

Climate change also poses a major obstacle for the aquaculture sector. The environmental changes resulting from climate change have the potential to affect the sustainability of aquaculture operations and the health and well-being of fish. Furthermore, the livelihoods of those reliant on aquatic ecosystems for aquaculture activities will indirectly be impacted by climate-related events. To address this challenge, efforts are being made to develop more resilient fish breeds and employ cutting-edge technologies to mitigate the effects of climate change (Soto and Brugere, 2008).

The exploration of offshore or open ocean aquaculture operations is being considered as a potential response to the challenges faced by the Norwegian aquaculture industry. By relocating aquaculture activities in the open sea, fish welfare can be improved. In addition, the overall ecosystem can also be improved through better water exchange and the dispersal of waste across a larger area (Cardia and Lovatelli, 2015). However, this approach is not without difficulties, including exposure to harsh ocean conditions and logistical challenges associated with remote

locations. Therefore, it becomes crucial to accurately predict and account for the loads exerted on the structure during the design phase, considering both economic and safety considerations.

1.2 Overview of marine fish cage

A fish cage system can be classified by its hydrostatic positioning or structural systems.

In terms of hydrostatic positioning, there are three different variants: (a) floating cages, (b) semi-submerged cages, and (c) submersible cages are shown in Figure 1-2.

Floating cages are conventional that are installed on the water surface and have a constant water line. Semi-submersible cages are operated in a partially submerged state in order to reduce the wave load on the structure and be able to vary the waterline. Submerged cages are mainly operated underwater and could be raised to the surface for necessary maintenance and fish harvesting. The best feature of submerged cages is that they do not need to be as strong as the surface structure since they are submerged to avoid the effects of storms (Bugrov *et al*., 2006).

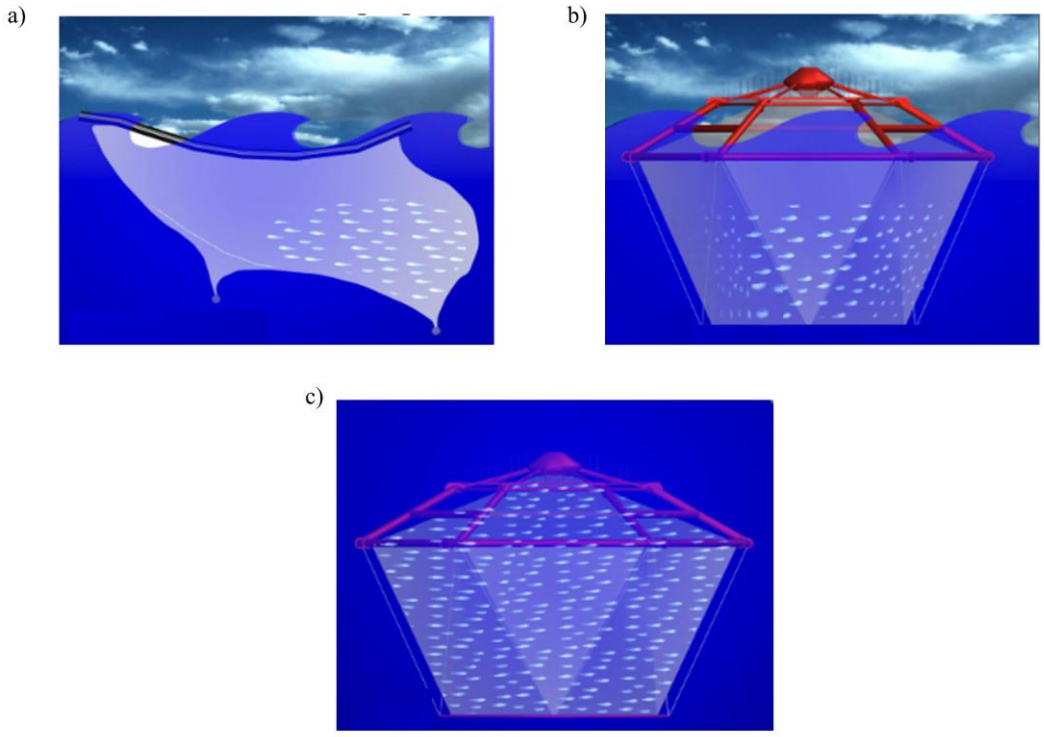

Figure 1- 2: (a) floating cages, (b) semi-submerged cages, and (c) submersible cages (Bugrov *et al*., 2006).

Another way to classify fish cages is with regard to the structural systems that maintain the cultivation volume proposed by (Loverich and Gace, 1998). There are four types of cages: (*i*) Gravity cages, (*ii*) anchor-tension cages, (*iii*) semi-rigid cages, and (*iv*) rigid cages are shown in Figure 1-3. (i) Gravity cages are the most commonly used in the fish farming industry. These

cages float with the help of a buoyancy element, which is a floating collar, and cultivation volume is provided by the underwater weighting system. (*ii*) Anchor – tension cages do not have a rigid frame and the cultivation volume is maintained by the tensioned mooring system. (*iii*) Semi-rigid or rigid steel parts of the cage relate to ropes to establish and sustain the cultivation volume. Finally, (*iv*) rigid cages use the rigid structural components to maintain the cultivation volume. (Ryan *et.al*., 2004).

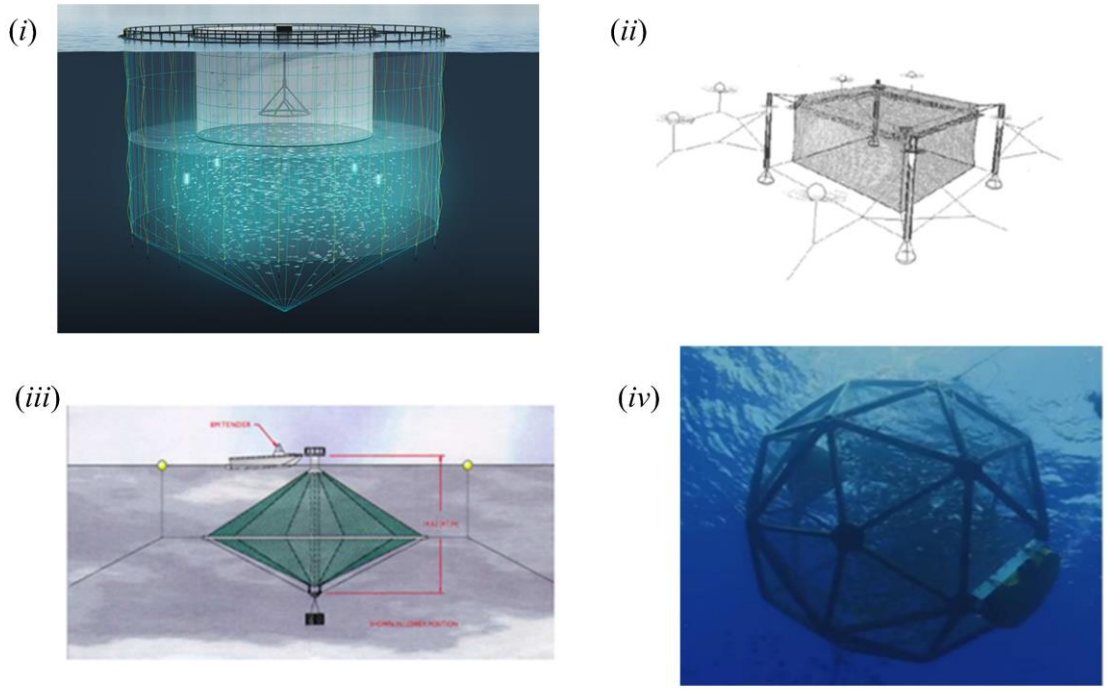

Figure 1- 3: (*i*) Gravity cages (AKVA Group, 2023), (*ii*) anchor-tension cages (Scott and Muir, 2000), (*iii*)semi-rigid cages (Scott and Muir, 2000), and (*iv*) rigid cages (Keith and James, 2023).

In addition to the general classification of the fish cages, there are several concepts proposed for offshore applications to adopt harsh environmental conditions. The vessel-shape fish farm with multiple cage system proposed by Nordlaks (2023) reduces the incoming wave load from the bow, and the application of the single-point mooring system allows rotation of the whole fish farm around the bow. Therefore, the infection risk of fishes can be reduced by spreading the feces from the fishes and the residue of the fees in a wider range of areas (Li *et. al*.,2018). RefaMed (2023) proposed a tension-leg cage (TLC) with a small floating collar and no mooring lines connected to it. With the help of its structural properties, during rough weather conditions, TLC submerged itself below the most violent sea surface layer. Thus, this

configuration of the cage can enable us to protect it from high environmental loads as shown in Figure 1-4.

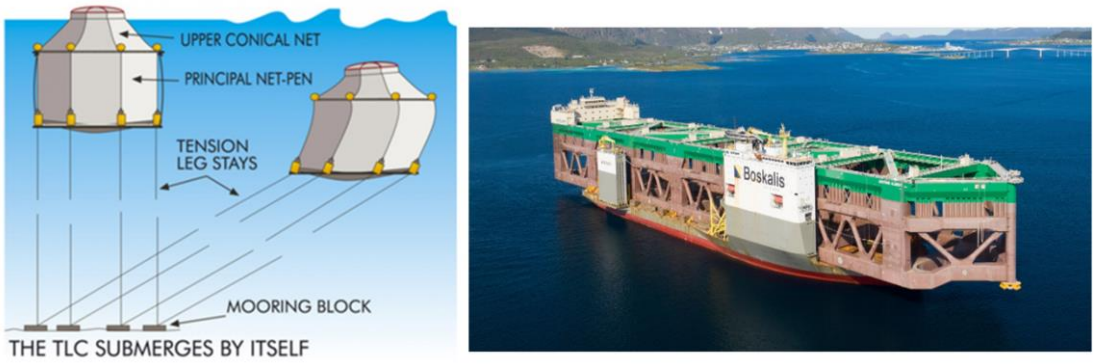

Figure 1- 4: Left tension-leg cage (RefaMed, 2023) right the vessel-shape fish farm (Nordlaks 2023).

1.3 Flexible gravity-based fish cage

Flexible gravity-based fish cage systems are popular in commercial fish farming because of its low cost, great output potential, and flexibility to various marine environments. A flexible gravity-based fish cage system can be divided into four main components: cage nets, buoyancy system, mooring system, and center point weights. Figure 1-5 illustrates a single fish cage.

Cage nets: The cage nets are made of high-density polyethylene (HDPE) material and feature a mesh pattern to allow water flow. They are attached to a frame for structure and rigidity and contain fish and other aquatic animals.

Buoyancy system: The buoyancy system consists of plastic or foam floats that are attached to the cage's top or sides to keep the cage afloat on the water's surface.

Mooring system: The mooring system uses ropes, chains, and cables to anchor the cage to the sea floor. It is designed to keep the cage in place in different water conditions.

Center point weights: The anchor weights are made of concrete or HDPE pipes and are attached to the bottom of the cage. They provide additional stability to the cage and prevent it from drifting.

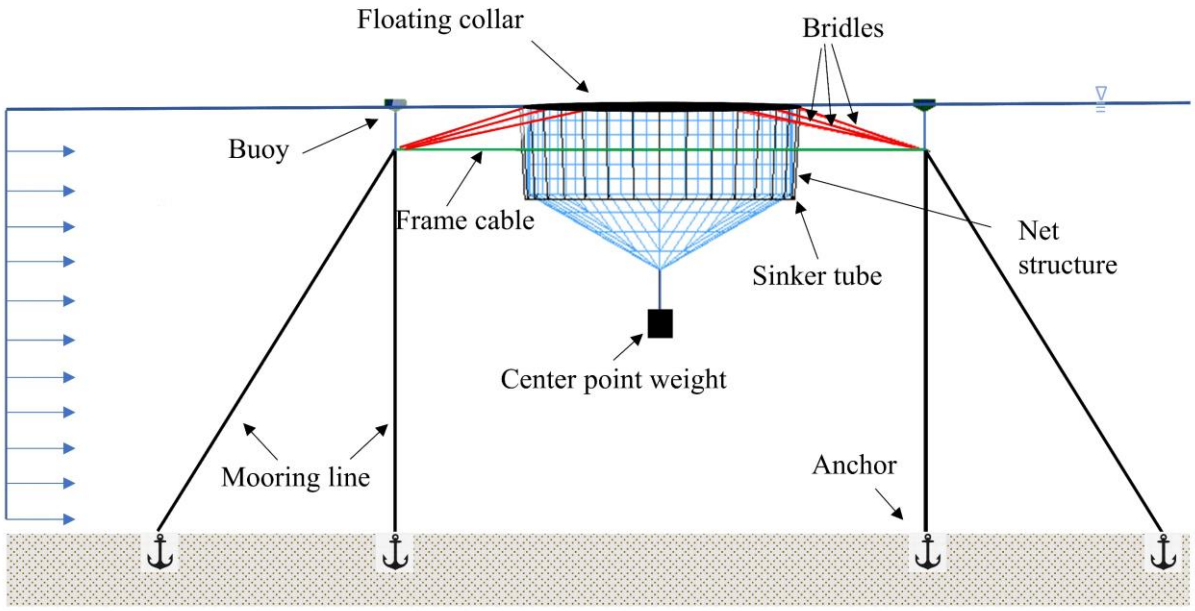

Figure 1- 5: Overview of a single gravity-based fish cage.

Flexible gravity-based fish cage systems have been shown to be an effective method for fish cultivation in a variety of maritime habitats (Cheng *et al.,* 2022). These systems are often made out of cage frames made of HDPE pipes and flexible mooring lines that allow them to tolerate water movements (*Cheng et al*., 2022). Furthermore, these systems can be configured to give an acceptable cultivation volume while also assuring the fish's well-being (Cheng *et al*., 2022). The present study focuses on this type of fish cages used in Norway.

1.4 Literature review

The complex and flexible design of fish farm structures, such as net structures, floaters, buoys, and cables, makes numerical modeling of their physical behavior difficult. However, scientists have made significant progress in precisely forecasting the behaviors of fish farm structures under currents and waves. Cheng (2017) emphasizes the importance of nets as an important component of aquaculture structures, accounting for more than 85% of total environmental loads on gravity-based fish cages. A precise estimate of net reactions under different current and wave conditions is necessary during the engineering design process of aquaculture structures, in order to ensure the proper construction of support structure and mooring system.

Løland (1991) proposed an empirical equation for the velocity reduction behind a net panel based on model testing and utilized this expression to approximate the wake effect after a fish cage. Bi and Xu (2018) numerically calculated the flow field around a 4x2 fish farm using the porous-media model. While their simulation provided useful data, the deformation of the fish cage was not included.

Experiments have also been conducted to investigate the wake effect in a variety of fish cages. Turner *et al*. (2016) assessed the drag forces of each square cage in a 2x3 array in a huge flume tank. Drag forces on the second and third cages were reduced by roughly 50% and 75%, compared to the first cage, when the cages were aligned with the flow direction. Similarly, Gansel *et al*. (2012) measured the wake characteristics behind a circular fish cage using particle image velocimetry. According to their findings, the flow velocity behind the fish cage was reduced by up to 40%.

Numerical modeling has proven to be an effective tool for investigating the behavior of aquaculture net cages and fish-farm systems under a variety of environmental circumstances. Endresen *et al*. (2013) discovered that the drag on net cages is strongly influenced by the wake created by fish-farm constructions. Kristiansen and Faltinsen (2012) created a numerical model that accurately predicted current loads on aquaculture net cages. Moe-Føre *et al*. (2015) examined various numerical modeling approaches for simulating net cage behavior and discovered that the finite element method was the most accurate and efficient. Zhao *et al*. (2013) discovered that the size and design of gravity cages, as well as flow velocity and water depth, influence water flow and oxygen distribution around the cages. Tsarau and Kristiansen (2019) investigated the effects of environmental loads on the behavior of an entire fish-farm system

and discovered that these loads have a significant impact on system behavior. Finally, Tang *et al.* (2019) investigated the impact of mooring line failure on the performance of a marine fish cage, discovering that it has a significant impact on cage performance under varied wave and current conditions. In a study conducted by Sim *et al*. (2021), the wake effect of a 4 × 2 cage array was investigated through numerical analysis. The findings revealed that the downstream cages experienced a more significant effect compared to the upstream cages. In another investigation, Cheng *et al*. (2023) used a computational model to assess the impact of wake effects on the drag force of downstream cages and discovered that the drag force on the cages varied greatly with the position of the downstream cage.

1.5 Scope and objective

The aquaculture industry faces a number of challenges, such as a lack of suitable sites, sea lice, environmental impact on the surrounding ecosystem. Those problems could be mitigated by improving the fish farm design or shifting the fish farm to a more exposed location. The above solutions require a well understanding of the wake effect inside fish farm and accurate predictions of structural responses. In this regard, the scope of this thesis is mainly focused on two subjects as follows.

(1) The effects of wake on the drag force of the downstream fish cage with respect to different solidities and cage positions are studied in detail using a computational fluid dynamic (CFD) method combined with a porous media model. This study also investigated the flow field through and around fish cages.

(2) A coupling algorithm between two open-source numerical toolboxes, OpenFOAM and Code_Aster, are developed for fluid-structure interaction analysis of 2 x 3 Array and a new design (Honeycomb) layout fish farm. The wake effects on the two layouts of fish farm, including flow field in and around fish farms, tensions in anchor lines, drag force, and cultivation volume, are investigated under different flow directions.

The structure of the thesis is given in Figure 1-6.

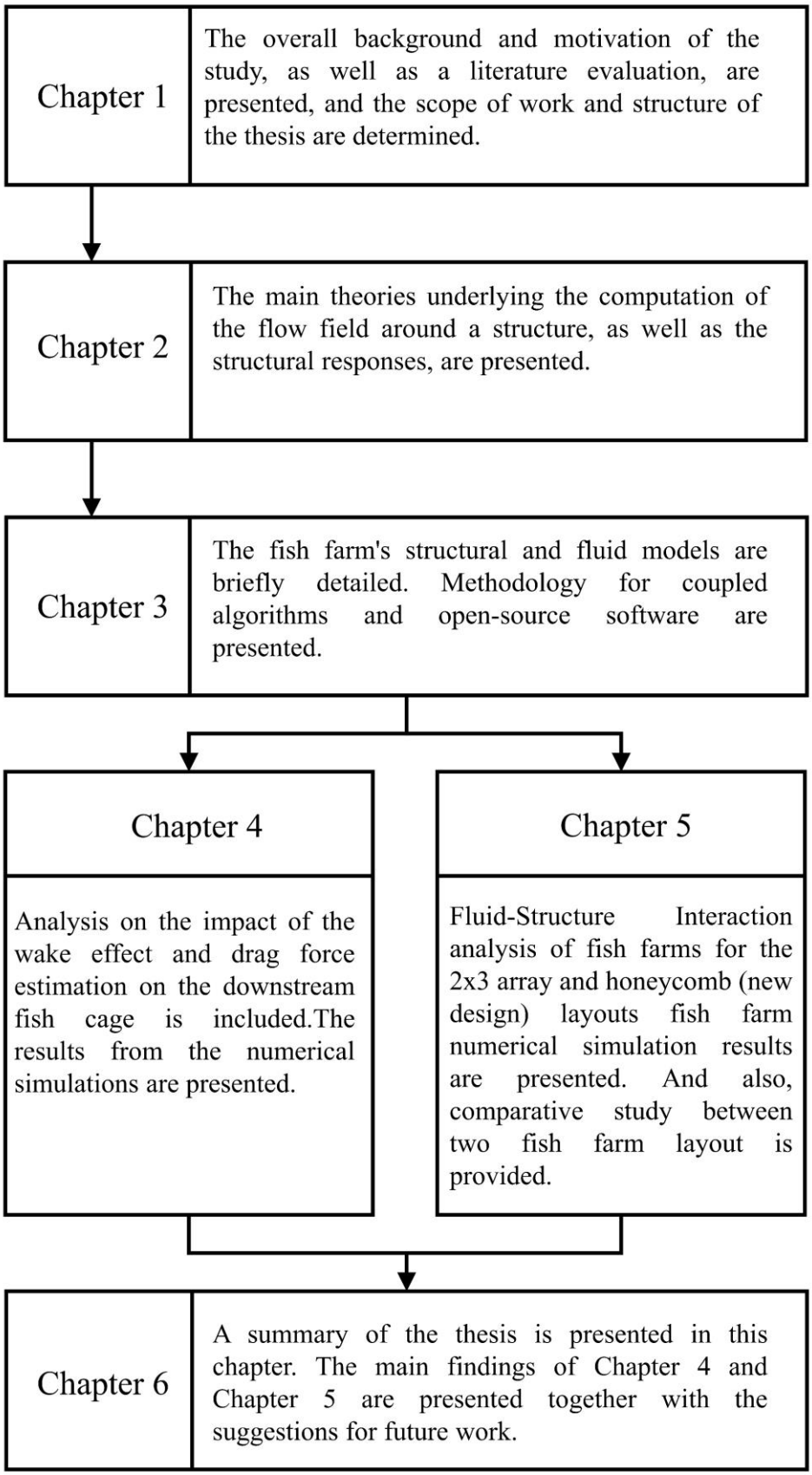

Figure 1- 6: The structure of the thesis.

Chapter 2

Theory

2.1 Wake flow

When a fluid flows around a circular cylinder, a laminar boundary layer forms around the cylinder and the flow is completely attached to the surface. Within the boundary layer, the pressure gradient, which is along the surface in the direction of the flow, depends on the velocity of the undisturbed external flow. In the case of a circular cylinder, according to conservation of mass, the same mass must stay the same and be moved around the cylinder. Therefore, velocity increases and reaches its maximum value at the thickest point of the boundary layer. However, kinetic energy change is directly related to static pressure change. Thus, static pressure decreases to a minimum, which means the pressure gradient in x- direction is negative at the thickest point of the boundary layer.

When the fluid finds more space to flow, the flow slows, and static pressure rises and reaches to the level of the atmosphere. This pressure gradient acts against the real direction. Mathematically, a positive pressure gradient is called an adverse pressure gradient. This results in a backflow area where boundary layer separation occurs. The separated flow falls downstream, and the resulting cylinder is known as a wake.

2.1.1 Flow around the cylinder

Due to the geometry of fish farm structures, cages can be positioned in tandem or staggered location relative to flow direction. The inbound flow velocity on downstream fish cages may be impacted by the disturbed flow caused by the presence of an upstream fish cage. As a result, the features of the flow before and after the circular cylinder are crucial in determining flow velocity.

A complex flow pattern is indicated by the flow over a circular cylinder. When the fluid approaches the cylinder, it is distributed and forms a boundary layer around it. The fluid hits the cylinder at the stagnation point, which completely stops the fluid. At that point, the fluid's pressure rises. While the flow velocity increases, the flow pressure decreases in the flow direction. The fluid hugs the cylinder on the frontal side at high Reynolds numbers, but it is difficult to stay attached to the surface. As a result, the boundary layer separates from the surface and begins to separate in the region behind the cylinder (Çengel, Y. A. and Cimbala, J. M., 2010). Zdravkovich (1997) proposed the distributed flow regions over the cylinder, as shown in Figure 2-1:

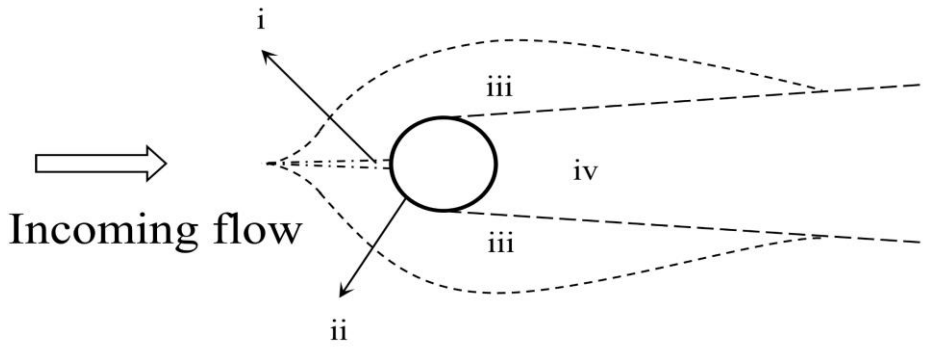

Figure 2-1: Regions of disturbed flow (Zdravkovich 1997).

(i) Narrow region of retarded flow.

(ii) Boundary layers attached to the surface of the cylinder.

(iii) Two sidewise regions of displaced and accelerated flow.

(iv) Wide downstream region of separated flow called the wake.

The main parameter to identify flow characteristics around a smooth circular cylinder is the Reynolds Number *Re*.

$$Re = \frac{DU}{v} \tag{2-1}$$

The change of the flow regime with regards to *Re* around a smooth circular cylinder is shown in Figure 2-2:

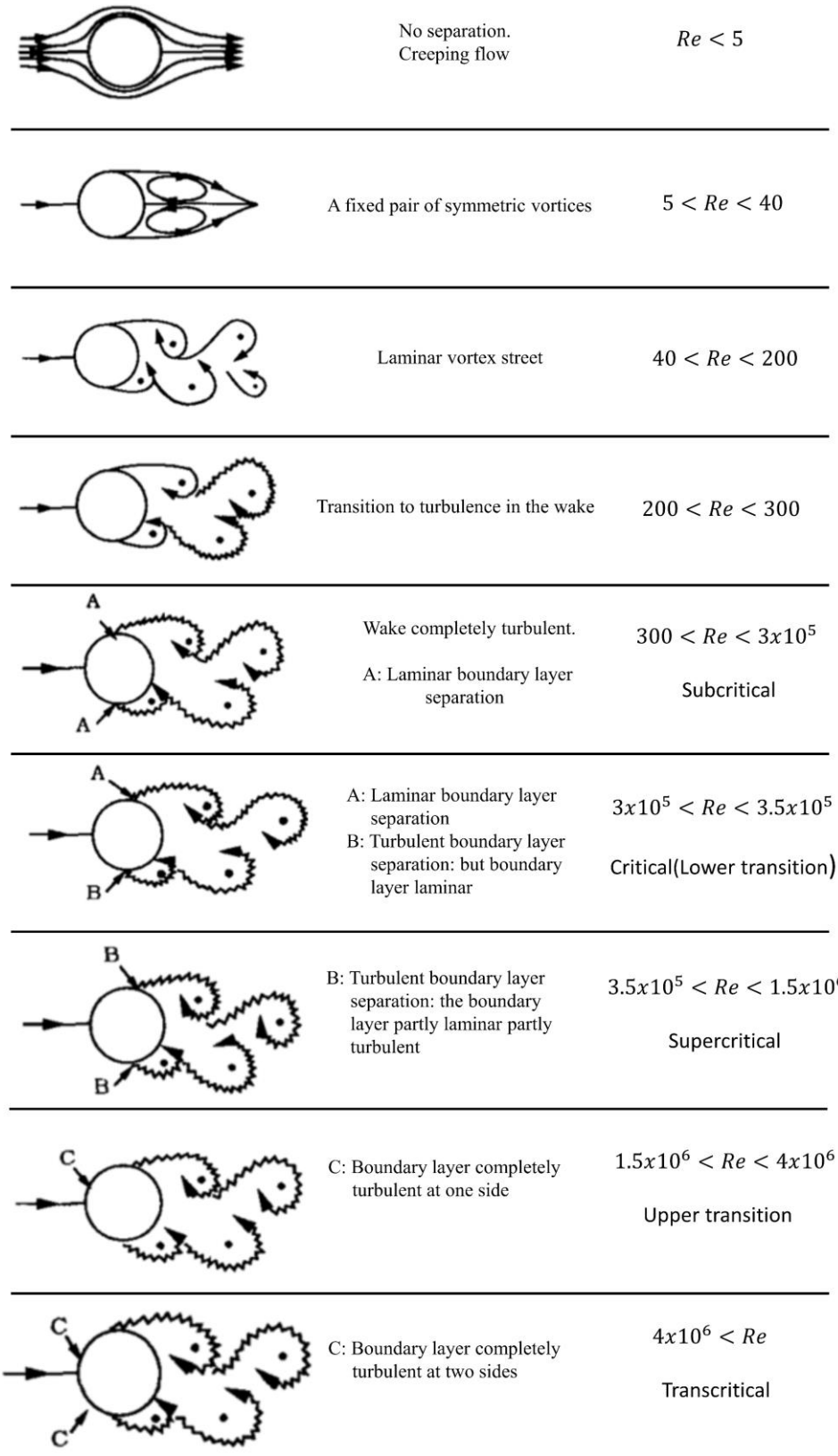

Figure 2- 2: Regime of flow around a smooth cylinder in steady current. (Sumer. and Fredsøe., 2006).

2.1.2 Vortex shedding

The boundary layer separates from the surface as a free shear layer and is highly unstable. The shear layer will eventually separate from the surface and form a distinct vortex. This is known as vortex shedding. The frequency of occurrence of this mechanism varies with the Reynolds number. The Strouhal number (St) represents the non-dimensional frequency of vortex shedding as shown in Eq (2-2).

$$St = \frac{f_{vs} D}{U} \tag{2-2}$$

where f_{vs} is the vortex shedding frequency, D is the cylinder diameter, U is the incoming velocity.

As shown in Figure 2-3, the relationship between *St* number and *Re* number is the primary indicator for defining flow regime and vortex characteristics.

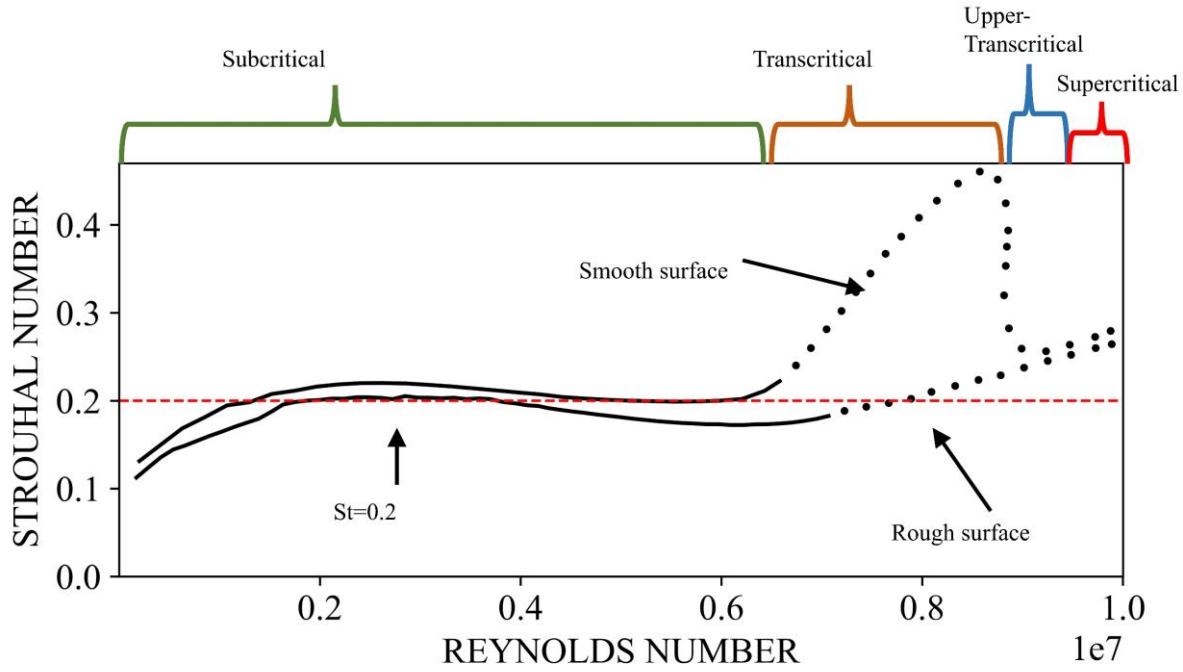

Figure 2- 3: Relationship between Re and St number for circular cylinder.

In the case of fish cages, the twines on the net panel can be regarded as a circular cylinder. Because of their small scale in comparison to a fish cage, they experience flow regimes in the supercritical regime, as illustrated in Figure 2-2. Although turbulent wake flow dissipates turbulent kinematic energy with 12D distance, as shown in Figure 2-4, this flow has no effect

on the main wake characteristic behind the fish cage due to the twine's very small diameter. As a result, instead of twines, turbulence was modelled in terms of a fish cage.

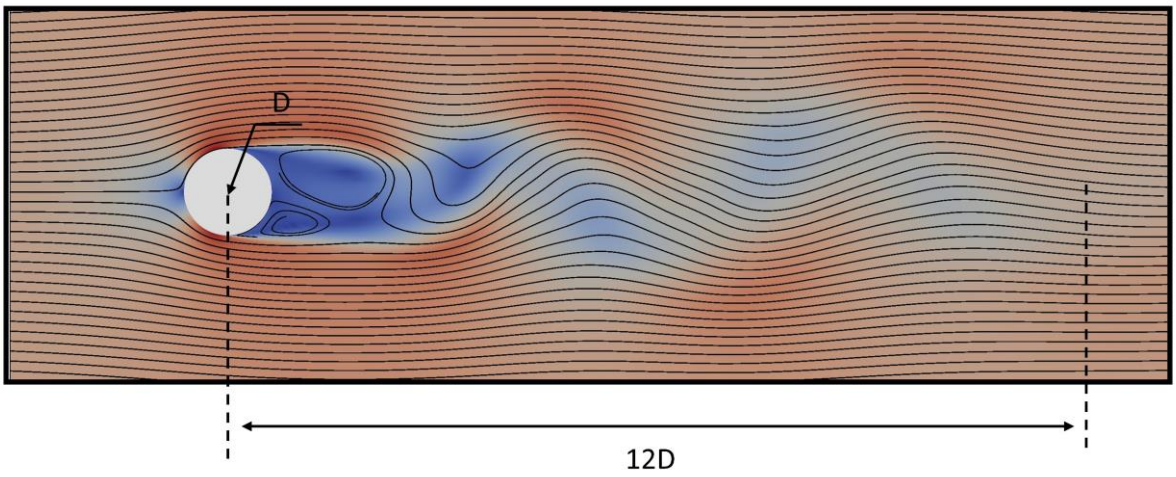

Figure 2- 4: Turbulent dissipation behind circular cylinder.

2.1.3 Wake model behind a circular cylinder

The purpose of the modelling wake is to find a relation between the velocity reduction through flow and the drag force on a net structure. The scientific norm of the wake model is to define a global wake with the distribution of wakes behind elements.

When a cylinder stays in a stream of fluid or moves in a fluid, a wake is formed behind the cylinder. Because of the velocity differences between the mainstream and wake region, the momentum of the fluid decreases, which is due to the drag force on the body.

Because free turbulent wake flow is similar to boundary layer flow, the flow behind a cylinder perpendicular to the main flow direction does not extend as far as the flow in the main flow direction. Therefore, the wake can be modelled with similar equations of the boundary layer flow are given as Eq. (2-3) for laminar flow, Eq. (2-4) for turbulent flow and continuity equation (2-5) (Schlichting, 1979).

$$\frac{\partial u}{\partial t} + u.\frac{\partial u}{\partial x} + v.\frac{\partial u}{\partial y} = \frac{-1}{\rho}\frac{\partial p}{\partial x} + v.\frac{\partial^2 u}{\partial y^2} \tag{2-3}$$

$$\frac{\partial u}{\partial t} + u.\frac{\partial u}{\partial x} + v.\frac{\partial u}{\partial y} = \frac{-1}{\rho}\frac{\partial p}{\partial x} + \frac{1}{\rho}\frac{\partial \tau}{\partial y} \tag{2-4}$$

$$\frac{\partial u}{\partial x} + \frac{\partial v}{\partial y} = 0 \tag{2-5}$$

where τ is the turbulent sheering stress, u and v are the real velocities for laminar flow and the mean velocities in an adequate time in turbulent flow case. Schlichting (1979) proposed Prandtl's mixing length theory to express the turbulent shearing stress for turbulent flow with Eqs. (2-6 and 2-7):

$$\tau = \rho l^2 \frac{|\partial u|}{|\partial y|} \frac{\partial u}{\partial y} \tag{2-6}$$

$$\tau = \rho \varepsilon_\tau \frac{\partial u}{\partial y} = \rho x_1 b (u_{max} - u_{min}) \frac{\partial u}{\partial y} \tag{2-7}$$

where b is the width of the mixing zone, l is the mixing length, x_1 is a constant, ε_τ is the virtual kinematic viscosity. The expression of the velocity deficit is given by Schlichting (1979) for turbulent flow and laminar flow which can be written by changing eddy viscosity to kinematic viscosity and the turbulent flow can be expressed with Eq. (2-8).

$$u_1(x, y) = \frac{1}{4\pi} C_D D U_\infty \sqrt{\frac{\pi U_\infty}{\varepsilon_\tau x}} exp\left(\frac{-y^2 U_\infty}{4\varepsilon_\tau x}\right) \tag{2-8}$$

where u_1 is the velocity difference between the ambient flow velocity (U_∞) and the measured velocity at a point. The x-axis is in the direction of flow, d is the diameter of the cylinder, and C_D is the Reynolds number dependent drag coefficient for a or circular cylinder (Løland 1991).

The eddy viscosity is still unknown, but from measurements by Schlichting (1979) we have that:

$$\varepsilon_\tau = 0.0222\, U_\infty\, C_D\, D \tag{2-9}$$

The final solution for the velocity profile in a turbulent wake behind a single cylinder in steady flow is given as:

$$u_1(x, y) = 0.95 U_\infty \left(\frac{C_D D}{x}\right)^{1/2} exp\left(-\frac{y^2}{0.0888 C_D D x}\right) \tag{2-10}$$

This equation can also be used in a similar manner to calculate the two-dimensional wake behind a two-dimensional net if we approximate the net by a row of cylinders.

$$\frac{u(x,y)}{U_\infty} = 1.0 - 0.95\sum_{i=1}^{N_i}\sqrt{\frac{C_{D_i}D_i}{x-x_i}}exp\left(-\frac{(y-y_i)^2}{0.0888C_{D_i}D_i(x-x_i)}\right) \quad (2\text{-}11)$$

2.1.3.1 The turbulent Wake far down stream

The form of a turbulent wake far downstream is independent of the local effects at the generation point, according to general wake theory. It is only affected by the body's drag force and eddy viscosity.

Therefore, the two-dimensional wake behind a screen far down stream is also given as:

$$u_1(x,y) = 0.95U_\infty(\frac{C_D D}{x})^{1/2}exp\left(-\frac{y^2}{0.0888C_D Dx}\right) \quad (2\text{-}12)$$

Near the screen, the single-body model, which is assumed to be asymptotically correct far downstream, produces completely incorrect velocity values. This is also to be expected given that the boundary layer equations that lead to the expression are only valid further downstream than 50-100 times $C_D\,L$ (F.M.White 1974).

The sum of the cylinders model produces incorrect values far downstream due to the use of eddy viscosity. The eddy viscosity is proportional to the wake width.

In the above calculation we used empirical value for eddy viscosity proposed by Schlichting (1979).

$$\varepsilon_\tau = 0.0222\,U_\infty\,C_D\,D \quad (2\text{-}13)$$

Which in the sum of the cylinders model becomes.

$$\varepsilon_{\tau_i} = 0.0222\,U_\infty\,C_{D_i}\,D_i \quad (2\text{-}14)$$

We need to adjust the eddy viscosity expression to take into account the merging of wakes from various bodies in order to get a better answer further downstream. Therefore, the governing equation of the far wake is given as:

$$u_1(x,y) = \frac{1}{4\pi} C_D D U_\infty \sqrt{\frac{\pi U_\infty}{\nu_0 x(1+(N-1)\tanh(x/C_D d)}} exp\left(-\frac{y^2 U_\infty}{4\nu_0 x(1+(N-1)\tanh(x/C_D d)}\right) \quad (2\text{-}15)$$

Løland (1991) concluded that if the eddy viscosity is related to the individual thread without taking into account the merging of the wakes in the eddy viscosity, the sum of cylinder models overestimates the velocity defect far downstream.

2.1.3.2 Near-field modification of the velocity deficit in the wake region

Schlichting's formula accurately predicts the velocity deficit in the far-field wake (typically a distance of 80 – 100 diameters downstream) according to experimental results. However, at smaller *x/d* ratios, this formula tends to overestimate the velocity deficits and produces a narrower wake region. As a result, researchers have modified the original formulation to achieve better results in the near-field wake (Frandheim 2005).

In order to improve Schlichting's formula, Blevins (2001) incorporated the concept of a virtual origin of the wake, which involves introducing a virtual distance. Furthermore, the constants in the original formula were adjusted. As a result of these modifications, the velocity deficit in the turbulent wake behind a circular cylinder positioned at the origin x=0, y=0 can be accurately predicted.

$$\frac{u_1}{U_\infty} = 1.02\sqrt{\frac{C_D}{6+(\frac{x}{D})}} exp\left(-\frac{(\frac{y}{D})^2}{0.0767 C_D(6+(\frac{x}{D}))}\right) \quad (2\text{-}16)$$

The velocity reduction at a given coordinate x and y is represented by u_1, while U_∞ denotes the undisturbed flow velocity, and C_D refers to the Reynolds number dependent drag coefficient for a circular cylinder. Through experiments, Fredheim (2005) confirmed the accuracy of the Virtual Origin Wake model and demonstrated its applicability in calculating the drag force on a downstream cylinder located 3.8 D behind an upstream cylinder at Reynolds numbers ranging from 2.0×10^4 to 6.0×10^4.

2.1.4 Wake behind a screen

Løland (1991) proposed a net panel wake model for a single cylinder in steady flow based on Schlichting's velocity profile formula. (Eq. 2-10). The contributions from individual cylinders inside the screen were combined to determine the net panel's wake, although hydrodynamic interaction between them was ignored. Assuming the screen is rigid, this assumption holds true when the mesh size (L) to cylinder diameter (d_w) ratio is greater than 5-6 (Figure 2-5). The drag coefficient of the screen was discovered to have a consistent solution for the current force as follows:

$$F_D = \sum_{i=0}^{N} F_{d,i}$$

$$\frac{1}{2}\rho\, C_D U_\infty^2 A = \sum_{i=0}^{N} \frac{1}{2}\rho\, C_d U_\infty^2\, d_i l_i \qquad (2\text{-}17)$$

$$C_d = \frac{C_D A}{\sum_{i=0}^{N} d_i l_i}$$

where F_D is the drag force for a screen, F_d is the drag force for a twine, C_D is the drag coefficient for a screen, C_d is the drag coefficient for a twine, A is the area for a net panel, d_i is the diameter of the ith twine, l_i is the mesh size of ith twine, U_∞ is the flow velocity, ρ is the density of the fluid, and N is the total number of twines.

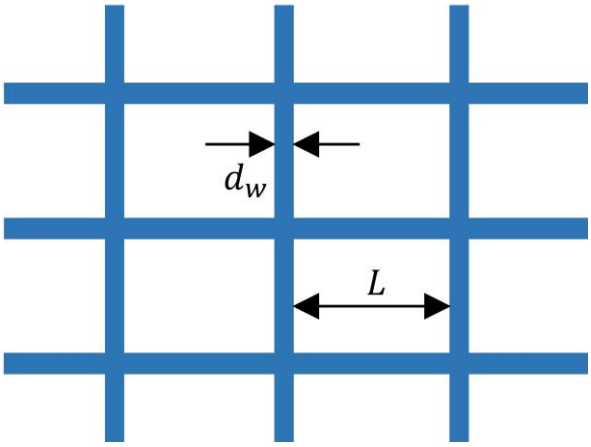

Figure 2- 5: Illustration of the net panel.

The velocity profile of the wake behind a screen is derived based on equations Eq. 2-10 and Eq. 2-17 as follows:

$$\frac{u(x,y,z)}{U_\infty} = 1.0 - 0.95\sum_{i=1}^{N_i}\sqrt{\frac{C_{d_i}d_i}{x-x_i}}\exp\left(-\frac{(y-y_i)^2}{0.0888C_{d_i}d_i(x-x_i)}\right) - 0.95\sum_{j=1}^{N_j}\sqrt{\frac{C_{d_j}d_j}{x-x_j}}\exp\left(-\frac{(z-z_j)^2}{0.0888C_{d_j}d_j(x-x_j)}\right) \quad (2\text{-}18)$$

where N_i is the number of twines in y-direction, N_j is the number of twines in the z-direction, C_{di} is the drag coefficient for an ith twine, C_{dj} is the drag coefficient for a jth twine, coordinates x, y, z are the field point for calculation of velocity, and x_i, y_i, zi are the source point of the screen element. The comparison between the model test and the computed value from the Eq. 2-18 showed a good agreement (Løland 1991).

The velocity in the near wake field (1~2 times the dimension of the net) showed that the velocity in the wake was constant except the flanks of the wake region.

2.2 Hydrodynamic forces

The fundamental theories underlying two hydrodynamic force models for the aquaculture structure are covered in this part. Two different force model types are primarily used to calculate the pressures acting on the aquaculture structure: the Morison type force model and the screen type force model.

2.2.1 Hydrodynamic force on the mooring system

The mooring system's lines-like structure, such as rope or wire, is subject to hydrodynamic forces. Using Morison's equation, the hydrodynamic forces on each line-like structure are calculated and added to determine the overall drag force of the mooring system.

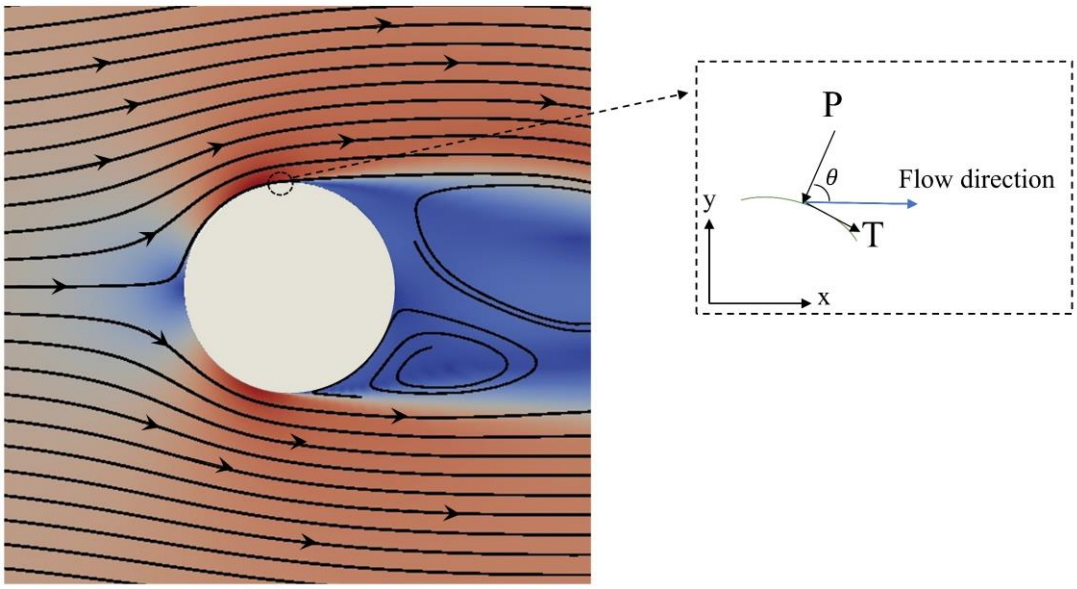

Figure 2- 6: The pressure and viscous forces acting on a circular cylinder.

2.2.1.1 Morison type force model

The forces acting on a submerged circular cylinder in a flowing fluid must be understood in order to apply the Morison force model method to mooring system substructures. A fluid in motion also places tangential shear forces on the cylinder's surface due to the no-slip condition, in contrast to a fluid at rest that only applies normal pressure forces to the surface. As a consequence, it is possible to calculate the drag force, which is the sum of the pressure and friction forces acting in the direction of the flow. The term "lift forces" also refers to the parts of pressure and friction forces acting perpendicular to the flow. However, the drag force is the only time-averaged force acting on an axisymmetric body, such as a circular cylinder (Çengel, Y. A. and Cimbala, J. M., 2010). Eq (2-19) shows the expression for the differential drag force:

$$dF_D = -PdA\cos\theta + TdA\sin\theta \qquad (2\text{-}19)$$

where P is the pressure around the cylinder, dA is the differential area of the cylinder, T is the shear stress operating on the cylinder, and θ is the angle between the flow direction and the pressure vector which is inward normal to the surface of the cylinder (see Figure 2-6) The expression for the total drag force acting on the cylinder is obtained by integrating Eq.(2-19) over the full surface of the cylinder.

$$F_D = \int_A (-P\cos\theta + T\sin\theta)dA \tag{2-20}$$

The total drag force on a cylinder is determined by the fluid's density, flow rate, or *U*, and the cylinder's diameter, or *d*. As a result, it is practical to divide the equation (Eq.2-20) by the stagnation pressure (kinetic energy of the flow), which is equal to $0.5\rho dU^2$, to describe the drag force with a dimensionless drag coefficient. The following is the circular cylinder's drag coefficient:

$$C_D = \frac{F_D}{0.5\rho dU^2} \tag{2-21}$$

The stagnation pressure and drag coefficient can be used to organize the drag force on a unit length of the cylinder. Since both the friction force and the pressure rely on the Reynolds number, the drag coefficient also depends on the Reynolds number. The following Eq. (2-22) is the drag force on a cylindrical cylinder with unit length.

$$F_D = 0.5\rho dU^2 C_D(Re) \tag{2-22}$$

where Re is the function of the drag coefficient C_D.

The hydrodynamic forces on a slender cylindrical body are calculated using Morison's equation (mooring system substructures). The crossflow principle, which states that the force relies only on the velocity component normal to the cylinder axis, forms the basis of the equation. In order to calculate the crossflow force, Morison *et al*. (1950) superimposed the inertia force and the drag force. This force is exerted on a unit length of the submerged, slender cylindrical body (Eq. 2-23)

$$F(t) = \frac{\pi}{4}\rho C_M d^2 \,.\dot{u}(t) + \frac{1}{2}\rho C_D d \,.u(t)|\,u(t)| \tag{2-23}$$

where C_M is the mass coefficient, C_D is the drag coefficient, ρ is the fluid density around the cylinder, d is the cylinder's diameter, u is the flow's velocity, and $\dot{u}$ is the flow's acceleration. The inertial force is the first term on the right side of Eq. (2-23), and the drag force, which stands in for the viscous forces, is the second term. The Froude-Krylov force, which is the force a submerged body experiences from the oscillatory flow's unstable pressure field, and the

diffraction force, which is the force caused by the body's existence, are both represented by the inertial term. When the flow is constant, the inertial term disappears, leaving only the drag term.

In the case of inclined structures due to fish farm geometry or mooring system deformation, the velocity components normal and tangential to the structure should be considered to calculate the drag associated with the crossflow principle as shown in Figure 2-7.

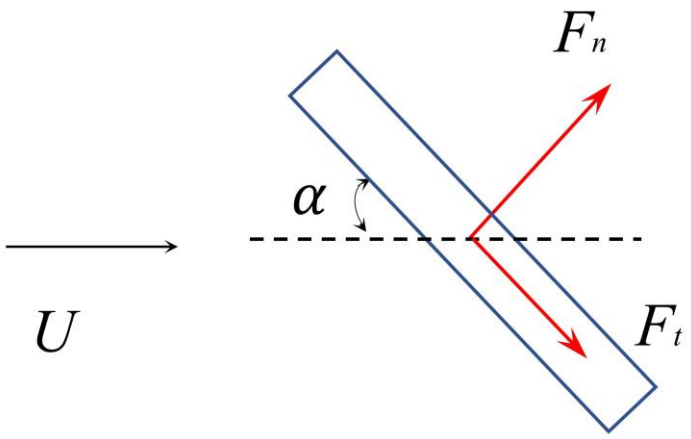

Figure 2- 7: The illustration of the environmental loads on a line-like structure. $\boldsymbol{Fn}$ and $\boldsymbol{Ft}$ are the normal and tangential drag, respectively. The angle of attack α is the angle between the current direction and the axis of a line-like structure.

$$\boldsymbol{F_n} = \frac{1}{2} C_n \rho L \, d |\boldsymbol{u^r}_{\boldsymbol{n}}| \boldsymbol{u^r}_{\boldsymbol{n}} \tag{2-24}$$

$$\boldsymbol{F_t} = \frac{1}{2} C_t \rho \, L \, d |\boldsymbol{u^r}_{\boldsymbol{t}}| \boldsymbol{u^r}_{\boldsymbol{t}} \tag{2-25}$$

where L is the length of the line-like structure, d is the diameter of the line-like structure, ρ is the fluid density. $\boldsymbol{u^r}_{\boldsymbol{n}}$ and $\boldsymbol{u^r}_{\boldsymbol{t}}$ are the normal and tangential velocity of fluid relative to the line-like structure($\boldsymbol{u^r} = \boldsymbol{U}_{-\infty} - \dot{\boldsymbol{q}}$). C_n and C_t are the drag coefficients in normal and tangential directions, respectively.

2.2.2 Hydrodynamic force on net structure

The netting is regarded to be a vital component of maritime aquaculture structures. The hydrodynamic loads on the net are affected by the inbound flow rate and the hydrodynamic characteristics of the net, which are decided by variables such as the materials used, mesh and twine forms, and net weaving techniques. According to study done by Løland (1991), the hydrodynamic properties of the net also rely on the Reynolds number and solidity ratio of the net construction. These factors will be explored further in the following parts.

2.2.2.1 Screen type force model

According to the screen model, hydrodynamic forces are computed using a planar net panel, with the twines being regarded as an essential component of the net panel. Technically, there are two discrete components to the hydraulic loads on the net screen. These components can be broken down in relation to the panel or the flow. In general, the hydrodynamic loads are divided into drag and lift forces in relation to the direction of the fluid velocity ($\boldsymbol{F_D}$ and $\boldsymbol{F_L}$ in the equation 2-26 – 2-29).

$$\boldsymbol{F_D} = \frac{1}{2} C_D \rho_w A_t |\boldsymbol{U}_{-\infty} - \dot{\boldsymbol{q}}|^2 \boldsymbol{i_D} \tag{2-26}$$

$$\boldsymbol{F_L} = \frac{1}{2} C_L \rho_w A_t |\boldsymbol{U}_{-\infty} - \dot{\boldsymbol{q}}|^2 \boldsymbol{i_L} \tag{2-27}$$

$$\boldsymbol{i_D} = \frac{\boldsymbol{U}_{-\infty} - \dot{\boldsymbol{q}}}{|\boldsymbol{U}_{-\infty} - \dot{\boldsymbol{q}}|} \tag{2-28}$$

$$\boldsymbol{i_L} = \frac{(\boldsymbol{U}_{-\infty} - \dot{\boldsymbol{q}}) \times e_n \times (\boldsymbol{U}_{-\infty} - \dot{\boldsymbol{q}})}{|(\boldsymbol{U}_{-\infty} - \dot{\boldsymbol{q}}) \times e_n \times (\boldsymbol{U}_{-\infty} - \dot{\boldsymbol{q}})|} \tag{2-29}$$

A_t is the area of a virtual net panel, $\boldsymbol{U}_{-\infty}$ is the unaltered inbound flow velocity, $\dot{\boldsymbol{q}}$ is the structure's velocity, ρ_w is the fluid's density, $\boldsymbol{i_D}$ and $\boldsymbol{i_L}$ are unit vectors that denote the forces' directions, C_D is the drag coefficient, and C_L is the lift coefficient. Eqs. (2-30) and (2-31) provide the formulas for the drag and lift coefficients. For a constrained range of solidity ratios (0.13-0.317), the force coefficients can be determined empirically or by applying Løland (1991) (functional)'s relationships with *Re, Sn*, and intake angle θ . The concept of the θ and the hydrodynamic forces acting on a net screen are shown in Figure 2-8.

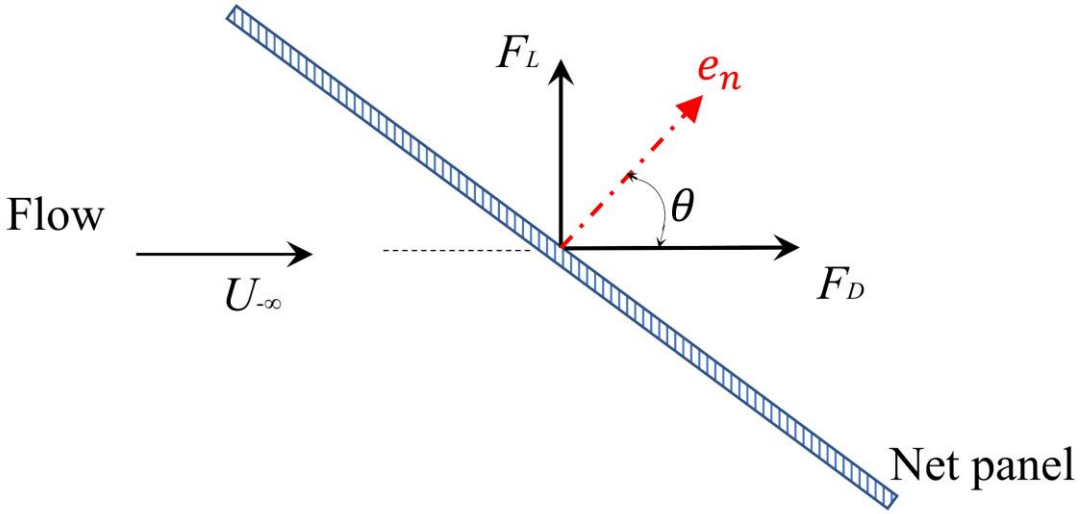

Figure 2- 8: Illustration of the hydrodynamic forces on a net panel and the defination of θ.

$$C_D = 0.04 + (-0.04 + 0.33Sn + 6.54Sn^2 - 4.88Sn^3)cos\,(\theta) \quad (2\text{-}30)$$

$$C_L = (-0.05Sn + 2.3Sn^2 - 1.76Sn^3)sin(2\theta) \quad (2\text{-}31)$$

The Sn is defined as the ratio between area covered by the threads in the net and the outline area of the net. The value of *Sn* is calculated using Eq. (2-32), where d_w is the twine diameter and L is the mesh size of a net panel as shown in Figure 2-5.

$$Sn = \frac{2d_w}{L} + \frac{1}{2}(\frac{d_w}{L})^2 \quad (2\text{-}32)$$

The hydrodynamic loads on a net panel, according to Fridman (1973), can also be divided into normal drag ($\boldsymbol{F_N}$) and tangential drag ($\boldsymbol{F_T}$), which are correlated with the direction of the net panel. These two components' formulas are Eqs. (2-33) and (2-34) where $\boldsymbol{u^r}_{\boldsymbol{n}}$and $\boldsymbol{u^r}_{\boldsymbol{t}}$ are the normal and tangential components of the fluid velocity relative to the net panel. C_N and C_T are the normal and tangential drag coefficients of the net panel.

$$\boldsymbol{F_N} = \frac{1}{2}C_N\rho A_t|\boldsymbol{u^r}_{\boldsymbol{n}}|\boldsymbol{u^r}_{\boldsymbol{n}} \quad (2\text{-}33)$$

$$\boldsymbol{F_T} = \frac{1}{2}C_T\rho A_t|\boldsymbol{u^r}_{\boldsymbol{t}}|\boldsymbol{u^r}_{\boldsymbol{t}} \quad (2\text{-}34)$$

The Morison model is formulated similarly in equations (2-24) and (2-25), with the exception that the reference area A_t is now the net panel rather than the twine's projected area $d_w L$.

The relationships of $\boldsymbol{F_N}$, $\boldsymbol{F_T}$, $\boldsymbol{F_D}$, $\boldsymbol{F_L}$ and θ are shown in Figure 2-9. The relationships of C_D, C_L, C_N, C_T are given in Eqs. (2-35) and (2-36).

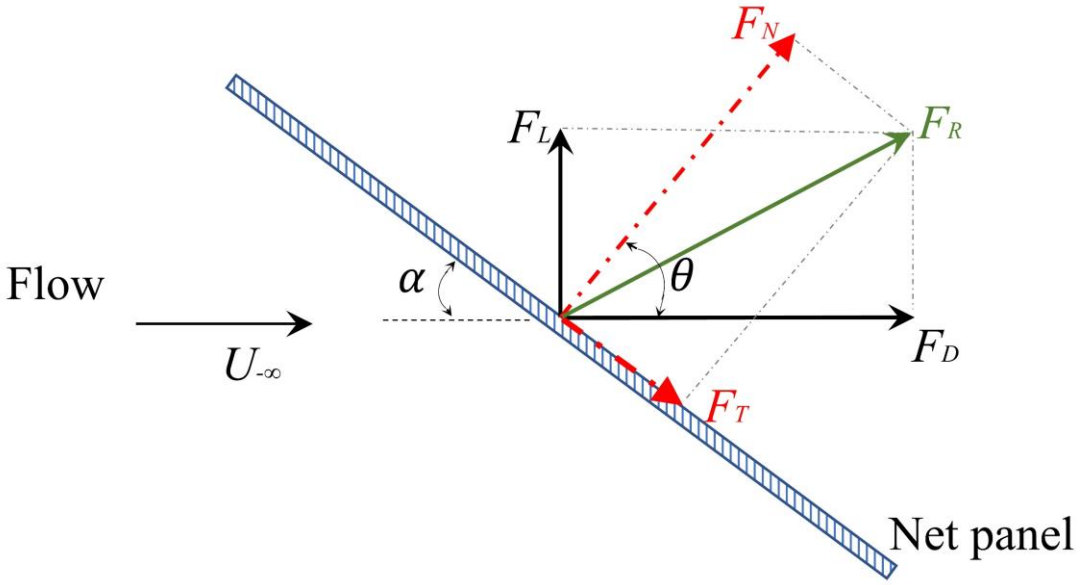

Figure 2- 9: Two dimensional visualazation of hydrodyanmc forces on the net panel. $\boldsymbol{F_R}$ resultant force can be divided as normal drag $\boldsymbol{F_N}$ and tangential drag $\boldsymbol{F_T}$ or drag $\boldsymbol{F_D}$ and lift force $\boldsymbol{F_L}$.

$$C_D = C_N \cos\theta \cos^2\theta + C_T \sin\theta \sin^2\theta \tag{2-35}$$

$$C_L = C_N \sin\theta \cos^2\theta - C_T \cos\theta \sin^2\theta \tag{2-36}$$

Chapter 3 will provide an explanation of how force models are applied in numerical studies.

Chapter 3

Numerical method

3.1 Structural model

In order to investigate the dynamic response of the marine aquaculture structure which consists of net structure, floating collar, sinker tube, buoy, and cables, FEM is used. Based on the shape and dimension of the element, the structural elements can be categorized into zero-dimensional (0D) element, one dimensional (1D) element, two-dimensional (2D) element and three-dimensional (3D) element, according to Okereke and Keates (2018). For modelling the global response of marine aquaculture structures, three models, i.e., mass -spring model, truss finite element model and triangular finite element model, are commonly used. In the present study 1D truss finite element model used for net structure and mooring system.

3.1.1 Truss finite element model

The truss finite element model is commonly used for the dynamic analysis of marine aquaculture structures, and it has been applied to many other industrial applications. This element type was originally developed for structural analyses of small-displacement structures. With further development, this element can be used for dynamic analyses of structures with large displacement and rotation in marine environments. The element name may be changed depending on the numerical solver. The element name is "CABLE" in Code_Aster as shown in Figure 3-1. The equations governing the global motion of the structure can be writing as:

$$[M + M_a]\ddot{\boldsymbol{q}} + [C]\dot{\boldsymbol{q}} + [K]\boldsymbol{q} = \boldsymbol{F_{D(\dot{q})}} + \boldsymbol{B_{(q)}} + \boldsymbol{W_{(q)}} \qquad (3\text{-}1)$$

where the [M+Ma] is the mass matrix, [K] is the global stiffness matrix, [C] is the damping matrix, $\boldsymbol{F_D}$ is the hydrodynamic loads, $\boldsymbol{B}$ is the buoyancy and $\boldsymbol{W}$ is the weight.

Tsukrov et al. (2003) proposed a consistent finite element (a linelike element) to analyze the structural responses of offshore aquaculture fish cages under the action of currents and waves, and it is successfully applied to the dynamic analyses of fish cages and mussel longlines (Shainee et al., 2013; DeCew et al., 2010; Knysh et al., 2021).

For modelling netting, the nodes are usually located at the intersection of twines (or the knots), and the elements are usually aligned with the twine. For modelling a rope, the elements are usually linked with nodes and are aligned with the rope. The solution techniques of Eq. (3-1) are usually based on the Newmark-β method for the time integration and the Newton-Raphson iteration scheme to find nodal displacement at every time step.

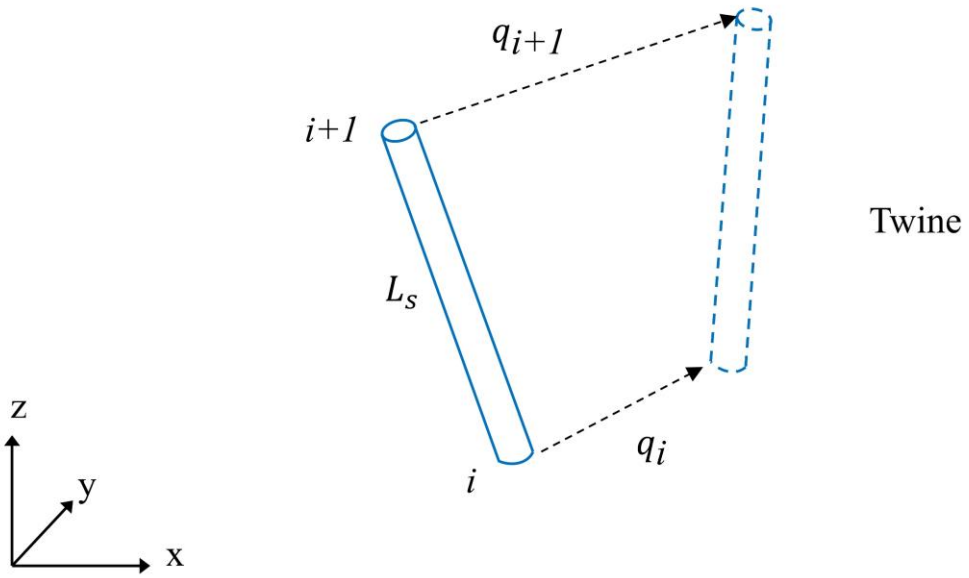

Figure 3- 1: illustration of the "CABLE" element.

3.1.2 Governing equations

The Finite Element Method (FEM) is used to calculate the structural responses by dividing the net and mooring system into a series of one-dimensional elements. The equation that governs the motion of Lagrangian nodes in the Cartesian coordinate system is as follows:

$$[\boldsymbol{M}]\ddot{\boldsymbol{q}} + [\boldsymbol{K}]\boldsymbol{q} = \boldsymbol{F_g} + \boldsymbol{F_b} + \boldsymbol{F_h} \tag{3-2}$$

The mass matrix, $\boldsymbol{M}$, stiffness matrix, $\boldsymbol{K}$, the time-dependent vector of nodal displacement, $\boldsymbol{q}$, and nodal force vectors, $\boldsymbol{F_g}$ (due to gravity), $\boldsymbol{F_b}$ (for buoyancy forces), and $\boldsymbol{F_h}$ (for hydrodynamic forces) all contribute to the dynamic behavior of the system in a numerical simulation of nodal displacements. It should be noted, however, that $\boldsymbol{F_g}$ and $\boldsymbol{F_b}$ are constants computed just once during the initialization stage and stay constant throughout the simulation.

The system's high nonlinearity can be attributed to $\boldsymbol{F_h}$'s dependency on time, the square of nodal velocities, and structural deformations. According to Antonutti *et al.* (2018), such nonlinearity can cause high-frequency oscillations and make it difficult for simulations to approach convergence. To overcome this problem, the current structural solver solves Eq. (3-2) using the unconditionally stable Hilber-Hughes-Taylor-α (HHT-α) approach. To ensure

accurate temporal integration of the equation, this method introduces low numerical damping in the low-frequency band and high damping in the high-frequency band. The temporal integration of Eq. (3-2) is:

$$\begin{aligned} \boldsymbol{M}\ddot{q}_{i+1} + (1-\alpha)\boldsymbol{K}\boldsymbol{q}_{i+1} + \alpha\boldsymbol{K}\boldsymbol{q}_i \\ = (1-\alpha)(\boldsymbol{F_s} + \boldsymbol{F_h})_{i+1} + \alpha(\boldsymbol{F_s} + \boldsymbol{F_h})_i \end{aligned} \tag{3-3}$$

$$\boldsymbol{q}_{i+1} = q_i + \Delta t\dot{\boldsymbol{q}}_i + \Delta t^2[(0.5-\beta)\ddot{\boldsymbol{q}}_{\boldsymbol{i}} + \beta\ddot{\boldsymbol{q}}_{\boldsymbol{i+1}}] \tag{3-4}$$

$$\dot{\boldsymbol{q}}_{i+1} = \dot{\boldsymbol{q}}_i + \Delta t[(1-\gamma)\ddot{\boldsymbol{q}}_{\boldsymbol{i}} + \gamma\ddot{\boldsymbol{q}}_{\boldsymbol{i+1}}] \tag{3-5}$$

where Δt is the time increment. The parameters α, β and γ are satisfied:

$$0 \le \alpha \le \frac{1}{3}, \qquad \beta = \frac{(1+\alpha)^2}{4}, \qquad \gamma = \frac{1}{2} + a \tag{3-6}$$

3.1.3 Finite element constitution

In this study, the mechanical behavior of a sea-based fish farming system is modeled using a one-dimensional finite element known as "CABLE" in the structural solver. This element was originally created to examine overhead power lines and is completely flexible, unsuitable for sustaining any bending forces or twisting. Because it allows for significant displacements in nonlinear dynamic analysis, the CABLE element is well suited for modelling very flexible line-like structures. (Antonutti *et al.*, 2018). As a result, it is ideal for simulating cable and nets in an aquaculture system. In addition, the sinker tube and floating collar are modeled using a one-dimensional beam element.

3.1.4 Mesh grouping

The netting in full-scale fish cages is often made up of multiple small twines, making it impractical to build a numerical model twine by twine. To reduce computing complexity, a mesh grouping method is widely utilized throughout the spatial discretization process. (Cheng et al., 2018); Zhao *et al.*, 2007). In our current structural model, we assume that the numerical model's material properties are similar to those of the physical net. The values of $\boldsymbol{M}$, $\boldsymbol{K}$, $\boldsymbol{F_b}$, $\boldsymbol{F_g}$ and $\boldsymbol{F_h}$ in Eq. (3-2) must be consistent between the physical and numerical nets to ensure

accurate results. To ensure this consistency, we use three derived diameters during the spatial discretization process: structural diameter (d_{ws}), elastic diameter (d_{we}), and hydrodynamic diameter (d_{wh}). These diameters and their relationships with the physical twine diameter (d_{w0}) are presented as:

$$\lambda = L_s/L_0 \; ; d_{ws} \approx \lambda d_{w0} \; ; d_{wh} \approx \lambda d_{w0} \tag{3-7}$$

where λ is the ratio between the half mesh size of the numerical net (Ls) and the half mesh size of the physical net (L_0). For a full-scale fish farm facility, λ is usually in the range of 20 to 80.

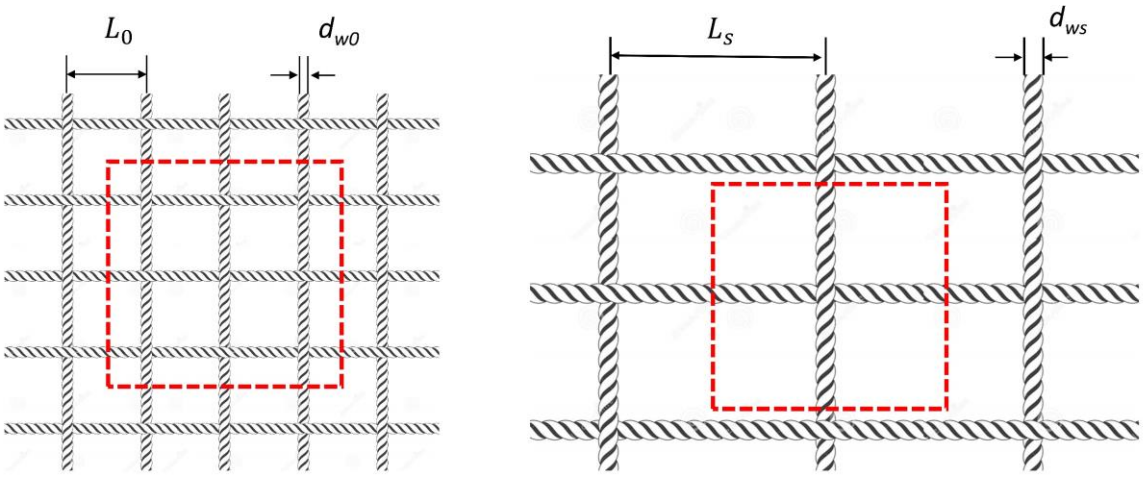

Figure 3- 2: Illustration of the mesh grouping method.

The numerical model's fluid velocity ($\boldsymbol{u}$), density of twine (ρ_{twine}), and Young's modulus of twine (E) are consistent with the physical value, and λ is the ratio between the numerical net's half mesh size (Ls) and the physical net's half mesh size (L_0).

The nets in the two red dashed boxes should have the same mass ($\boldsymbol{M}$), as shown in Figure 3-2. The structural diameter (d_{ws}) is employed in the numerical model building to ensure uniformity. The correlations between structural diameter and physical twine diameter (d_{w0}) are deduced further below.

3.1.4.1 Mass equivalent

As shown in Figure 3-2, the mass of the physical net in the red dashed box is:

$$M_0 = \rho_{twine}\lambda^2 \frac{\pi}{4} {d_{w0}}^2 (2L_0 - d_{w0}) \tag{3-8}$$

And the mass of the numerical net in the red dashed box is:

$$M_s = \rho_{twine} \frac{\pi}{4} {d_{ws}}^2 (2L_s - d_{ws}) \tag{3-9}$$

Because $M_0 = M_s$, the structural diameter d_{ws} should satisfy:

$$d_{ws} = \lambda d_{w0} \sqrt{\frac{2L_0 - d_{w0}}{2L_s - d_{ws}}} \tag{3-10}$$

For typical aquaculture nets, $2L_0 \gg d_{w0}$ and $2L_s \gg d_{ws}$.Therefore, the square root term can be simplified as:

$$\sqrt{\frac{2L_0 - d_{w0}}{2L_s - d_{ws}}} \approx \sqrt{\frac{1}{\lambda}} \tag{3-11}$$

Then the structural diameter can be obtained as:

$$d_{ws} \approx \lambda d_{w0} \tag{3-12}$$

3.2 Fluid model

3.2.1 Governing equations

The present study employs the Finite Volume Method (FVM) to solve the flow field surrounding fish cages. The fluid domain is discretized into a grid of cells, and the governing equations for mass and momentum conservation are presented as Eqs. (3-13) and (3-14), respectively.

$$\frac{\partial \rho}{\partial t} + \frac{\partial u_i}{\partial x_i} = 0 \tag{3-13}$$

$$\frac{\partial}{\partial t}(\rho u_i) + \frac{\partial}{\partial x_j}(\rho u_i u_j) = -\frac{\partial P}{\partial x_i} + \frac{\partial}{\partial x_j}[\mu \frac{\partial u_i}{\partial x_j}] + S_{pz} \tag{3-14}$$

The velocity of the stream is represented by $\boldsymbol{u}$, while the pressure is represented by P. The flowing viscosity is denoted by μ, and the density of the fluid is given by ρ .The source term, $\boldsymbol{S_{pz}}$, is used to account for the resistance force from nets. This term is zero for most of the computational domain and only has non-zero value in the exact cells belonging to nets. A dynamic porous media (DPM) model is developed to identify these cells and calculate the appropriate $\boldsymbol{S_{pz}}$ values.

The Reynolds number, a dimensionless parameter obtained from the ratio of input velocity, turbulence length scale, and kinematic viscosity. A Reynolds number of 12 500 000 was specified for the cage diameter (Re_c), indicating a turbulent wake flow regime. Similarly, a Reynolds number of 675 was chosen for the twine diameter (Re_t), indicating a turbulent wake flow regime. These variables were chosen to ensure proper fluid dynamics characterization in the numerical setup.

The modeling of turbulent flow is a complex phenomenon that has been extensively researched in recent decades. Among the most widely used turbulence models are the *k-ε, k-ω*, *k-ω* SST, and realizable *k-ε* models, which have been compared by Chen and Christensen (2017) in terms of their ability to predict flow velocities in the wake. Their study found that all four models produced similar results for flow velocities in the wake, indicating their capability to accurately predict such velocities. Considering these findings, the *k-ω* SST model was selected as the turbulent closure model for the present study due to its demonstrated accuracy in predicting wake flow velocities.

3.2.2 k-ω SST turbulence model

The *k-ω* Shear Stress Transport (SST) model was created to combine the best characteristics of both the *k-ε* and *k-ω* models. Menter *et al*. (1992, 1997) integrated the low sensitivity of the *k-ε* model in the free stream into the *k-ω* SST model. The *k-ε* model, on the other hand, has been shown to over-predict instances with adverse pressure gradients in the near-boundary layer. To overcome this limitation, Menter *et al*. (1992, 1997) used the *k-ω* model

in the near-wall area and used the relationship between ε and k ω to transform the ε -equation into the ω -equation. For the computation of Reynolds stress and the k-equation, the k- ω SST model follows the same method as Wilcox's (1988, 1994) original k-ω model.

Menter *et al*. (2003)'s k-ω SST model has been modified for use with general-purpose computation models. This revised model includes changes to the model constant, blending function, and limiters. Because of differences in eddy viscosity, the standard k-ε model is known to induce numerical instability. The blending function is used to transition from the standard k-ε model in the far field to the k-ω model near the wall to resolve this problem. Notably, the transport equation in this model contains an extra source term, *i.e.,* cross diffusion, which is not present in Wilcox (1988, 1994)'s k-ω model. We use Menter *et al*. (2003)'s k-ω SST model in this research, which allows us to express the turbulent kinetic energy and specific dissipation rate as follows:

$$\frac{\partial(\rho k)}{\partial t}+\frac{\partial(\rho U_i k)}{\partial x_i}=P_k-\beta^*\rho k\omega+\frac{\partial}{\partial x_i}\left[(\mu+\sigma_k\mu_T)\frac{\partial k}{\partial x_i}\right] \tag{3-15}$$

$$\frac{\partial(\rho\omega)}{\partial t}+\frac{\partial(\rho U_i\omega)}{\partial x_i}= \\ \alpha\rho S^2-\beta\rho\omega^2+\frac{\partial}{\partial x_i}\left[(\mu+\sigma_\omega\mu_T)\frac{\partial\omega}{\partial x_i}\right]+2(1-F_1)\rho\sigma_{\omega_2}\frac{1}{\omega}\frac{\partial k}{\partial x_i}\frac{\partial\omega}{\partial x_i} \tag{3-16}$$

where the blending function F_1 is defined by:

$$F_1=\tanh\left\{\left\{\min\left[\max\left(\frac{\sqrt{k}}{\beta^*\omega y},\frac{500\nu}{y^2\omega}\right),\frac{4\rho\sigma_{\omega_2}k}{\mathrm{CD}_{k\omega}y^2}\right]\right\}\right\} \tag{3-17}$$

with $CD_{k\omega}=\max\left(2\rho\sigma_{\omega_2}\frac{1}{\omega}\frac{dk}{\partial x_i}\frac{d\omega}{\partial x_i},10^{-10}\right)$ and y is the distance to the nearest wall. F_1 is equal to zero away from the surface (k-ε model) and switches over to one inside the boundary layer (k-ω model).

The turbulent eddy viscosity is defined as follows:

$$\nu_T = \frac{\alpha_1 k}{\max(\alpha_1 \omega, SF_2)} \tag{3-18}$$

Where $\boldsymbol{S}$ is the strain rate invariant measure and F_2 is the second blending function defined as:

$$F_2 = \tanh\left[\left[\max\left(\frac{2\sqrt{k}}{\beta^* \omega y}, \frac{500\nu}{y^2 \omega}\right)\right]^2\right] \tag{3-19}$$

The SST model employs a production limiter to prevent the accumulation of turbulence in stagnation regions:

$$P_k = \mu_T \frac{\partial U_i}{\partial x_j}\left(\frac{\partial U_i}{\partial x_j} + \frac{\partial U_j}{\partial x_i}\right) \longrightarrow \widetilde{P_k} = \min(P_k, 10.\beta^* \rho k \omega) \tag{3-20}$$

All constants are computed by a blend of the k-ε and k-ω model constants via $\alpha = \alpha_1 F + \alpha_2(1 - F)$ and so on.

The constants for this model are shown in Table 3-1.

Table 3-1: The constants for Menter *et al*. (2003)'s k-ω SST model.

α_1	β_1	σ_{k_1}	σ_{ω_1}	β^*	α_2	β_2	σ_{k_2}	σ_{ω_2}
5/9	3/40	0.85	0.5	0.09	0.44	0.0828	1	0.5

3.2.3 Dynamic porous media model

In the current study, we utilized a dynamic porous media (DPM) model to govern the porous zones, which represent nets within the fluid domain. The DPM model serves two primary purposes, namely (1) identification of the cells belonging to the porous zones, and (2) allocation of the appropriate $\boldsymbol{S_{pz}}$ to the corresponding cells.

In order to represent the deformation of nets in fluid, a topological method is needed to map the Lagrangian nodes to the Eulerian grids. As the nets are flexible and can have violent movements under strong current flows, it is challenging for the fluid solver to identify the positions of the net panels. The virtual net panels with different α and the direction of the hydrodynamic load are shown in Figure 3-3. Where α present angle between net panels.

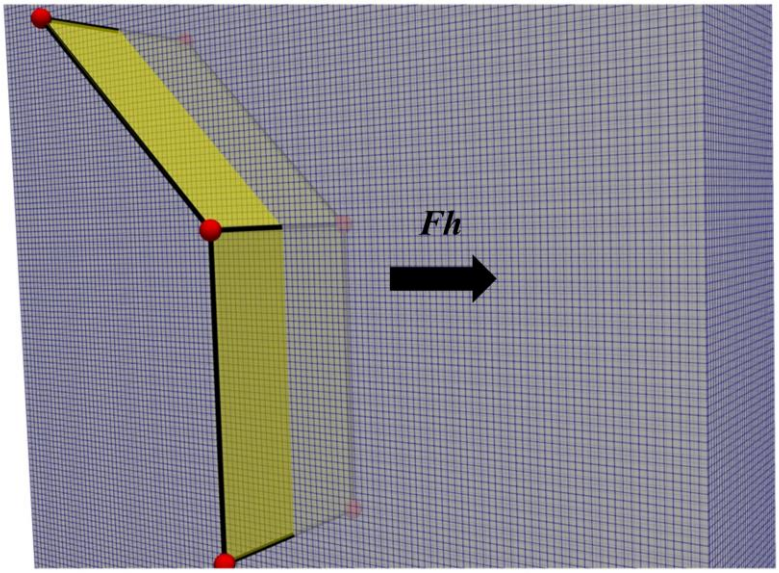

Figure 3- 3**:** Hydrodynamic force on the virtual net panels with different α.

3.2.4 Calculation of the source term *Spz*

The presence of nets in the computational domain is represented by a source term, $\boldsymbol{S_{pz}}$. The value of $\boldsymbol{S_{pz}}$ in this research is determined based on the conservation of momentum, as proposed by Cheng *et al*. (2022). Using Newton's Third Law, we can show that the hydrodynamic loads acting on the nets are identical in magnitude but opposite in direction to the fluid's resistance forces. As a result, we can use Eq. (3-21), which involves a volume integral over the porous zone, to describe the relationship between the hydrodynamic loads on a single net panel and the loss of fluid momentum in the corresponding porous zone.

When the value of $\boldsymbol{S_{pz}}$ in Eq. (3-21) remains constant across cells in a porous zone, the volume integral on the left-hand side of the equation can be simplified as the product of the porous zone's volume (TA_t) and $\boldsymbol{S_{pz}}$. This simplification is demonstrated in Eq. (3-22). On the right-hand side of Eq. (3-22), the hydrodynamic loads $\boldsymbol{F_h = F_D + F_L}$ are calculated using Eq.

(2-26) through (2-29). Together with Eq. (3-24), the value of source term in one fluid cell with a volume of V_i can be written as Eq. (3-23) for convenience.

$$\iiint_{V} \rho_w \boldsymbol{S_{pz}}\, \boldsymbol{dxdydz} = -\boldsymbol{F_h} \tag{3-21}$$

$$\rho_w T A_t \boldsymbol{S_{pz}} = -\boldsymbol{F_h} \tag{3-22}$$

$$\boldsymbol{S_{pz}} = \frac{-\boldsymbol{F_h}}{\rho_w T A_t} V_i = -\frac{1}{2}\left|\sqrt{\frac{2}{2-(C_D+C_L)}}\boldsymbol{U_c} - \boldsymbol{v}\right|^2 \frac{C_D \boldsymbol{i_D} + C_L \boldsymbol{i_L}}{T} V_i \tag{3-23}$$

3.3 Hydrodynamic force models

3.3.1 Hydrodynamic force on net structure (Screen type force model)

The Screen model, as introduced by Løland (1991), is used in this research to calculate the hydrodynamic loads acting on a net panel. According to Cheng *et al*. (2020) the Screen model is theoretically better to the Morison model due to its implicit consideration of twine-to-twine interactions in force calculations. The hydrodynamic loads are classified into drag and lift forces based on the direction of fluid velocity, which are written as $\boldsymbol{F_D}$ and $\boldsymbol{F_L}$ in equations (2-26) through (2-29). Figure 3-4 illustrates a virtual panel element for calculating hydrodynamic forces in the present study.

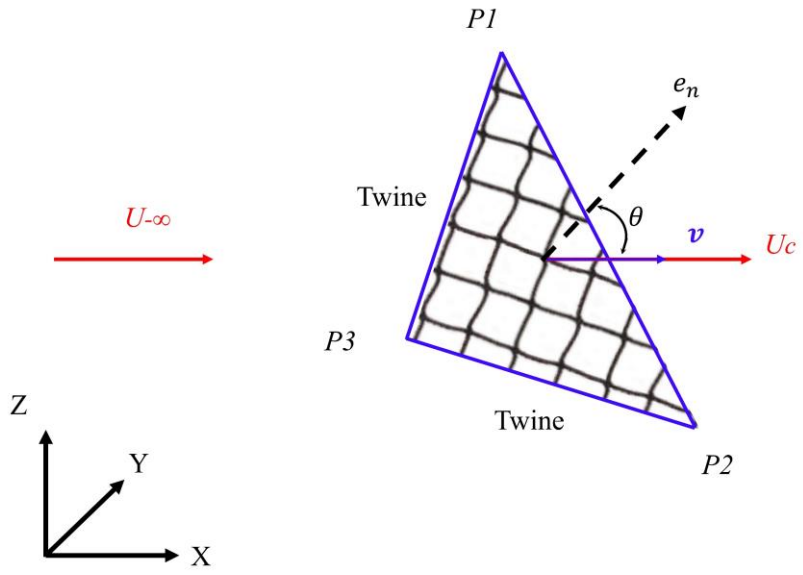

Figure 3- 4: Illustration of a virtual panel. The inflow angle θ of the virtual panel element is defined as the angle between $\boldsymbol{e_n}$ and $\boldsymbol{Uc}$.

It is widely accepted that force coefficients (*i.e.,* C_D and C_L) are determined experimentally in order to model the ideal conditions of a finite net panel in an infinite flow field. Nonetheless, it is generally acknowledged that achieving these ideal conditions in practical uses can be difficult.

It is commonly acknowledged that existing hydrodynamic force models rely on the measurement of the undisturbed flow velocity $\boldsymbol{U}_{-\infty}$ in laboratory experiments to derive force coefficients. However, in the case of nets positioned at various locations on an aquaculture structure, wake effects can cause variations in $\boldsymbol{U}_{-\infty}$ **,** making it difficult to calculate hydrodynamic forces on the nets correctly. In this research, a fluid model was used to solve the wake effects, allowing for direct extraction of the flow velocity at the centroid of a virtual panel element $\boldsymbol{U_C}$ from the fluid solver. As shown in Eq. (3-24), the existing hydrodynamic force model was modified by expressing $\boldsymbol{U}_{-\infty}$ in terms of $\boldsymbol{U_C}$, with detailed derivations given by Cheng *et al.* (2022).

$$\boldsymbol{U_{-\infty}} = \sqrt{\frac{2}{2-(C_D+C_L)}}\,\boldsymbol{U_c} \tag{3-24}$$

3.3.2 Hydrodynamic force on the mooring system (Morison type force model)

The Morison type hydrodynamic force model can be applied to a line like structure, such as rope, cable, chain, and pipe. Using Morison's equation, the hydrodynamic forces on each line-like structure are calculated and added to determine the overall drag force of the mooring system. In practice, the environmental load on the line-like structure is usually decomposed into two components: normal drag ($\boldsymbol{Fn}$, Eq. (2-24)) and tangential drag ($\boldsymbol{Ft}$, Eq. (2-25)).

The Morison model has a benefit due to its format. The application of a Morison model is immediately compatible with the structural model because the formulation of the Morison mode coincides with the line-like elements in structural models. As a result, it is simple to incorporate the Morison model into FEM programs to compute hydrodynamic loads. Additionally, the Morison model is readily adaptable to a variety of line-like marine structures, including ropes, cables, and mooring lines.

3.4 Coupling algorithm

In the study by Cheng *et al.* (2022), it was observed that both solvers used in the research, Code_Aster and OpenFOAM, are open source and written in an object-oriented manner. This feature enabled the possibility of coupling the two solvers to investigate the fluid-structure interaction (FSI) problem. To achieve this, an in-house module was developed to facilitate information exchange between the solvers. The coupling process involved a two-way coupling algorithm, which is depicted in Figure 3-5. The main procedures of this algorithm are as follows:

1. Two open-source solvers, Code_Aster and OpenFOAM, import the physical parameters from a dictionary file and build up the model based on the net setup to begin the simulations. The fluid solver generates porous zones during initialization, while the structural solver generates virtual net panels.
2. In the fluid solver, the flow field is solved using the PISO algorithm.
3. The fluid solver is used to extract velocities in the porous zones, and the Screen model uses these corrected velocities (Eq.3-24) to calculate hydrodynamic forces on the nets.
4. The hydrodynamic forces on the nets are projected onto the structural nodes.
5. The HHT-α algorithm estimates the position of each structural node based on the received hydrodynamic forces.
6. Using Eq. (3-23), the DPM model updates the geometries of porous zones and the ***Spz*** value in fluid cells.
7. Finally, the fluid solver recalculates the flow field using the revised porous zones, resulting in a loop that solves the FSI problem.
8. This results in a complete loop for solving the FSI problem, beginning with loading physical data and initializing the model and ending with recalculating the flow field with the updated porous zones.

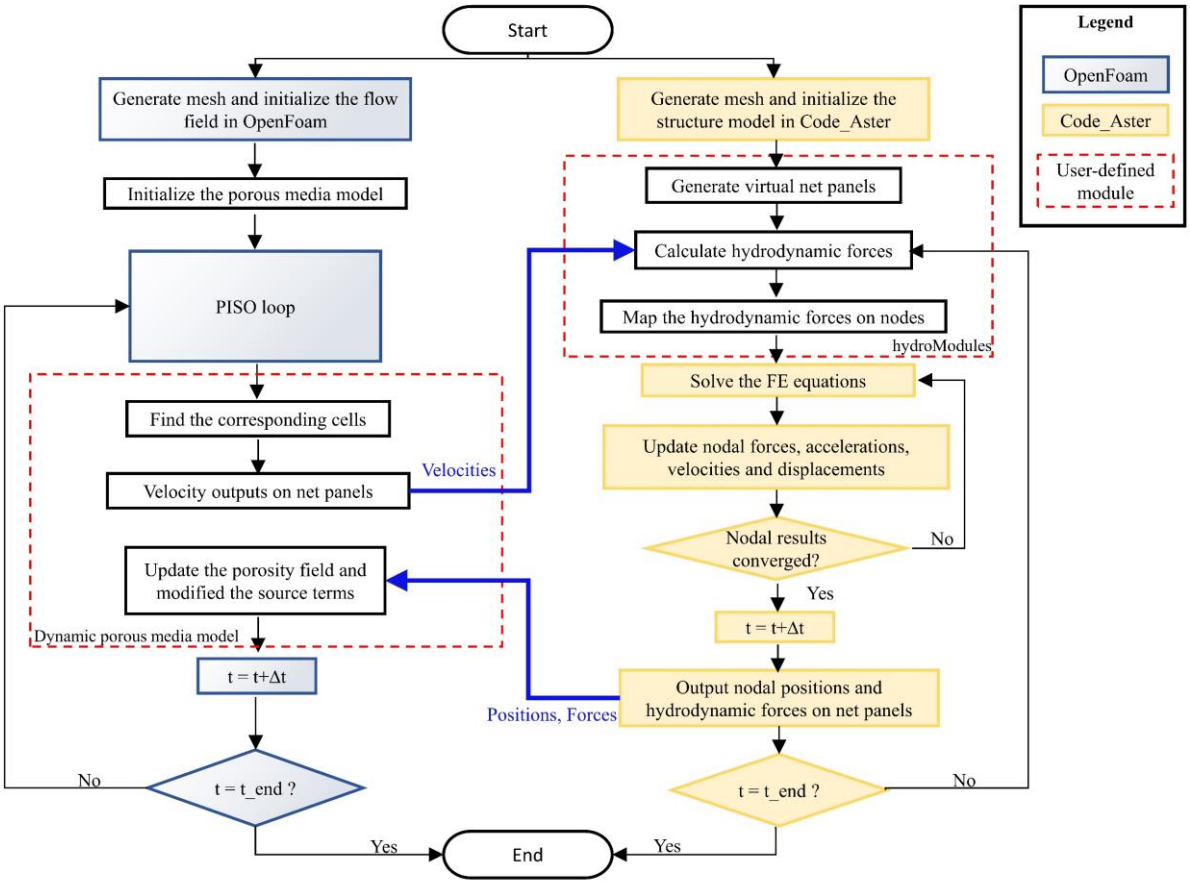

Figure 3- 5: Flow chart of the coupling algorithm.

3.5 Model setup

The open-source finite volume method CFD code OpenFOAM v2012 is used in this study to solve the governing equations for the flow field, and the finite element solver Code_Aster is used to solve the governing equation for structure reactions. The Hilber-Hughes-Taylor-α (HHT-α) approach is used to solve nonlinear dynamic equation motions. The k- SST model is used for RANS simulation, and the flow field is calculated using the Pressure Implicit with Splitting of Operator (PISO) technique. For the discretization of transient terms, the Euler implicit time scheme is used, and the Laplacian scheme is Gauss linear corrected; the divergence is Gauss linear, bounded Gauss limited linear, and Gauss limited linear. All simulations are carried out in three-dimensional identical fluid environments with varying flow directions. The initial fluid boundary conditions are presented in the Table 3-2. Patursson's (2008) numerical results are unaffected by near-wall treatment when nets are far away from the walls. As a result, *u* is assigned as a slip condition for the wall boundary.

Table 3-2: The initial boundary conditions for fluid domain.

Surface domain	Left	Right	Top, Bottom, Front, Back
Patch type	Patch	Patch	Wall
Pressure, P	Zero normal gradient	Fixed zero pressure	Zero normal gradient
Velocity, U	Fixed value	Zero normal gradient	Slip condition
Omega, ω	Fixed value	Fixed value	Zero normal gradient
K	Fixed value	Fixed value	Zero normal gradient
Nut	Calculated	Calculated	Calculated

Chapter 4*

Wake effects on the drag force estimation of downstream fish cages

* The contents of this chapter are included in the paper Cheng *et al.* (2023) which is accepted for publication in Proceedings of the ASME 2023 42nd International Conference on Ocean, Offshore and Arctic Engineering OMAE2023.

4.1 Computational setup

The numerical model uses a coordinate system where x is positive in the flow direction, y is perpendicular to the flow direction on the horizontal plane, and z is upward (Figure 4-1). The dimensions of the numerical flume are 15D long, 10D wide, and 1D deep. To investigate the influence of the upstream fish cage on the downstream fish cage, as well as the drag force on both cages, the study considers the relative position of the second cage and solidity. Nineteen cage positions (α is from 0° to 90° with a 5° interval) and three different solidity ratios (Sn = 0.10, 0.18, and 0.25) are investigated in a uniform current with a flow velocity of 0.2 m/s. The distance between the two cages is kept as 2D. The numerical flume is used to conduct a time-dependent simulation of 16 s for each cage position. Figure 4-1 shows the setup of the coordinate system and cage positions.

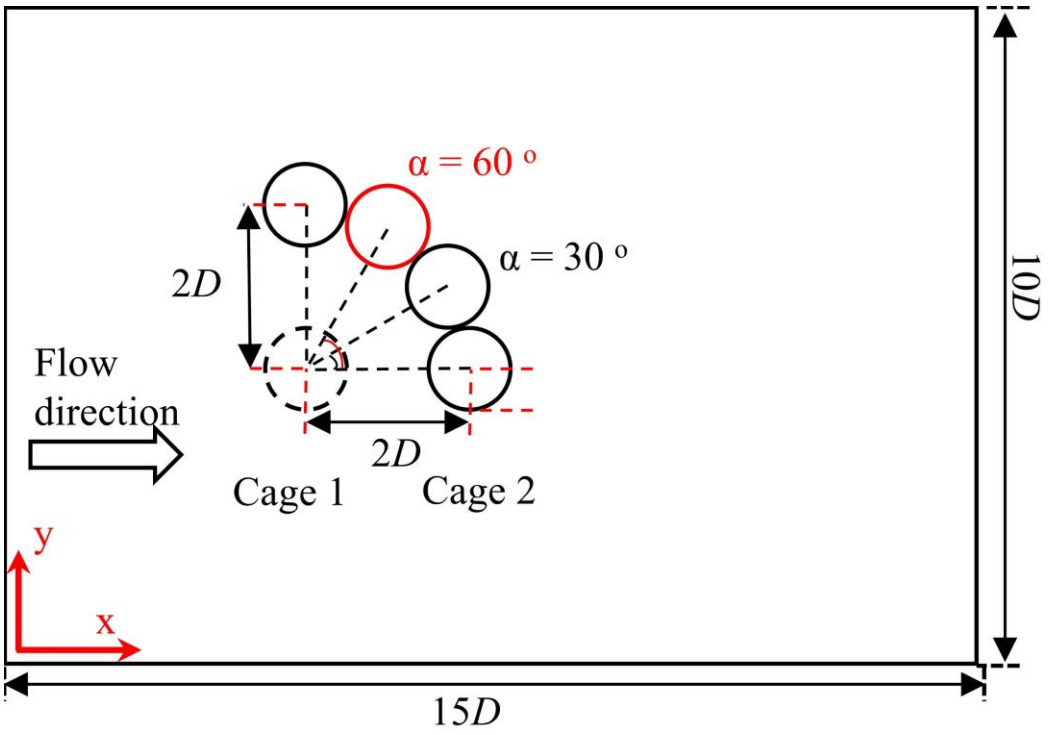

Figure 4- 1: Illustration of the computational domain and the relative position of the second fish cage.

4.2 Results and discussion

4.2.1 Convergence study

In this study, simulations have been carried out to reach a steady state flow field for simulation. Figure 4-2 gives the time history for drag force on single fish cage. The present results show that the single fish cage converges stable value approximately after 2 s.

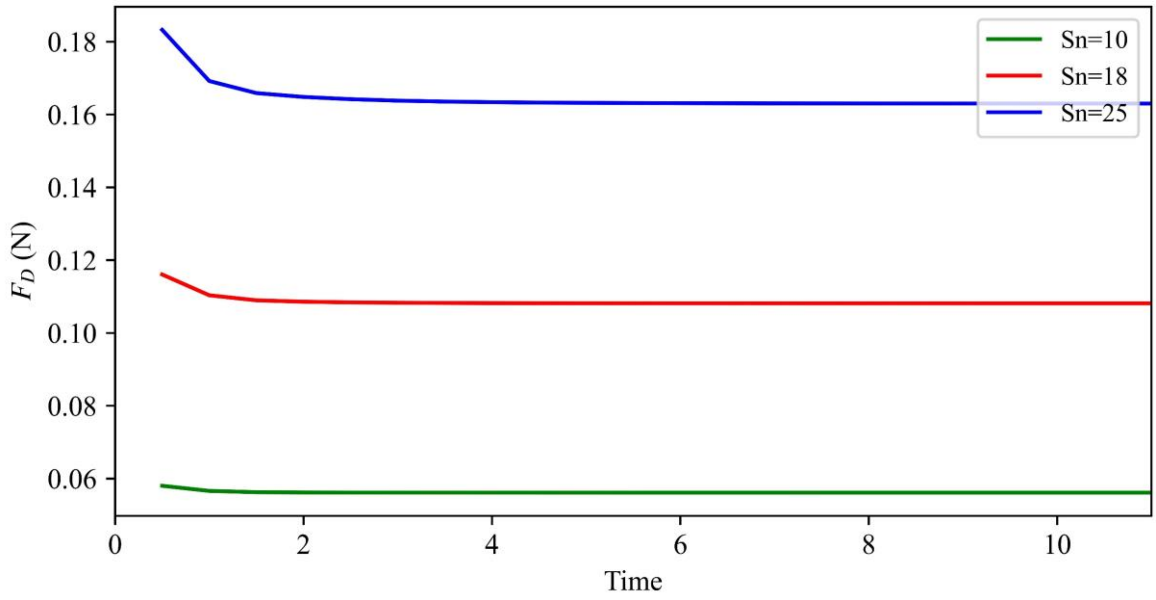

Figure 4- 2: Drag force on single fish cage.

A series of simulations with different mesh resolutions have been carried out for the mesh convergence study. The purpose is to find the threshold of mesh size for sufficient numerical accuracy. In the present study, uniform hexahedral orthogonal meshes (*i.e.*, $\Delta x=\Delta y=\Delta z$) are used to discretize the fluid domain. The porous zone thickness has no significant effect on the simulation results (Patursson *et al*., 2010). However, the resolution of the cell grid across the porous zone may affect the simulation results (Chen and Christensen, 2016). Therefore, a mesh convergence study is performed with a constant $T/\Delta x$, where Δx is the cell size and T is the thickness of the porous zone. The grid convergence is executed by refining the flow field around the porous media zone with five mesh sets (M1-M5) as shown in Table 4-1.

Table 4- 1: Number of the cells, cell size and porous zone thickness, cell size ratio in x -direction.

Grid	Number of Cells	Δx(mm)	$T/\Delta x$
M1	425 000	6	2
M2	720 000	5	2
M3	1 406 250	4	2
M4	3 300 000	3	2
M5	11 250 000	2	2

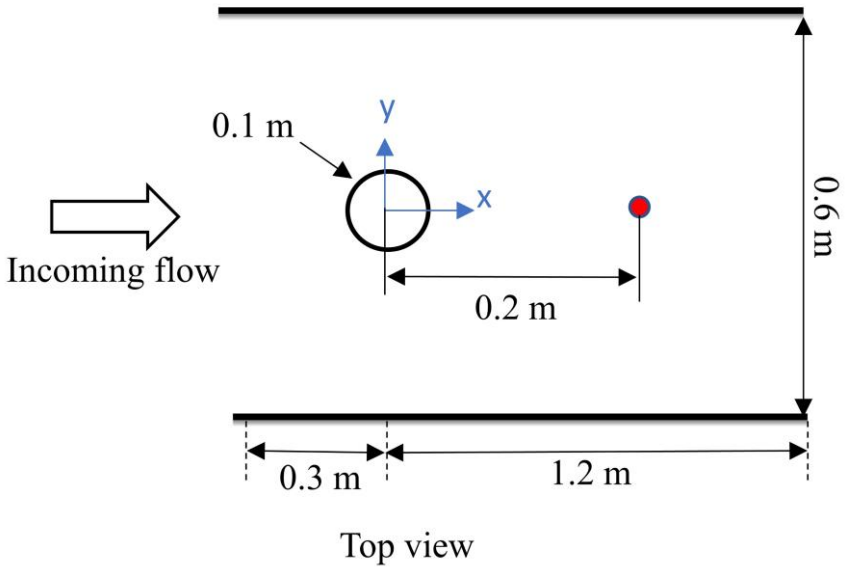

Figure 4- 3: Sketch of the fluid domain or reproduction of experiment by (Gansel et al., 2012).

The results of the mesh convergence study are shown in Table 4-2. The flow velocity in the wake region $\boldsymbol{u^*}$ is extracted from the red spot in Figure 4-3, and the drag force $\boldsymbol{F_D}$ is calculated as integral of the loads on the fish cage. The discrepancy in Table 4-2 is calculated based on the finest mesh resolution (M5). For the flow velocity in the wake region, the results from all the studied mesh sizes have discrepancies less than 4%. In particular, M2 has the least discrepancy 0.18%. For the drag force, the results from all the studied mesh sizes have discrepancies less 3.6%. M2 an M4 has the smallest discrepancies. With the consideration of both flow velocity and drag force, M2 is selected as the mesh resolutions for the subsequent simulations.

Table 4- 2: Result of convergence study for cylinder.

Grid	u^*	Discrepancy	F_D	Discrepancy
M1	0.146671	3.9%	0.1575	3.6%
M2	0.140855	0.18%	0.1663	1.7%
M3	0.145523	3.1%	0.1583	3.1%
M4	0.146270	3.6%	0.1662	1.6%
M5	0.141114	---	0.1635	---

u^*: flow velocity at the red circle in Figure4-3

The time-step convergence study is also performed for the nets in pure currents. The conclusion is similar to the research by Cheng *et al.* (2020), where four time steps Δt, *i.e.*, 0.02s, 0.05s, 0.1s and 0.2s, were applied. Since the simulations are calculated under pure current conditions without any oscillating loads, the above time steps have negligible influences on the final results. Thus, Δt = 0.1s was selected for the subsequent simulations with the consideration of Courant-Friedrichs-Lewy (CFL) number. In the following simulations, the maximum CFL number is 0.8.

4.2.2 Validation Study

The validation study is carried out based on the experimental results from Gansel *et al*. (2012). The experimental models in Gansel *et al*. (2012) were porous cylindrical structure that has a fish cage shape. And all these models were made from the same solid metal string but variant solidities (*i.e., Sn* = 1.0, 0.25, 0.18, and 0.1). The models had a diameter (*D*) of 0.1 m and a length (*L*) of 0.3 m. The tests were carried out in a towing tank with pure current conditions. The towing tank was 13.5 m long, 0.6 m wide, and 1.5 m deep, and the towing speed was within the range of 0.05–0.2 m/s. As shown in Figure 4-3, the computational domain in the present study has the same dimension as the towing tank in Gansel *et al*. (2012).

As shown in Figure 4-4, the velocity defect (*Uinf-u* [m/s]) profiles from the experimental results by Gansel *et al*. (2012) and the present numerical results are compared. According to the comparison, the present numerical simulations are in good agreement with the experimental data. With the increase of the solidity, the present numerical results are closer to the experimental data under the same environmental condition.

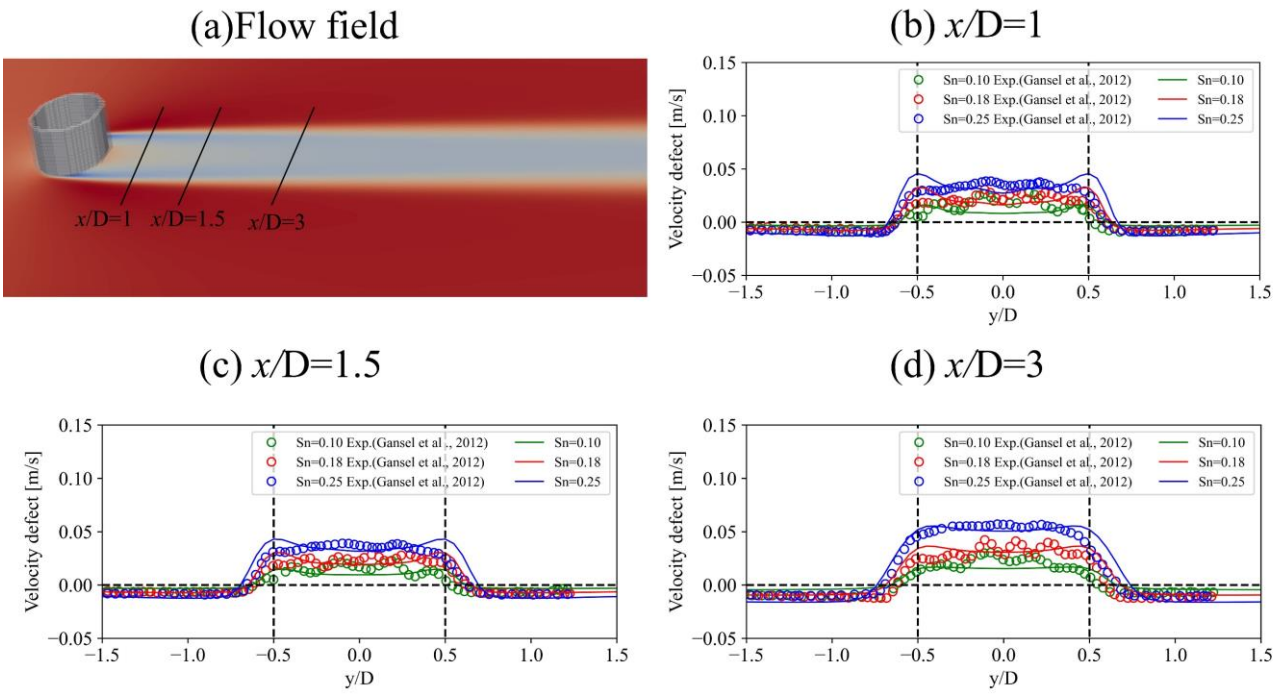

Figure 4- 4: Velocity defect [m/s] in the wake of a porous cylinder at different locations downstream from the centerline of the cylinder with Sn = 0.10, 0.18, 0.25. The towing speed was 0.2 m/s.

4.2.3 Drag Forces on the Downstream Fish Cage at Different Locations

Figure 4-5 shows the normalized drag force of the two fish cages. The normalization is calculated as the ratio of the drag force on Cage1 to the drag force on Cage2. As shown in Figure 4-5, the drag forces on the downstream fish cage first increase then decrease with the increasing α, and finally match with the drag force on the upstream cage. When $\alpha < 30°$, the drag force on the downstream fish cage is smaller than the upstream fish cage due to the flow reduction caused by the wake effect. When the position of the downstream fish cage is located between $\alpha = 30°$ and $\alpha = 70°$, the downstream fish cage experiences increased velocity. That increased velocity is caused by the upstream fish cage and can be explained by the law of mass conservation. The net, although is high permeability, can still partly block the water flow passing through the fish cage. This blockage effect can lead the water flow go around the fish cage and cause a velocity increment. Subsequently, the drag force on the downstream fish cage is larger than that on the upstream cage. When $a > 70°$, the interactions between the upstream cage and the downstream cage become insignificant, and the drag forces on these two cages are close to each other. Finally, when $a = 90°$, the drag forces on the two cages are the same.

Solidity (Sn) is one of the important parameters that can influence the environmental loads on fish cages. Since Sn plays an important role in drag and lift coefficients (Løland 1991), cages with different Sn can experience different loads and also affect the surrounding flow field in different levels. According to Figure 4-5, when $\alpha = 0°$, with the increase of the solidity, the second fish cage will experience lower velocity and lower drag force. When Sn = 0.10, 0.18 and 0.25, the drag force on the downstream fish cage is reduced by 21%, 37%, and 51%, respectively, compared to the upstream fish cage.

The present study also discovers that the drag force on the upstream cage is slightly changed with the changing position of Cage2. The total load on Cage1 is dependent on the pressure distribution in both front and rear parts. The pressures in the front part of Cage1 are almost constant in this series of numerical simulations, since Cage1 always faces the same undisturbed flow velocity. However, the pressures in the rear part of Cage1 can be different due to the influence of Cage2. Thus, the drag force on Cage1 will change with the positions of Cage2.

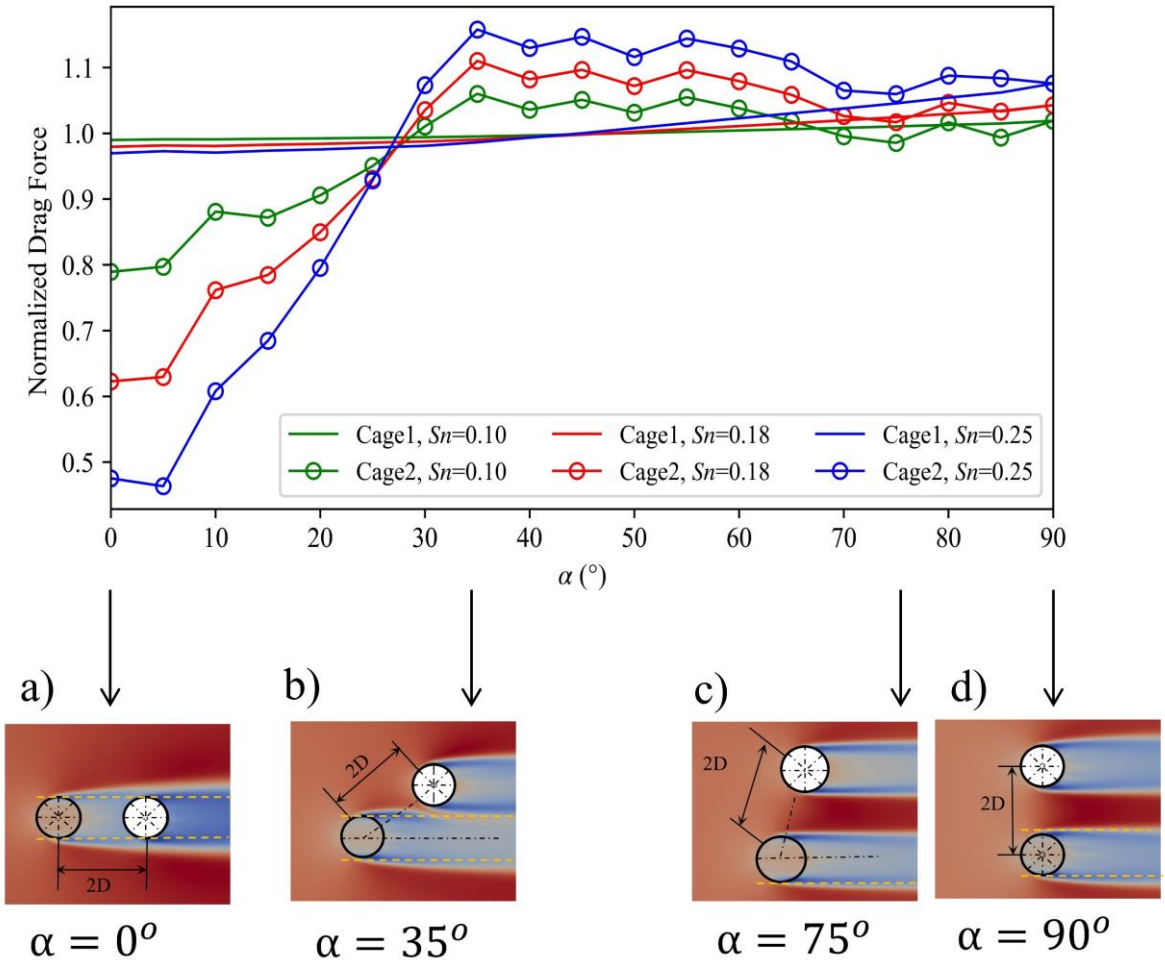

Figure 4- 5: Normalized drag force.

According to Sim *et al.* (2021), the flow velocity in the wake region is symmetrical about the Y=0 plane. With the increasing distance to the plane of symmetry, the flow velocity first decreases then becomes steady. The flow velocity reaches the undisturbed incoming velocity around Y= 0.65D. When the distance to the axis of plane exceeds 0.65D, the flow velocity is slightly higher than the undisturbed incoming velocity due to the conservation of mass. In addition, the study by Sim *et al.* (2021) concluded that the influence of the upstream cage on the flow field around the downstream cages will become negligible when $\alpha > 48.6°$, as illustrated in Figure4-6.

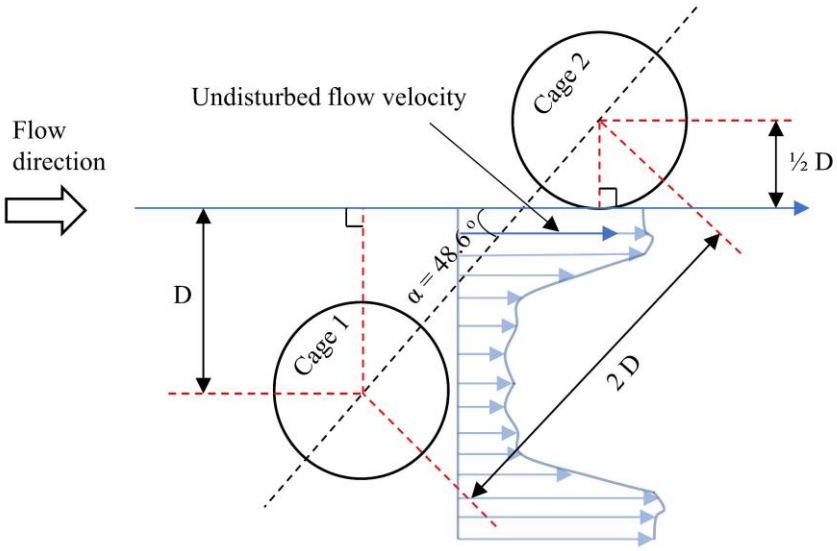

Figure 4- 6: Illustration of the velocity profile after upstream cage with 48.6 ^{0} downstream cage position (Sim et al. 2021).

In contrast to Sim *et al.* (2021), the flow field in the present study is calculated using CFD method rather than the simple velocity superposition. Thus, the flow field around the studied fish cages can be investigated in a more detailed way. As shown in Figure 4-7, the velocity transitions between the low and high flow velocity regions around the two studied fish cages are smoother than the results by Sim *et al*. (2021). Moreover, different to the conclusion from Sim *et al*. (2021), the present numerical results indicate that the wake effect on the downstream fish cage exists until $\alpha = 70°$. This contrast will cause significant differences on the drag force estimations for the downstream fish cages as well as on the total drag force estimations for the whole fish farm.

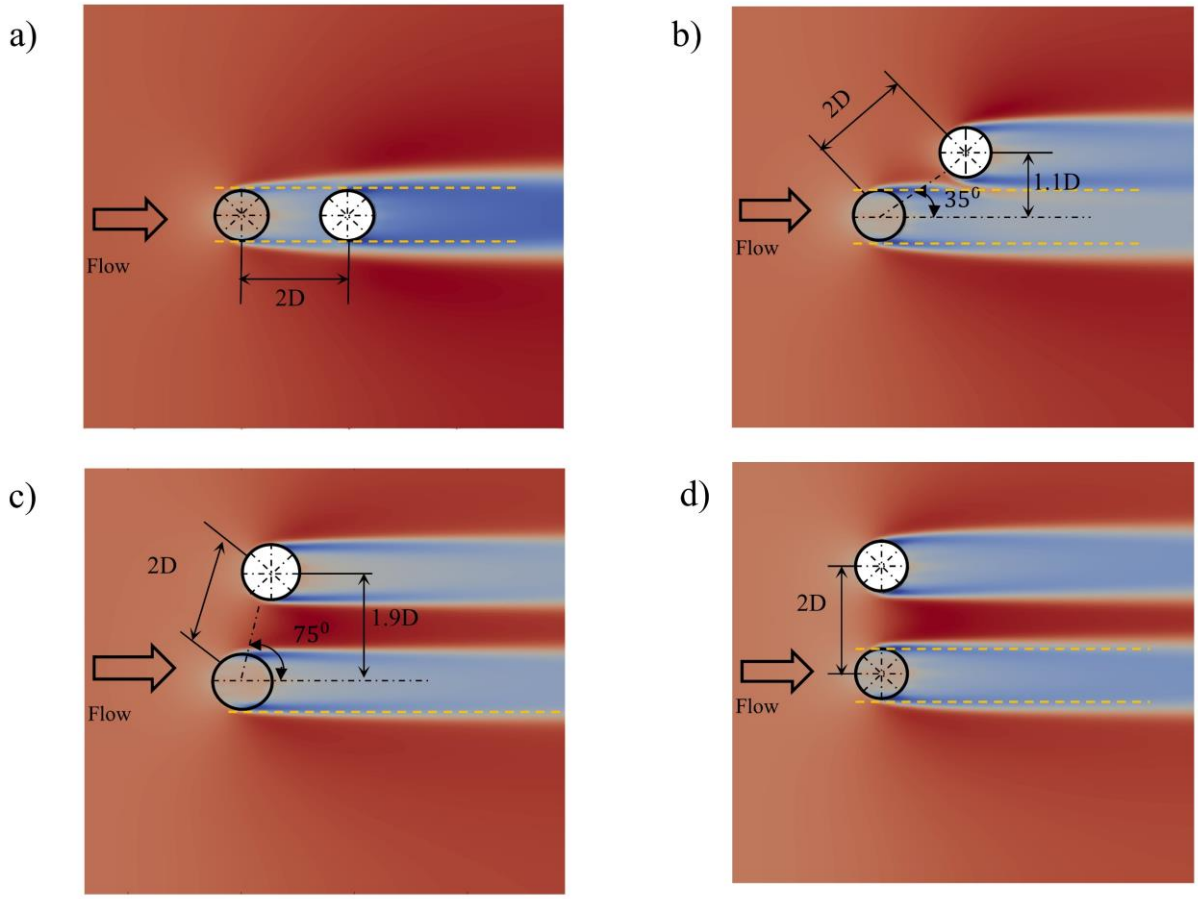

Figure 4- 7: Illustration of the typical flow fields around the two fish cages with SN=0.25: A) =0 °, B) =35°, C) = 75° and D) = 90°.

4.3 Summary

This study investigates the flow field through and around fish cages using CFD method. The wake effects on the drag force estimations are studied in detail. The main conclusions are summarized as follows:

(1) The drag forces on the downstream fish cage are not always smaller than that on the upstream fish cage. When the position of the downstream fish cage is between $\alpha = 30°$ and $\alpha = 70°$, the drag forces on the downstream fish cage can be larger than that on the upstream one, due to the relative higher flow velocity caused by the blockage effects.

(2) Higher solidity can cause a larger drag force on fish cage, a larger flow velocity reduction in the wake region, and also a higher flow velocity increase beside the wake region.

(3) The drag force on the upstream fish cage can also be affected by the existence of downstream fish cages, as the pressure distribution in the rear parts of the upstream fish cage can be altered by the downstream fish cage.

Chapter 5*

A Comparative Study of Two Fish Farm Layouts under Pure Current Conditions

*The contents of this chapter are included in the paper which will be submitted to Aquacultural Engineering for possible publication.

5.1. Computational setup

5.1.1 Cage configuration

The target of examination in this study was a flexible gravity-based fish cage, which is the most often utilized type in the aquaculture industry. A net framework, a floating collar, a sinker tube, and a mooring system compose the fish cage. Table 5-1 shows the size and material attributes of the single-cage model utilized in the numerical simulations.

The numerical model in the present study is based on a coordinate system in which the z-axis is upward, as shown in Figures 5-1 and 5-2. The dimension of the numerical flume is 8 D (where D is the diameter of the cage) in long, 8 D in wide, and 1.6 D in deep. In the study, two different fish farming layouts are used: a 2 × 3 Array and a new design (Honeycomb) with six cages. Figures 5-1 and 5-2 illustrates the coordinate system as well as the positions of cages in the 2 × 3 Array and Honeycomb layouts. The study considers 19 flow angles from 0° to 90° with 5° interval under a uniform current of 0.25 m/s. The distance between the two cages is 2D. Each flow angle is subjected to a time-dependent simulation lasting 2 000 seconds.

Conventional fish farms, according to Halwart *et al.* (2007), are normally placed in sheltered areas, as specified by Norwegian Standards (Standards Norway, 2009), with a significant wave height of 0-0.5 m and a peak wave period of 0-2 s. Shen *et al.* (2018) discovered that when the current velocity is 0.5 m/s, waves at these locations contribute only up to 10% of the tension forces in mooring lines. Because the focus of this research is on the structural reactions and flow fields of typical fish farms under operational settings, wave-induced forces are regarded as minor in comparison to current-induced forces. As a result, wave loads are not considered in the present numerical simulations.

Table 5- 1: Dimensions and properties of the fish cage in the present study.

Component	Parameter	Value	Unit
Floating collar	Material	HDPE	
	Inside pipe diameter	50	m
	Outside pipe diameter	53	m
	Pipe cross section radius	0.18	m
	Pipe thickness	0.004	m
	Young's modulus	270	GPa
	Poisson ratio	0.29	--
	Density	910	kg/m^3
Netting	Material	PA (Nylon)	
	Vertical cylinder depth	15	m
	Conical bottom depth	28	m
	Net bag diameter	50	m
	Twine diameter	2.5	mm
	Mesh length	20	mm
	Net bag weight	0.5	kg/m^2
	Young's modulus	2	GPa
	Poisson ratio	0.3	--
	Density	1140	kg/m^3
	Solidity	0.25	--
Sinker Tube	Material	Steel	
	Inside pipe diameter	50	m
	Outside pipe diameter	51	m
	Pipe cross section radius	0.125	m
	Pipe thickness	0.013	m
	Young's modulus	204	GPa
	Poisson ratio	0.29	--
	Density	7874	kg/m^3
	Centre points weight	100	kg
Mooring line	Material	PE	
	Initial length of anchor line	360	m
	Initial length of frame line (Array/Honeycomb)	100 / 57.73	m
	Numerical Section diameter	0.05	m
	Young's modulus	270	GPa
	Poisson ratio	0.2	--
	Density	960	kg/m^3
Buoy	Diameter	2	m
	Vertical cylinder depth	1	m
	Conical bottom depth	2	m
	Buoy line	7.5	m

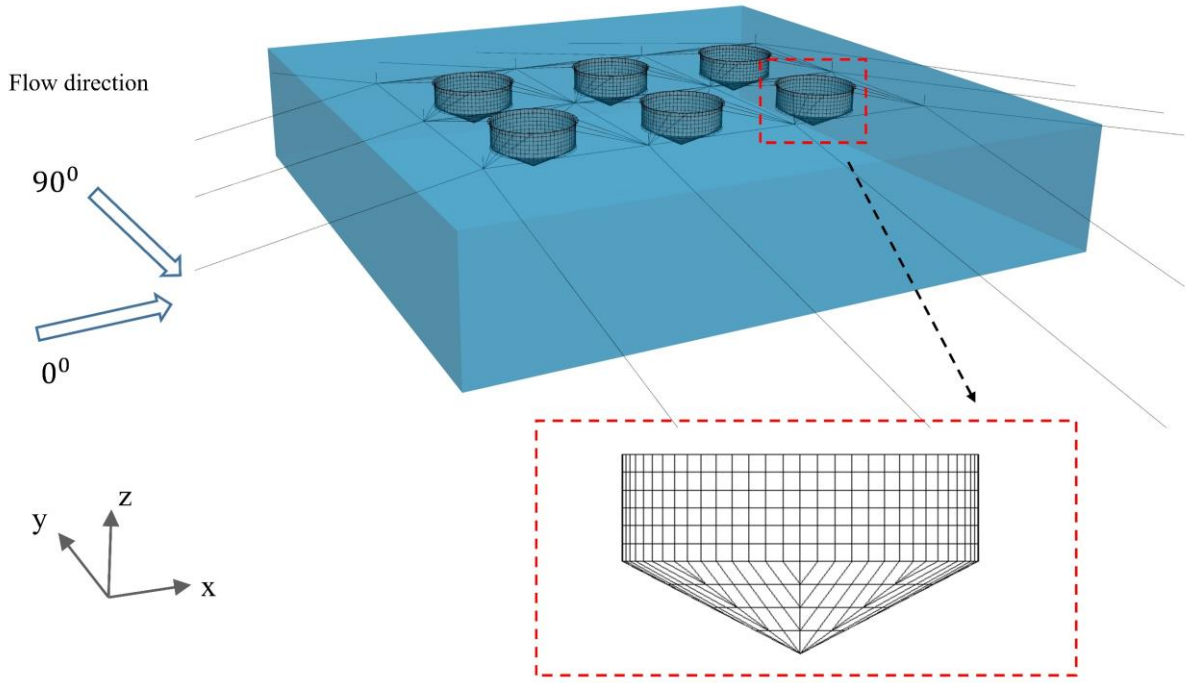

Figure 5- 1: Computational domain and the layout of 2x3 Array farm.

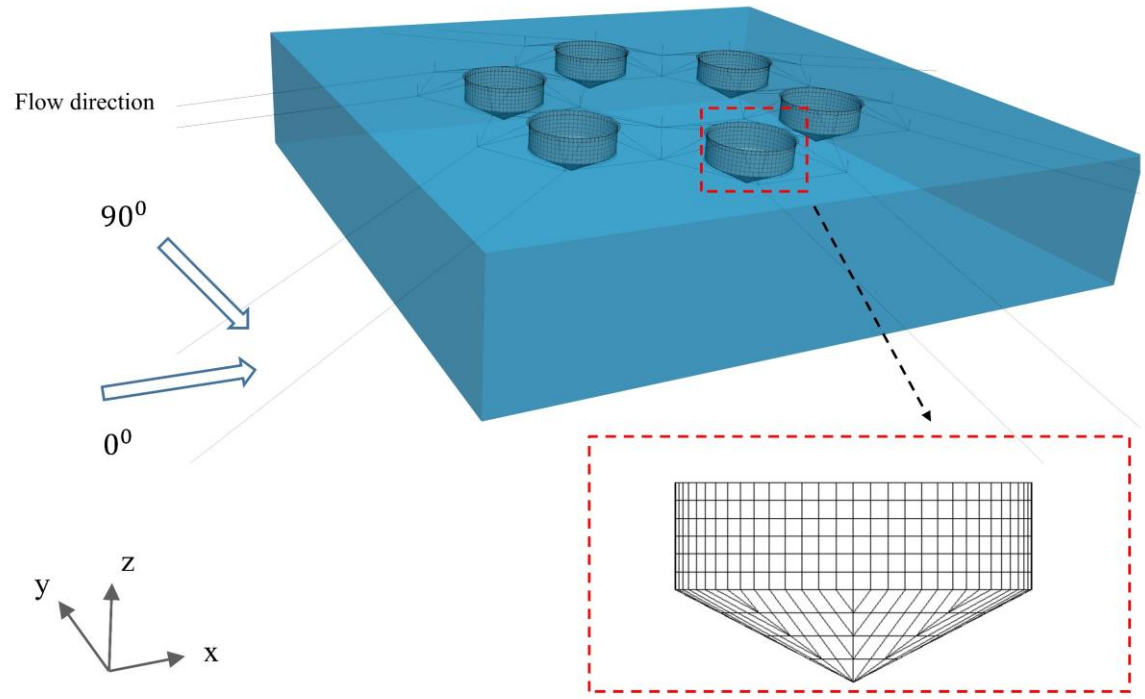

Figure 5- 2: Computational domain and the layout of Honeycomb farm.

5.1.2. Mooring system configuration

Figures 5-3 and 5-4 provide overviews of the 2 × 3 Array and Honeycomb fish farm layouts, respectively. The mooring lines in both layouts are labeled in a clockwise direction, starting from the upper right side. The anchor lines are represented by black lines, the bridle lines are represented by red lines, and the frame lines are represented by green lines. The blue arrows located at the center of each fish farm layout represent the global coordinate system, with the X and Y axes indicated. The Z-axis is oriented upward from the paper. The cages within the layouts are numbered sequentially from 1 to 6 along the positive X-axis.

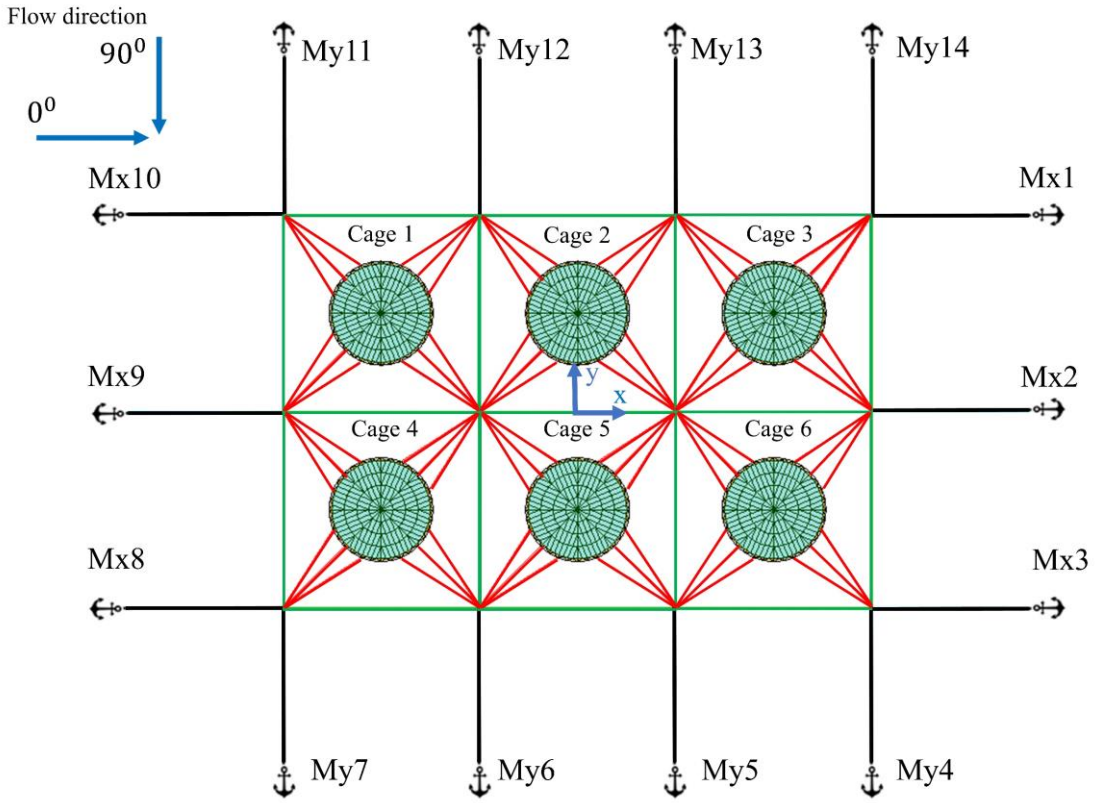

Figure 5- 3: Configuration of 2 × 3 Array fish farm.

Figure 5-3 illustrates the 2 × 3 Array fish farm with mooring lines along the X-axis labeled as "Mx" and the lines along the Y-axis labeled as "My." The layout includes a total of 14 anchor lines.

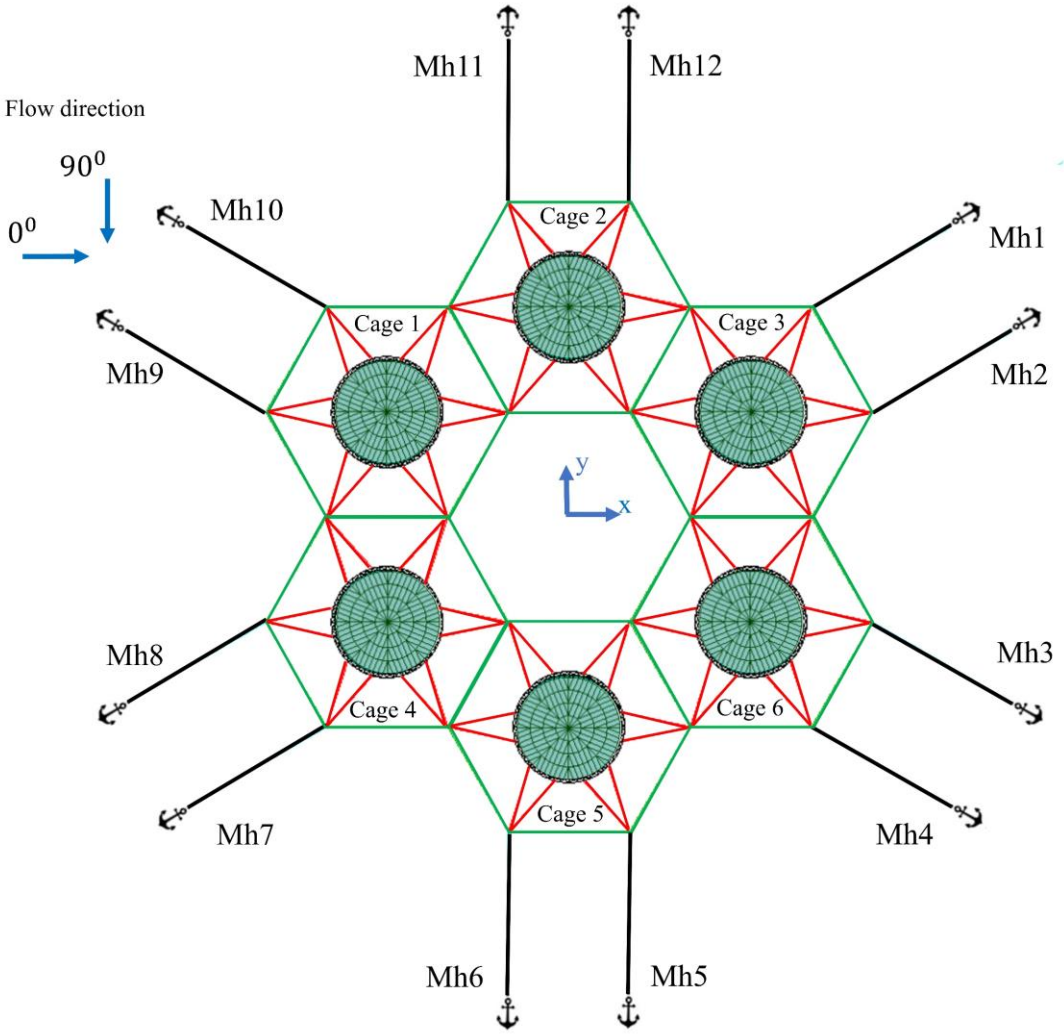

Figure 5- 4: Configuration of the Honeycomb fish farm layouts.

In Figure 5-4, the Honeycomb fish farm layout is presented, showing the specific mooring lines denoted as "Mh." This layout is comprised of a total of 12 anchor lines.

5.2. Results and discussion

5.2.1. 2 × 3 Array farm

5.2.1.1 Flow field

The direction of the incoming flow has a large influence on the flow fields inside and surrounding a fish farm, which are characterized by non-dimensional velocity in this study. The numerical simulation findings reveal that raising the angle of incidence of the incoming flow

leads to a greater number of positive wake regions or flank flow in the upstream of the fish farm, while decreasing the wake effect on the downstream cages. The presence of upstream cages is linked to the phenomena of flank flow, which corresponds to a rise in velocity and can be explained by the principle of mass conservation. Despite their high permeability, the fish nets operate as partial obstacles to the flow of water passing through the cages, causing the flow to divert around the cages and increasing velocity. The blockage effect is stronger in staggered (offset) net cages than in tandem (linear) net cages, resulting in a uniformly distributed wake downstream of the fish farm. When the flow angle reaches 90°, the flow pattern around the fish farm resembles that observed at 0°, as the net cages return to a tandem arrangement, as illustrated in Figure 5-5.

In the context of fish farming, the downstream cages are exposed to variable velocities as a function of the flow angle. As wake regions from different upstream cages combine in a specific flow angle, areas of decreased velocity from one cage may be compensated by flanks of wake regions from other upstream cages. As a result, all cages experience similar ambient flow velocities.

In terms of velocity reduction, the downstream velocity of the fish farm at 0° is expected to be higher than at 90° due to the existence of more tandem net cages in the flow angle, as shown in Figure 5-5.

0°

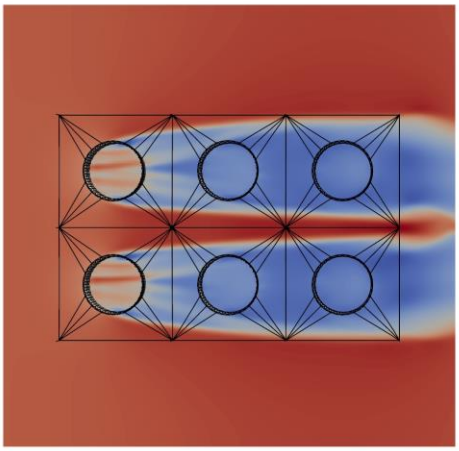

5°

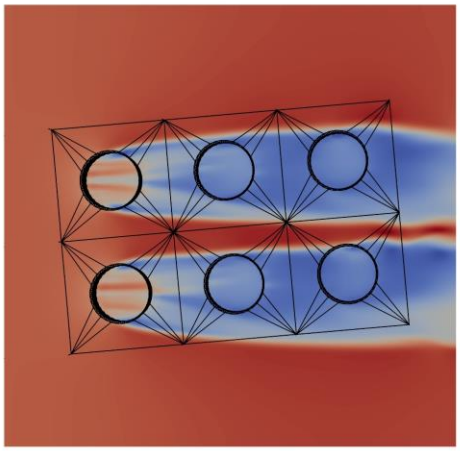

10°

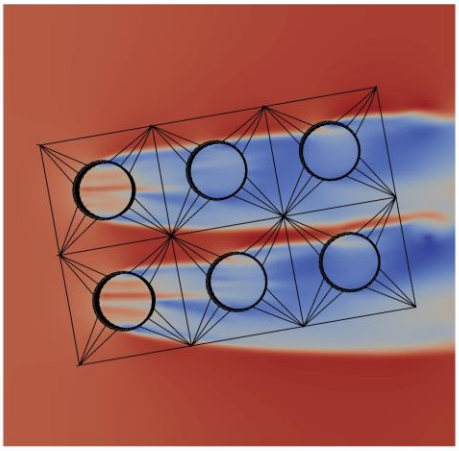

15°

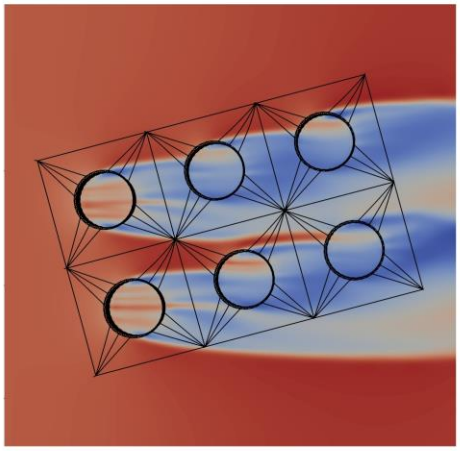

20°

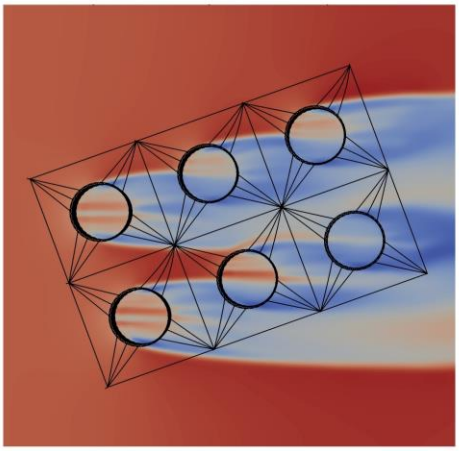

25°

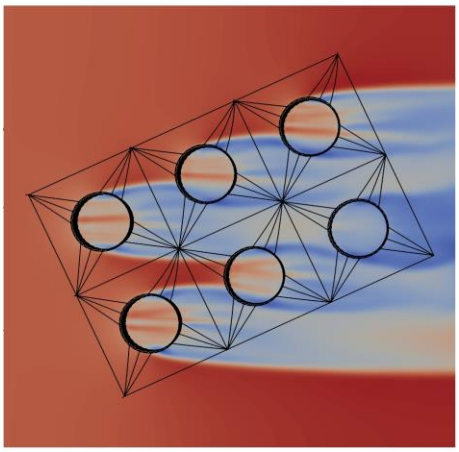

30°

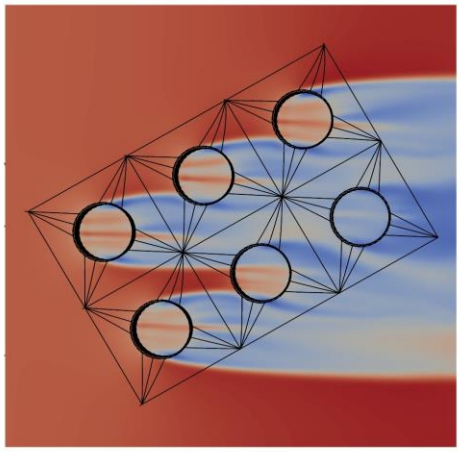

35°

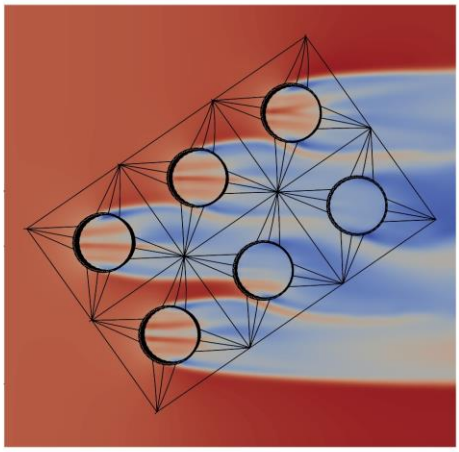

40°

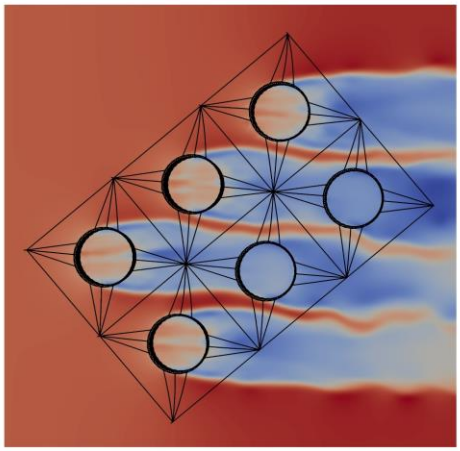

45°

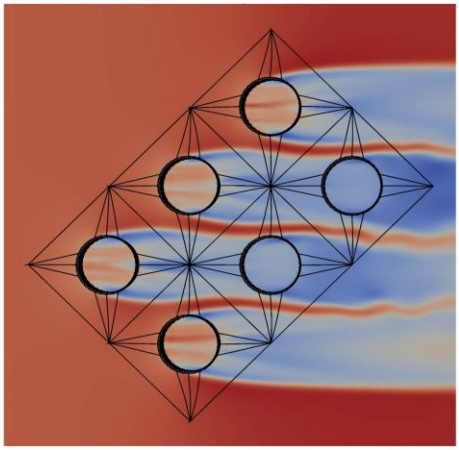

50°

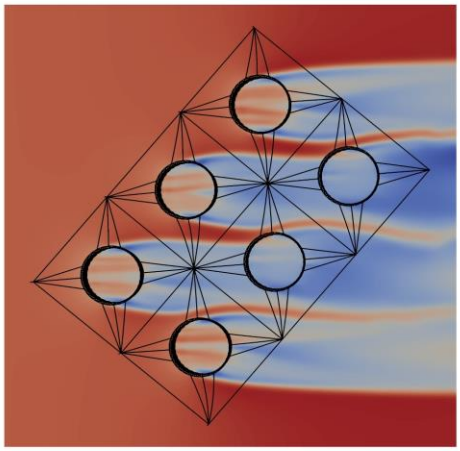

55°

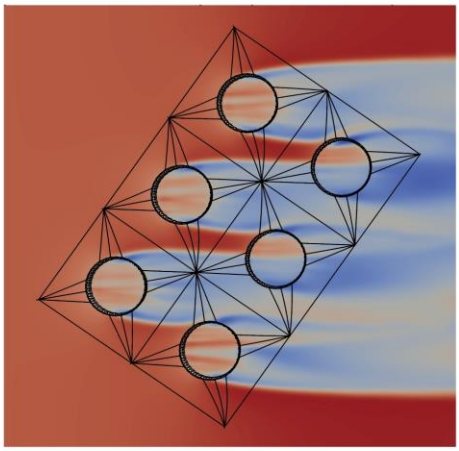

60°

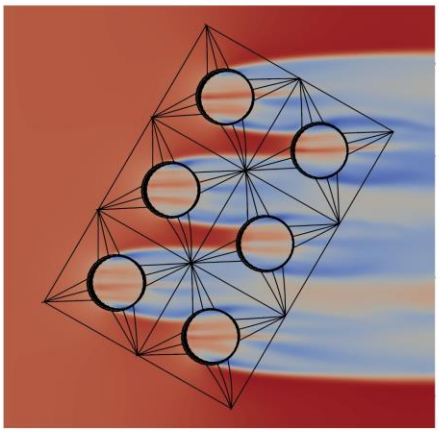

65°

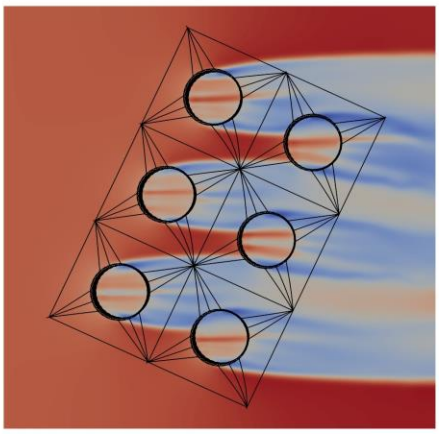

70°

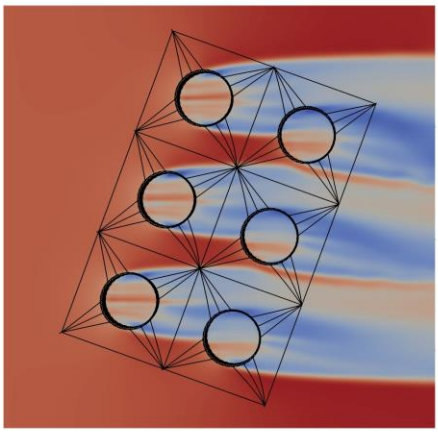

75°

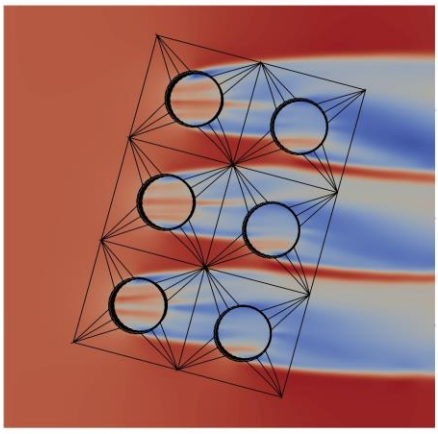

80°

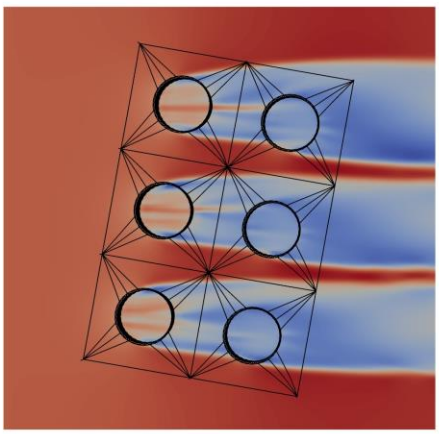

85°

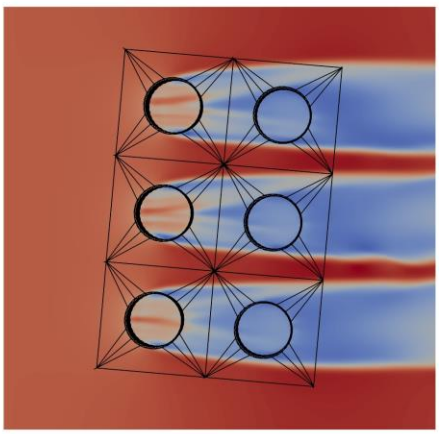

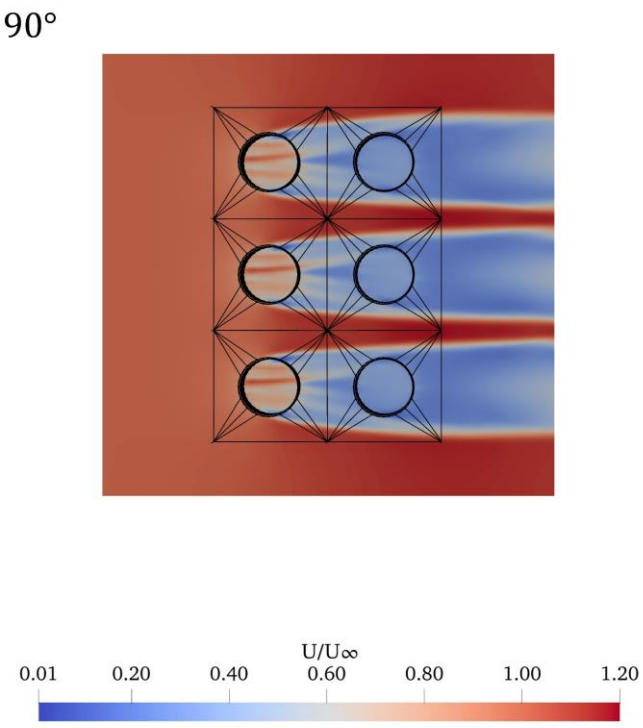

Figure 5- 5: Numerical results of flow fields within and around the fish farm with different flow angles on the horizontal plane Z=-7.5 m.

Monitoring flow velocity inside net cages is critical in examining the flow field inside fish farms because it provides insights into the cages' water exchange and overall flow environment. In this study, the non-dimensional flow velocity $U/U_{-\infty}$ inside the net cages was measured at the center, as shown in Figure 5-6. The non-dimensional flow velocity $U/U_{-\infty}$ inside the net cages ranged from 0.24 to 1.04 across nineteen flow angles, suggesting significant fluctuations in flow velocity throughout the fish farm.

The netting's blocking effect resulted in a substantial flow velocity reduction on downstream net cages. However, due to the interactions of wakes from different surrounding net cages, the downstream net cages do not always receive a velocity-reduced water flow. As shown in Figure 5-6, when the flow angle is 25°, the flow velocity inside Cage5 can be even slightly increased due to the flank flow from the upstream cages (Cage1 and Cage4).

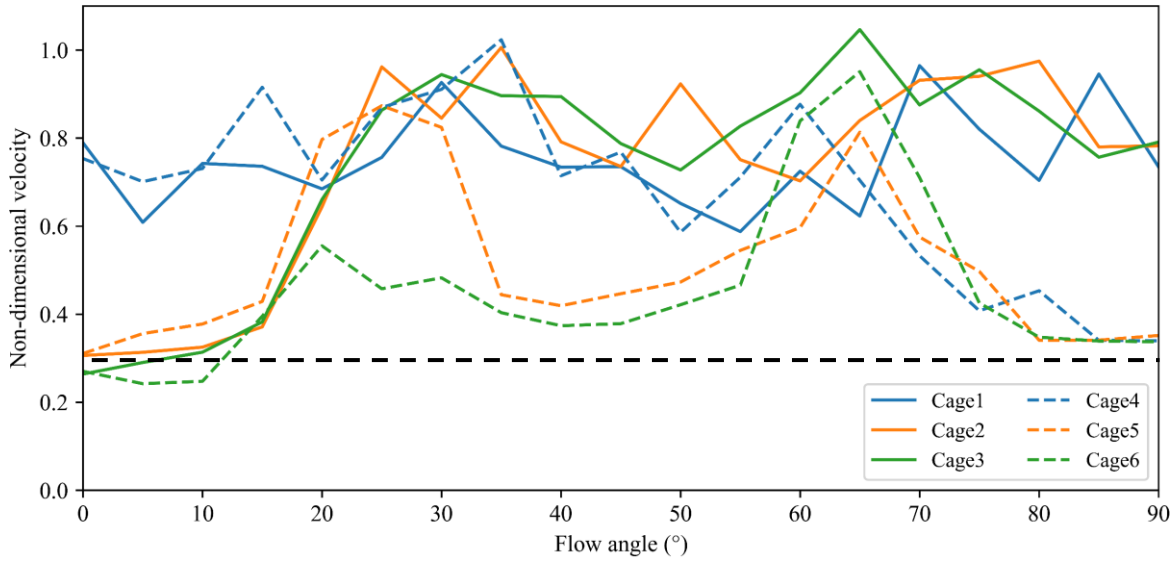

Figure 5- 6: The non-dimensional velocity at the center of cages under different current angles.

Further investigation revealed that at the flow angle of 65°, substantially higher flow velocities ranging from 0.62 to 1.04 were detected inside net cages. These high flow velocities will be helpful for water exchange within the cages. Furthermore, the flow velocity deviation among six cages was lowest at an incoming flow angle of 65°, indicating a stable flow environment throughout all cages. However, for an incoming flow angle of 5°, a relatively smaller velocity ranges from 0.24 to 0.7 was founded, indicating poor water exchange.

As shown in the Figure 5-5 when the flow angle = 0°, Cages 1 and 4 have undisturbed current velocity, while the remaining cages are shielded by Cages 1 and 4. Because of the farm's geometric layout, when the flow angle = 90°, Cages 1, 2, and 3 will have the same undisturbed current velocity. However, at both 0° and 90° flow angles, the number of tandem cages changes, resulting in downstream fish cages experiencing different current velocities with minor variations. Cages 2 and 5 have the same current velocity at 0° flow angle, whereas Cages 3 and 6 have the same velocity value due to axis symmetry and similar placement along the X-axis. Similarly, downstream fish Cages 4, 5, and 6 subject to the same flow velocity at 90° flow angle.

5.2.1.2 Total force on the fish farm and the nets

The total drag forces on the fish farm and net panels with respect to different flow angles are presented in Figure 5-7. The total drag force on the farm consists of the force on the mooring lines and the net panels.

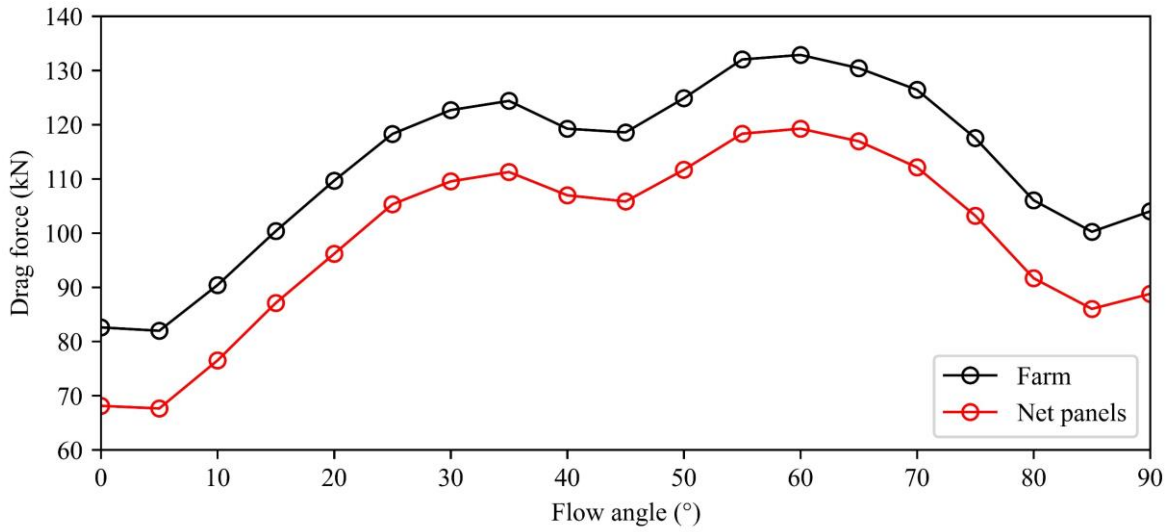

Figure 5- 7: The total drag force on the farm and the net panels.

The total drag force on the farm and net panels first increases with increasing the flow angle, but as the flow angle exceeds 35°, the farm experiences a decline in drag force until 45° flow angle. When the flow angle is 60°, the total drag force reaches its maximum and begins to reduce until it reaches 85°. The cage-to-cage wake effect can explain differences in total drag force with changing flow angles. The flow velocities encountered by fish cages fluctuate when the flow angle changes, and thus the total drag force changes.

The drag force on the farm reaches the maximum value when the flow angle of 60°. This can be explained by mass conservation. As shown in Figure 5-5, when the flow passing through the upstream fish cages, a part of the flow goes around the cages and gets an increased velocity at the flank of the cage. The velocity-increased flow will bring more loads on the net panels. The farm experiences the greatest drag force at this flow angle since the force in hydrodynamic force models is related to the square of the flow velocity (Lekang, 2019).

Cheng (2017) found that environmental loads on nets account for more than 85% of the total loads on a gravity-based fish cage. Consistent with his experimental findings, the total force on the farm consists of 82% to 90% of the force on the nets. Therefore, the drag force on the farm and net panels shows the same trend.

5.2.1.3 Cultivation volume

The effect of flow direction on the total cultivation volume of a 2 × 3 Array layout fish farm was analyzed and is presented in Figure 5-8. The cultivation volume was calculated using the divergence method, as described by Eq (5-1).

$$V = \iiint_{\Delta} (\nabla . f)\, d\forall = \oiint_{s} (f . n) dA_s \qquad (5\text{-}1)$$

It was observed that the total cultivation volume of the fish farm first decreases with the increasing flow angle until 55°, and then increases with the increasing flow angle. The fish farm experiences the highest cultivation volume at 0° flow angle due to the geometrical configuration of the fish farm, where the number of cages experiencing shielding (wake) effect varies.

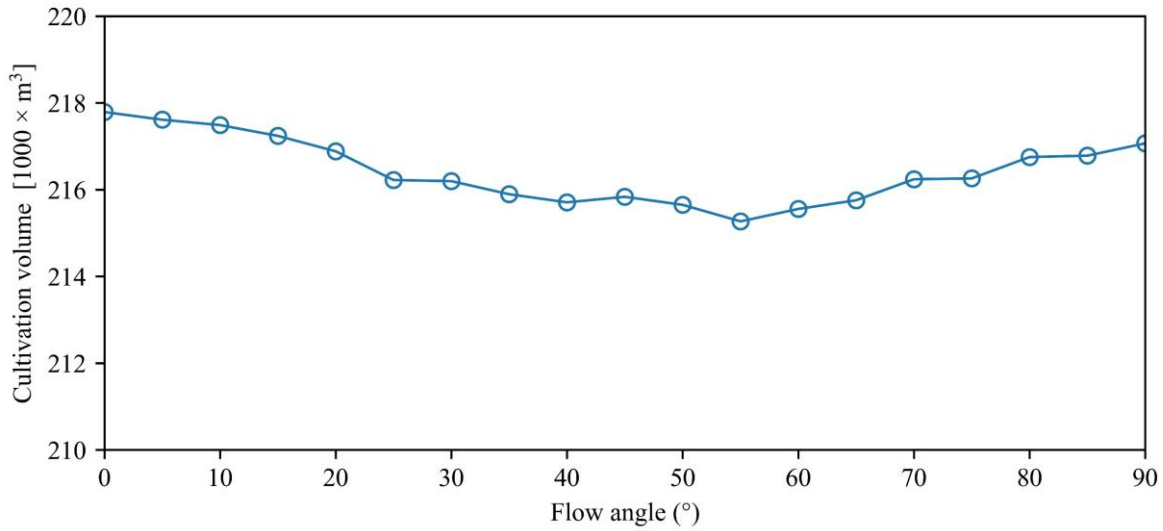

Figure 5- 8: Total cultivation volume change with flow angle.

The wake effect was discovered to contribute significantly to variations in cultivation volume. Individual fish cages experience various flow velocities and drag forces when the flow angle varies. Furthermore, the farm's overall cultivation volume is significantly associated with the total drag force on the nets, with a higher drag force corresponding to a lower cultivation volume. As shown in Figure 5-7, the change in cultivation volume with respect to flow angle follows the opposite trend as the drag force on the nets.

5.2.1.4 Tensions on the anchor lines under different flow angles

The tension distribution and extreme tension in anchor lines under different flow angles are presented in Figure 5-9. The tensions in all anchor lines between 0°and 90° flow angle are shown. In the 2 × 3 Array layout of the fish farm (Figure 5-3), the anchor lines with higher tension, namely Mx8, Mx9, and Mx10, are located on the negative side of the X-axis and are the primary contributors to hold the fish farms when flow angle is 0°. When the flow angle is 90°, the effective anchor lines to hold the fish farm are Mx11, Mx12, Mx13, and Mx14.

Furthermore, when the flow angle is either 0° or 90°, the response of each individual anchor line is connected with its symmetric counterparts. Anchor lines along the Y-axis, for example, are axis-symmetric with respect to the Y-axis and have the same tension in both the 0° and 90° flow angles, as seen in the Figure 5-9. Except for Mx9 and Mx2, which adjust for each other's reactions, this is true for anchor lines situated along the X-axis.

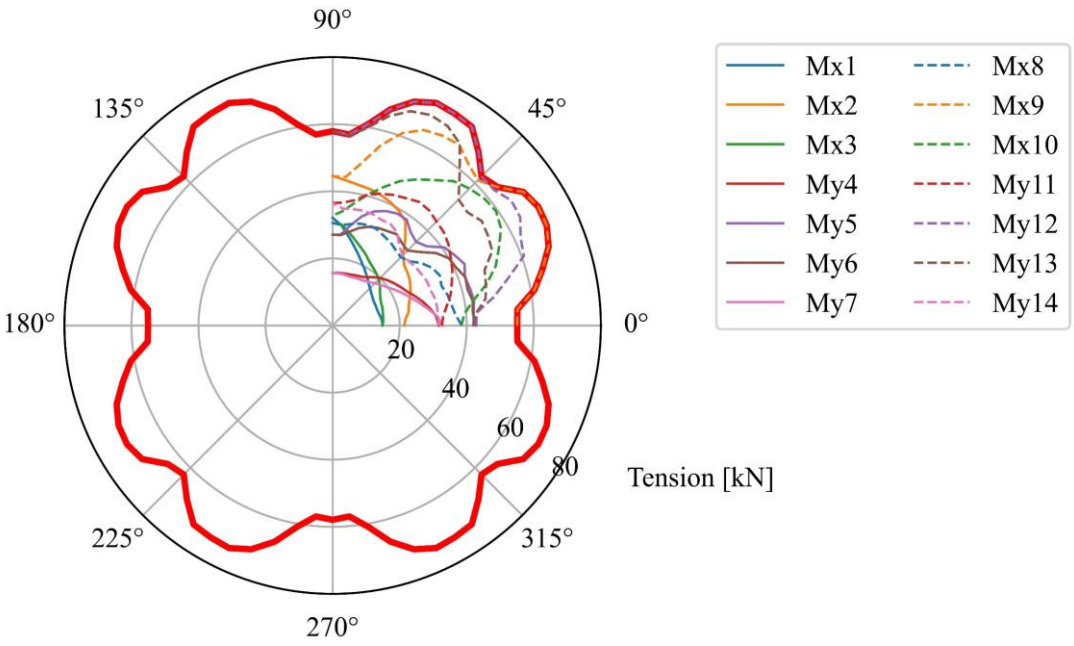

Figure 5- 9: The tension distribution and extreme tension in anchor lines under different flow angles

The highest tension among all of the 14 anchor lines in the mooring system, is defined as the extreme tension in anchor lines (ETAL). The value of ETAL is an important aspect in the design and operation of offshore fish farms. ETAL was investigated in this study for varied flow angles in a 2x3 Array layout of a fish farm. The sum of environmental loads was distributed to the anchors using the mooring system arrangement. The flow angles can affect the sum of environmental loads as well as ETAL.

As shown in Figure 5-9, the ETAL is indicated by the red line. The maximum value of ETAL 73.19 kN when the flow angle is 60°-65°, and this maximum value is located in anchor line My12. Similarly, the ETAL reaches 70.80 kN at flow angles of 25°-30° on anchor line Mx9. These findings indicate that the maximum ETAL and maximum drag force on the farm might happen at different flow angles. In Section 5.2.1.2, the maximum drag force on the farm happens when the flow angle is 60°. However, the maximum ETAL can occur at a different flow angle, indicating that the number of anchor lines contributing to holding the current load varies with flow angle. As a result, ETAL can change significantly as the flow angle changes, even when the total drag force on the farm remains constant.

The geometric symmetry of the fish farm also results in similar observations of the ETAL for other flow angles between 90° and 360°, with the dominant anchor line changing accordingly. Overall, these findings demonstrate the importance of analyzing ETAL for different flow angles and the impact of mooring system configuration on the distribution of environmental loads to the anchors.

5.2.2 Honeycomb farm

5.2.2.1 Flow field

The flow field inside and around a fish farm, as indicated by dimensionless velocity, are influenced by the direction of the incoming flow. The layout of the fish farm, as shown in Figure 5-10, leads to a periodic flow field pattern. This means that the flow field around and inside the fish farm repeats itself every 60°, reflecting the farm's layout design. Through numerical simulations, it has been observed that increasing the flow angle initially results in a decrease in the number of flanks in the upstream area of the fish farm. However, the downstream cages experience an increase in the wake effect until the flow direction reaches 30°.

When the flow direction decreases between 30° and 60°, the flow field exhibits a diverse trend. Subsequently, when the flow direction reaches 60° and increases through 90°, the fish farm experiences a reduction in the number of positive wake regions or flanks in the upstream area, while the wake effect on the downstream cages increases. This is due to the presence of fish cages, which block the water flow and lead a part of the flow passing around them, consequently, enhance the velocity in the flank. When the flow angle is 0°, the flank flow between Cage1 and Cage4 merged into one velocity-increased stream, and this stream flows through the middle of the fish farm. When the flow angle is 30°, two velocity-increased streams exist at the two sides of Cage1. These two streams also come from the merging of flank flows, which are at the side of Cage1, Cage 2 and Cage4.

As shown in Figure 5-10, the blockage effect is more significant at flow directions of 0° compared to 30°. This is because more cages experience undisturbed velocity at 0° flow directions (Cages 1, 2, 4 and 5) compared to 30° flow angle (Cages 1, 2 and 4). More cage in front of the undisturbed flow means more flow will be blocked by the cages. Regarding the reduction in velocity, only two fish cages (Cages 3 and 6) are located in the wake flow when the flow angle is 0°, while three fish cages (Cages 3, 5 and 6) are located in the wake flow when the flow angle is 30°. Because of periodic characteristics, the flow field pattern repeats every 60°, the above-mentioned comparison also applies to 60° and 90°.

0°

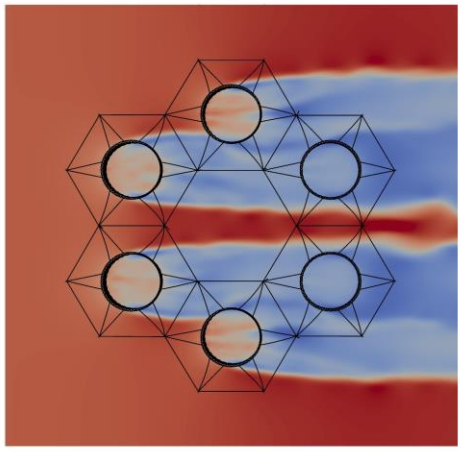

5°

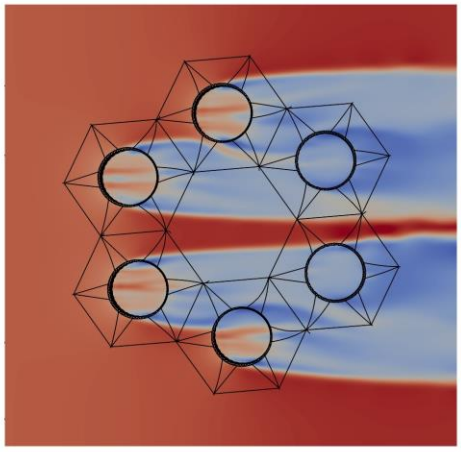

10°

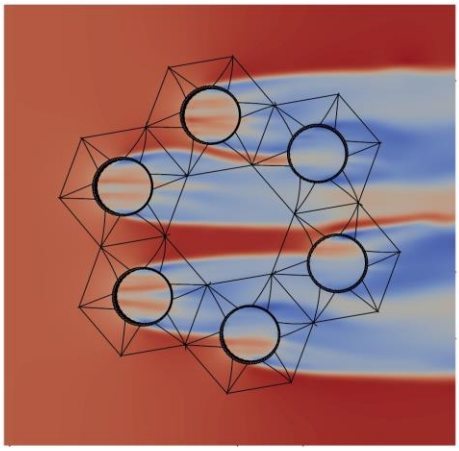

15°

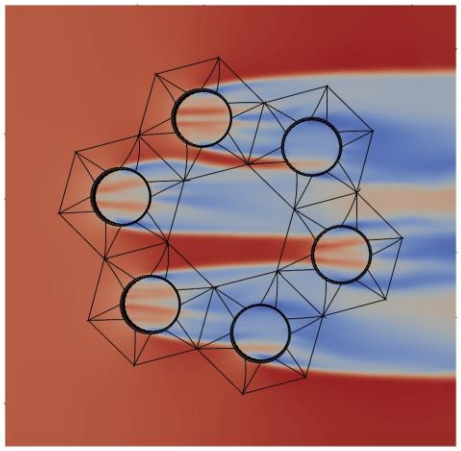

20°

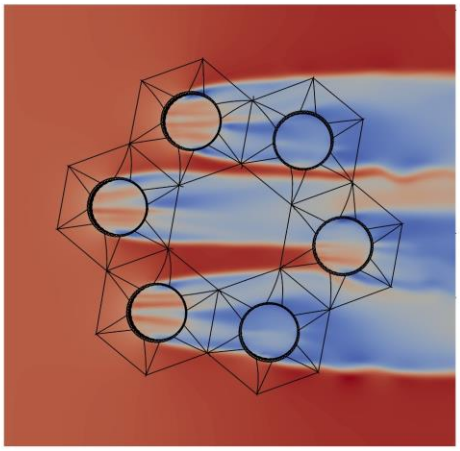

25°

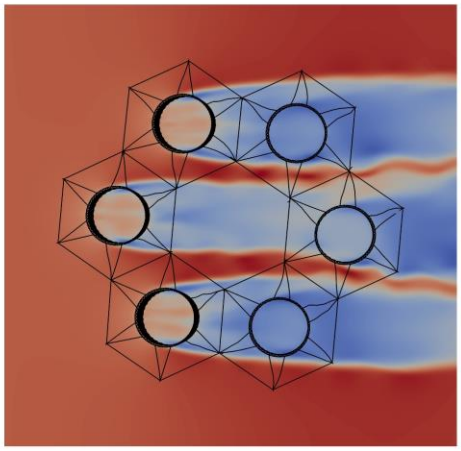

30°

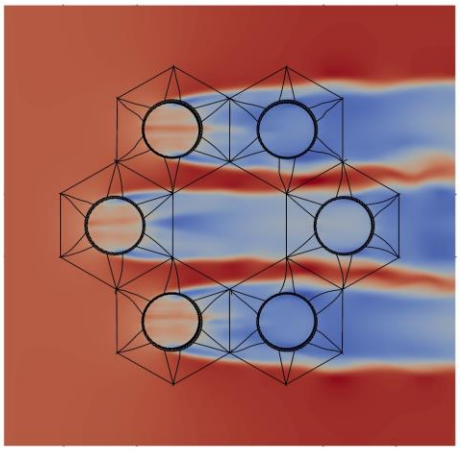

35°

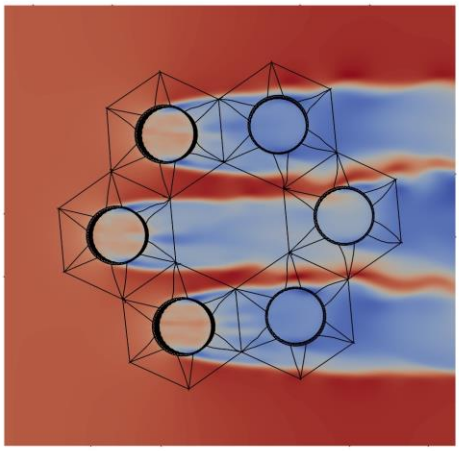

40°

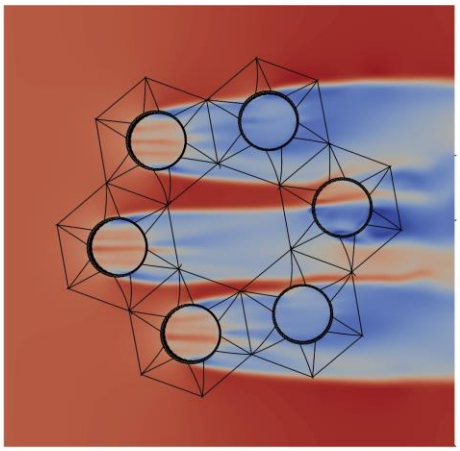

45°

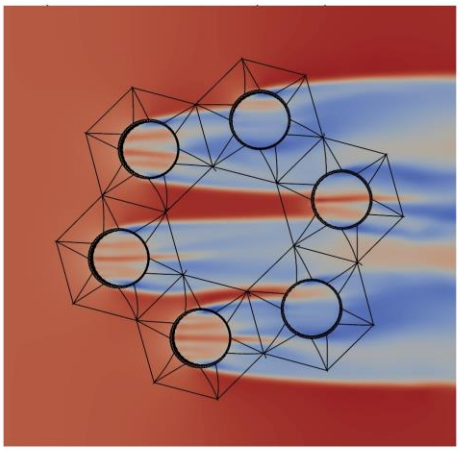

50°

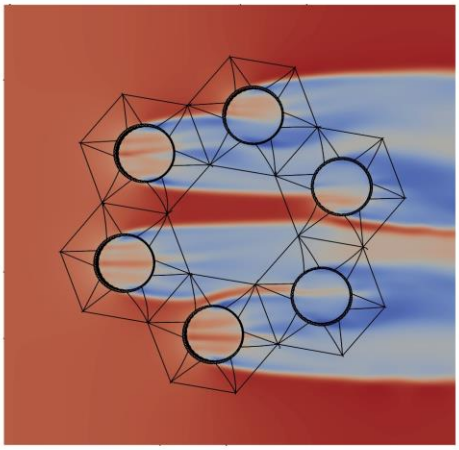

55°

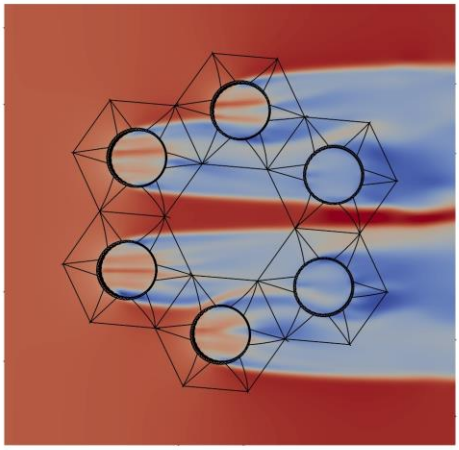

60°

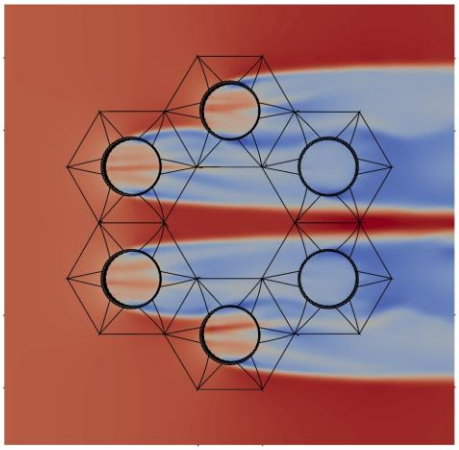

65°

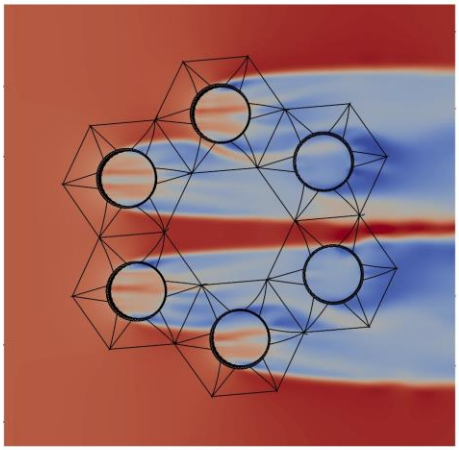

70°

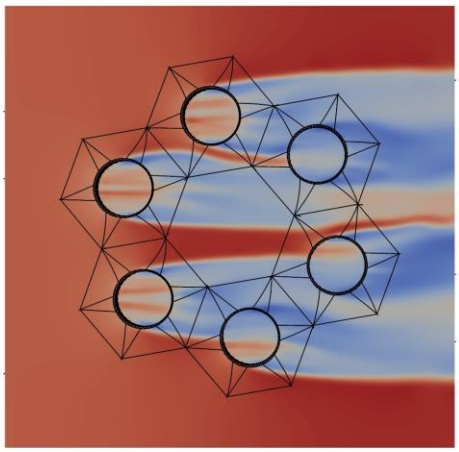

75°

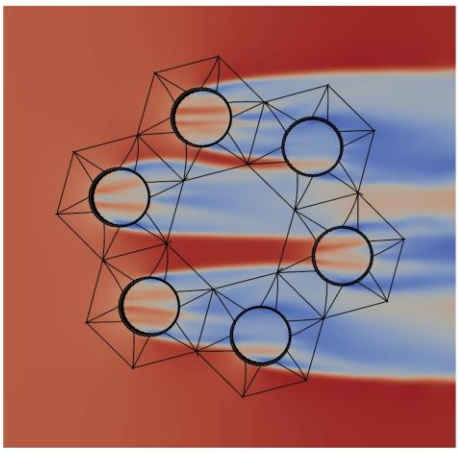

80°

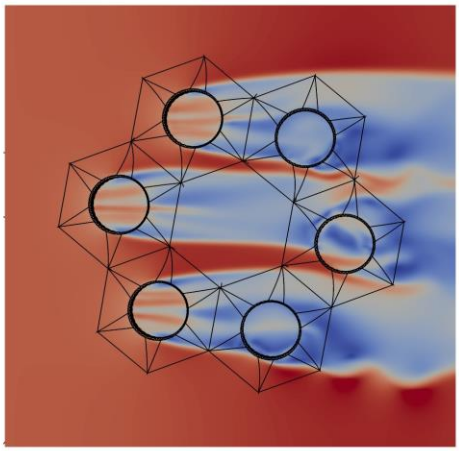

85°

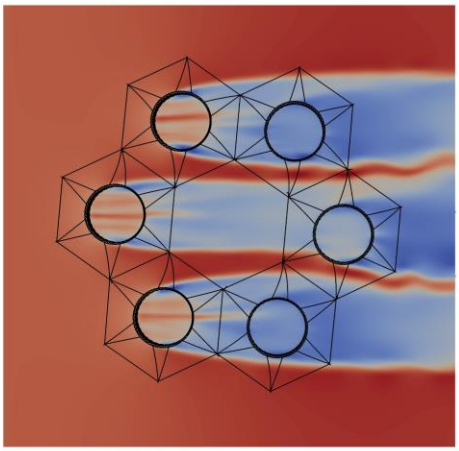

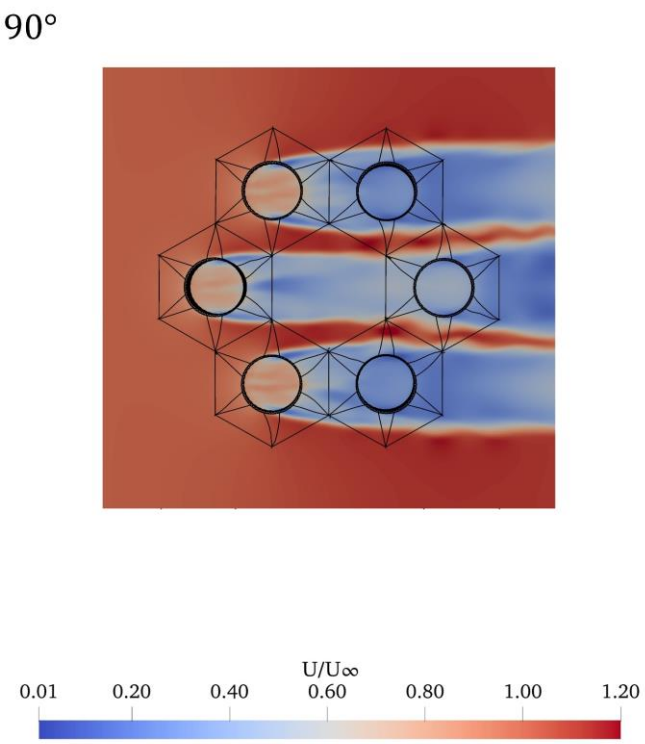

Figure 5- 10: Numerical results of flow fields within and around the fish farm with different flow angles on the horizontal plane Z=-7.5 m.

.

The non-dimensional flow velocity $U/U_{-\infty}$ inside net cages is measured to examine the flow field and water exchange ability within fish farms. This study reveals significant fluctuations in the non-dimensional flow velocity across nineteen incidence angles, ranging from 0.22 to 1.04. These findings indicate a non-uniform flow environment inside the net cages.

The presence of netting in the cages led to a significant decrease in flow velocity within most of the net cages, indicating the blocking effect of the netting. However, interestingly, certain downstream net cages exhibited no reduction or even a slight increase in flow velocity. This behavior can be attributed to the interactions and interplay of wakes generated by the surrounding net cages.

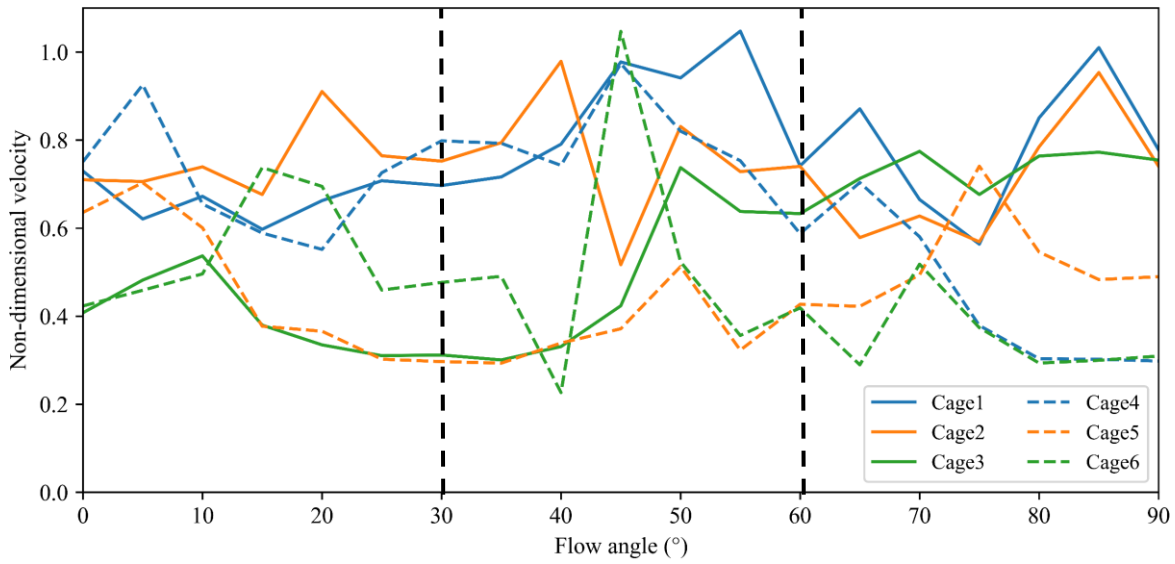

Figure 5- 11: The non-dimensional velocity at the center of cages under different current angles.

Figure 5-11 illustrates the non-dimensional velocity at the center of six cages under different flow angles. The same trend observed for the 0° and 60° flow angles is also applicable to the 30° and 90° flow angles within the fish farm due to the periodic geometric configuration. However, due to the change in flow direction, the number of cages experiencing fully wake flow is different. When the flow angle is 0°, Cages 1 and 4 experience an undisturbed current velocity, as they are not shielded by any other cages. On the other hand, the remaining cages (Cages 2, 3, 5, and 6) are shielded by Cages 1 and 4, resulting in a low current velocity. Cages 2 and 5, due to their placement and symmetry along the X-axis (see the first subfigure in Figure 5-10), have the same current velocity at a 0° flow angle. Similarly, Cages 3 and 6 also exhibit the same velocity value, as they benefit from axis symmetry and similar placement along the X-axis. At a 30° flow angle, Cages 1, 2, and 4 encounter undisturbed flow and nearly the same velocity. Cages 3 and 5, benefiting from axis symmetry and similar placement along the X-axis, experience the same velocity. However, Cage 6 faces flank flow from both sides, resulting in a higher velocity compared to Cages 3 and 5.

When the flow angle is 55°, the maximum value of flow velocities is measured, which is ranging from 0.32 to 1.04. This data implies that the net cages have a fast water exchange compared to the other flow angles. When the flow angle is 40°, the smallest flow velocities were measured, ranging from 0.22 to 0.97. This small velocity indicates a slow water exchange within the whole farm. Furthermore, the investigation finds that the deviation of flow velocity among the six cages is the lowest when the flow angles are 15° and 75°. This outcome suggests that at these flow angles, a stable flow environment was maintained throughout the whole farm.

5.2.2.2 Total force on the fish farm and the nets

The total drag force on the Honeycomb layout fish farm and net panels are illustrated in Figure 5-12. This figure shows the impact of wake effects on drag forces under different flow angles. The overall drag force comprises the forces experienced by additional components such as the frame line, bridles, floating collar, sinker tube, and mooring lines in addition to the forces experienced by the net panels.

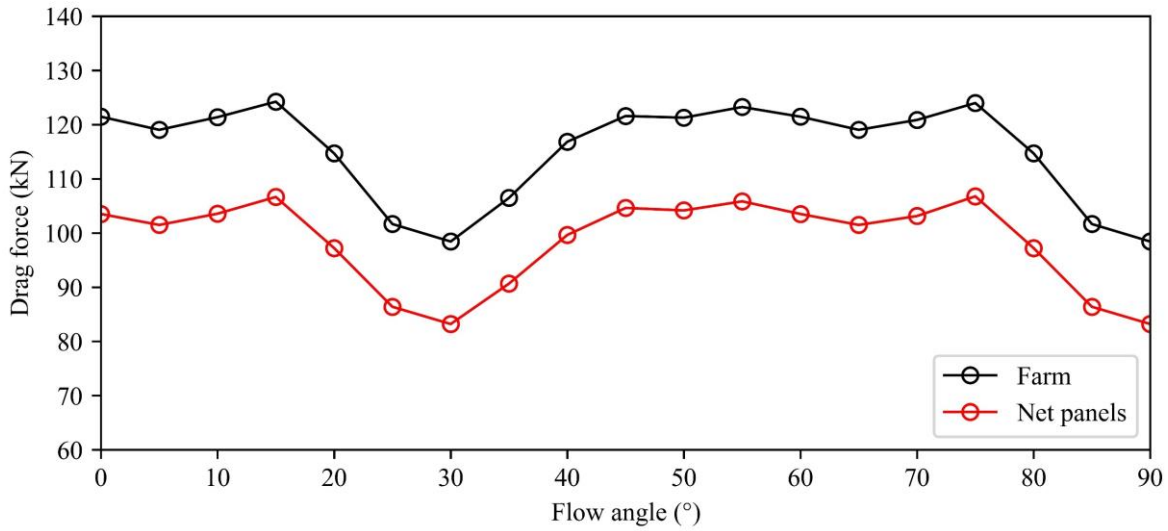

Figure 5- 12: The total drag force on the farm and the net panels.

When the flow angle between 0° and 15°, the total drag forces on the farm and net panels are roughly constant as the flow direction changes. However, the farm and net panels experience a decrease in drag force between flow angles of 15° and 30°. When the flow angle is 45°, the drag force on the farm and net panels reaches almost the same magnitude with the range 0° and 15°. As mentioned, section 5.2.2.1 the flow field in the Honeycomb design farm repeats itself every 60° flow angle. As a result, the magnitude of the drag force follows the same pattern for each 60° angle of the flow. This is shown in Figure 5-12, where the drag force on the farm and net panels follows a similar pattern in the 15°-30° and 75°-90° flow angles. This trend can be attributed to the number of cages within the farm that are subject to increased wake flow.

The flow angles of 15° and 75° correspond to the farm's greatest drag force. Surprisingly, except for the diminishing trend observed in the flow directions 15°-30° and 75°-90°, the total drag force remains reasonably stable across the other flow angles. The combined impacts of wake flow and flank flow experienced by some of the cages, as illustrated in Figure 5-10, can

be attributed to this small reduction in overall drag force. As a result, the farm's total drag force may maintain stability in these specific flow angles.

The net panels experience a significant proportion of the environmental loads. According to Figure 5-12, this proportion almost keep the same value of 85% in all flow angles. This indicates that irrespective of the flow angle, the net panels endure a consistent ratio of total force on the farm.

5.2.2.3 Cultivation volume

The effect of flow angle on the cultivation volume of a Honeycomb design fish farm is shown in Figure 5-13. Section 5.2.1.3 contains the approach for calculating cultivation volume.

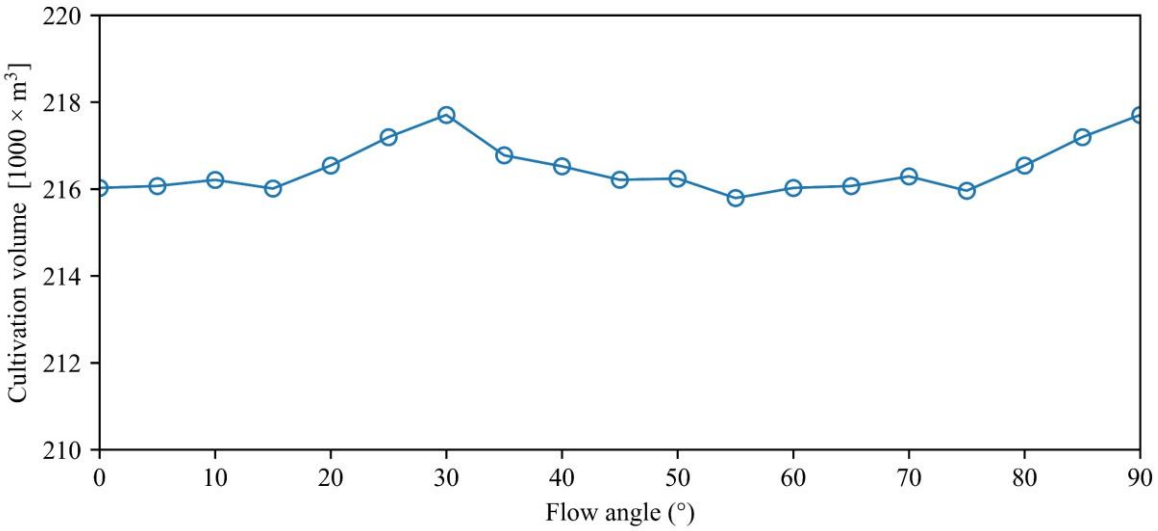

Figure 5- 13: Total cultivation volume change with flow angle.

Figure 5-13 shows that the overall cultivation volume varies only slightly across different flow angles, with the exception of 15°-30° and 75°-90°. The fish farm experiences the highest cultivation volume in flow angles of 30° and 90°. This can be explained with the correlation of the drag force and cultivation volume. The farm's total cultivation volume is significantly connected with the total drag force on the nets, with a higher drag force corresponding to a lower cultivation volume. Figure 5-12 indicates this relationship, in which the change in cultivation volume with regard to flow angle demonstrates an inverse trend as compared to the drag force on the nets. Additionally, the higher number of cages experiencing the wake effect in these flow angles 30° and 90° can be linked to the increase in cultivation volume.

Despite differences in flow velocities and drag forces encountered by individual fish cages as a result of varied flow angles, the farm's geometrical configuration compensates for the effect of wake with flank flow. As a result, the cultivation volume is able to recover and stabilize within the flow angle ranges of 0°-15° and 45°-75°.

5.2.2.4 Tensions on the anchor lines

The tension distribution and extreme tension in the anchor lines are shown in Figure 5-14 for different flow angles. It presents the tension of the anchor lines between 0° and 90° flow angles. The tension in the other anchor lines can be determined using symmetry.

The anchor lines that experience higher tension, specifically Mh7, Mh8, Mh9, and Mh10, are positioned on the negative side of the X-axis in the Honeycomb layout fish farm as shown in Figure 5-4. These anchor lines extend through a 30° angle on both the negative and positive sides of the Y-axis. They are critical in maintaining the stability of the fish farms at 0° flow angle. Mh11 and Mh12 are the anchor lines that effectively hold the fish farm in place when the flow angle is 90°. Similar tension distribution patterns can be seen with different anchor numbers for flow angles of 60° and 30°.

Additionally, in cases where the flow angle is either 0° or 90°, the response of each individual anchor line is linked to its symmetric counterparts. For instance, anchor lines Mh7, Mh8, Mh9, and Mh10 exhibit axis-symmetry with respect to the Y-axis and experience the highest tension in the 0° flow angles. Conversely, their symmetric counterparts, namely Mh1, Mh2, Mh3, and Mh4, have the lowest tension on them. This distribution of tension helps to balance and adjust the structural response of the Honeycomb fish farm, as demonstrated in Figure 5-14.

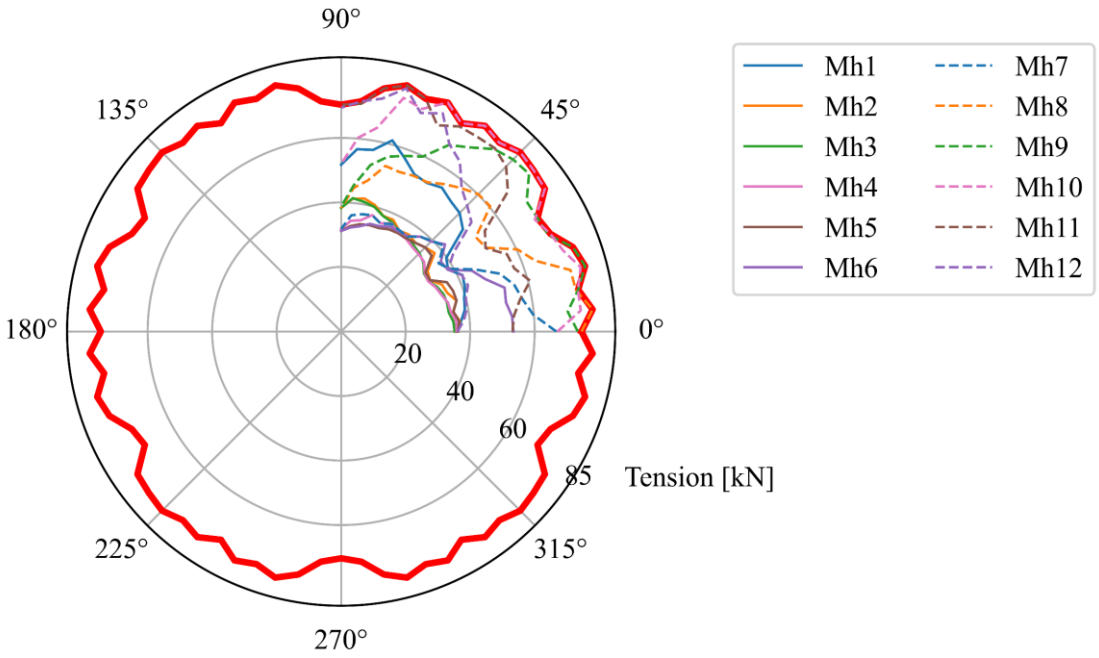

Figure 5- 14: The tension distribution and extreme tension in anchor lines under different flow angles

The extreme tension in anchor lines (ETAL), the maximum tension experienced in any of the mooring system's 12 anchor lines, is critical in the design and operation of offshore fish farms. This study focused on the ETAL in the setting of different flow angles within a Honeycomb layout fish farm. The sum of environmental loads was distributed to the anchors using the mooring system configuration and different flow angles.

The extreme tension in anchor lines (ETAL) can be observed by the red line in Figure5-14, which reaches its maximum at a flow angle of 75°. The maximum value of ETAL at this flow angle on anchor line My11 is 78.97 kN. Similarly, for all flow angles, the ETAL for anchor lines Mh7, Mh8, Mh9, and Mh10 ranges between 70.29 kN and 78.97 kN. These data suggest that the direction of the maximum drag force on the fish farm correlates to the maximum ETAL. Furthermore, there is little difference in the ETAL across different flow angles, which aligns with the farm's slight changes in drag force.

According to the section 5.2.2.2, the total drag force on the farm was greatest at flow angles of 15° and 75°. Similarly, the maximum value of extreme tension in anchor lines (ETAL) occur in the same flow angles. This means that regardless of flow angle, the number of anchor lines contributing to holding the current load remains constant. As a result, as long as the total drag force on the farm remains constant, the ETAL may exhibit slight fluctuations as the flow angle changes.

Because of the fish farm's geometric symmetry, identical observations of extreme tension in anchor lines (ETAL) are made for additional flow angles ranging from 90° to 360°. Depending on the flow angle, the precise anchor line that experiences the most tension may change. This highlights the importance of assessing the ETAL for different flow angles and the impact of mooring system design on the distribution of environmental loads among the anchor lines. These findings emphasize the need of considering diverse flow angles and optimizing the mooring system design to ensure the fish farm's stability and integrity.

5.2.3 Comparison of the 2 x 3 Array and Honeycomb layout

Several factors influence the flow patterns and velocity distribution in both the 2 × 3 Array and Honeycomb layouts of fish farms. Wake regions, fish cage blockage effects, and diverting flow all contribute to an increase in velocity, notably in the form of flank flow. Furthermore, the flow patterns inside these layouts are complicated, with complex and turbulent movements.

In terms of flow patterns, the 2 × 3 Array layout has a flow field that repeats every 90° flow angle, however, the Honeycomb layout has a flow field that repeats every 60°. This means that the flow pattern within and around the Honeycomb layout fluctuates more frequently than the 2 × 3 Array layout. This increase variety in flow patterns could enhance water velocity and turbulence within the Honeycomb layout.

However, the number of cages exposed to wake flow and undisturbed flow has a crucial impact on shaping the flow characteristics within the fish farm. The number of cages experiencing wake flow and undisturbed flow varies significantly in the Array configuration during the period of changing flow angles. In comparison, the Honeycomb design exhibits less variation in the number of cages under the influence of wake flow and undisturbed flow as shown in Figures 5-5 and 5-10. As a result, the Honeycomb form provides a more predictable flow pattern based on flow angle.

Overall, the Honeycomb layout's characteristics make it advantageous in terms of providing a more stable and consistent flow pattern, which can be beneficial for fish farm operations and structural stability.

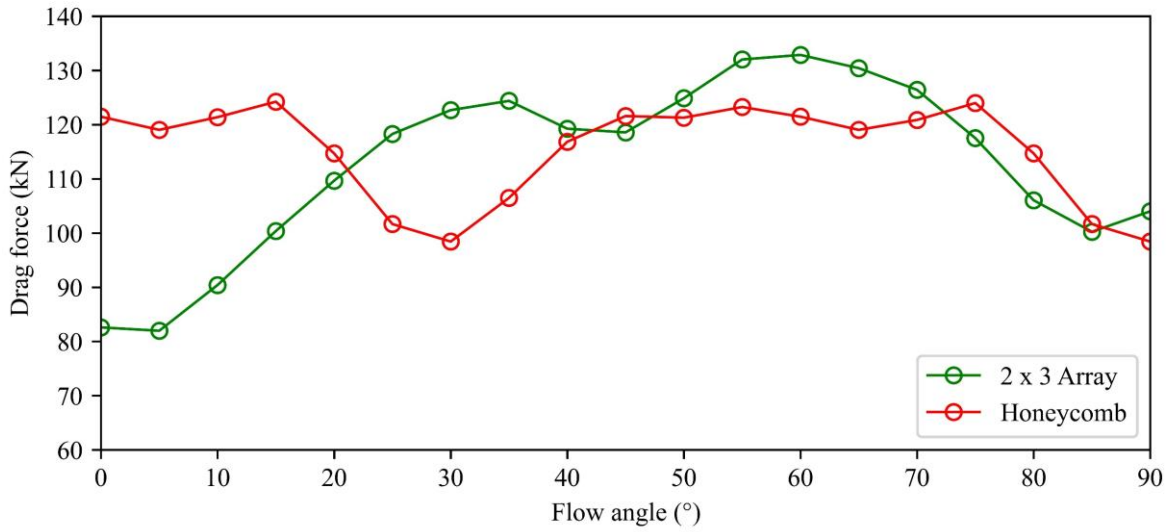

Figure 5- 15: The total drag force on the 2 x 3 Array and Honeycomb farm.

The total drag force on the fish farm is affected by flank flow as well as the number of cages exposed to wake flow and undisturbed flow.

As previously stated, sections 5.2.1.2 and 5.2.2.2, the drag force on the net panels contributes significantly to the overall drag force experienced by the farm. In the case of the Honeycomb layout, the net panels' contribution to drag force remains constant regardless of flow angle. However, the contribution of the net panels changes greatly depending on the flow angle for the 2 × 3 Array arrangement. The number of cages exposed to wake flow, undisturbed flow, and flank flow can explain this variance.

While the mean values of the total drag force are nearly same for both the 2 × 3 Array (112.76 kN) and Honeycomb (115.28 kN) layouts, there are considerable changes in the standard deviation (2 × 3 Array =15.52 kN, Honeycomb = 8.84 kN) of the drag force with regard to the flow angle. The drag force on the 2 × 3 Array layout changes significantly across different flow angles, however, the drag force on the Honeycomb layout changes slightly with the exception of 15°-30° and 75°-90° flow angles range as shown in Figure 5-15.

This implies that the Honeycomb layout has stronger predictability of the drag force due to the steadier contribution of the net panels, but the 2 × 3 Array pattern has higher variability in the drag force due to changing cage exposure to different flow conditions.

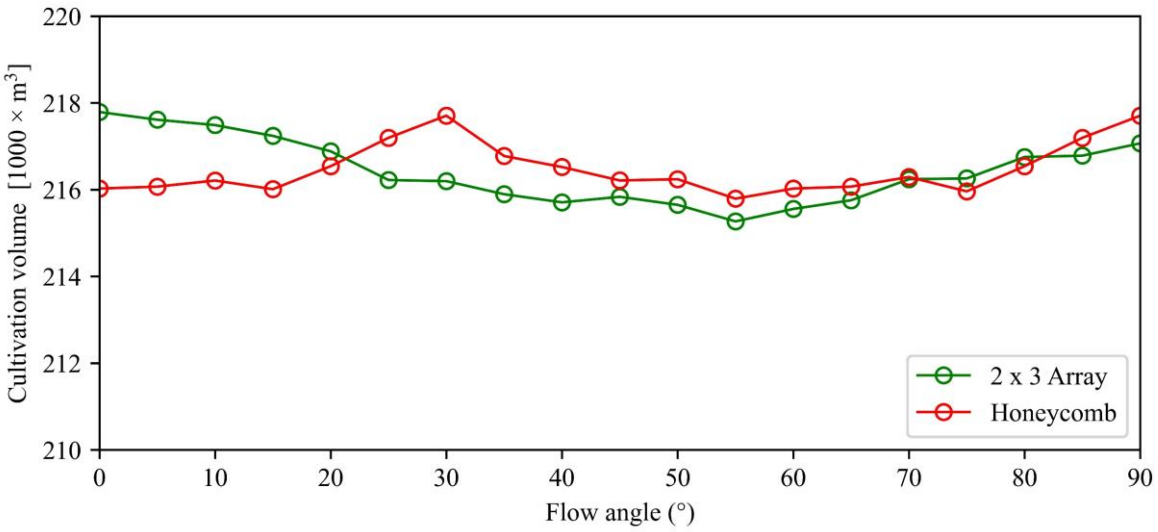

Figure 5- 16: Total cultivation volume change of the 2 x 3 Array and Honeycomb farm.

The cultivation volume within the cages is critical in determining the overall effectiveness of open cage sea-based fish farming. It refers to the amount of room available for fish to grow and move freely, and it has a direct impact on productivity, fish health, and environmental implications. The mean cultivation volume for both the 2 × 3 Array (216430 m^3) and Honeycomb (216470 m^3) layouts is similar as well. However, the Honeycomb design stands out with a lower standard deviation of cultivation volume (2 × 3 Array = 730 m^3, Honeycomb = 560 m^3), indicating a more consistent and steadier environment for fish. Furthermore, as illustrated in Figure 5-16, the Honeycomb layout generally provides a higher cultivation volume in most flow angles, giving fish more area to grow. This expanded capacity allows for a higher stocking density, which may result in enhanced fish productivity within the cages. In conclusion, while both layouts can contribute to fish productivity, the Honeycomb layout, with its smaller standard deviation and bigger cultivation volume, offers advantages in open cage sea-based fish farming for maintaining a stable environment and maximizing fish growth potential.

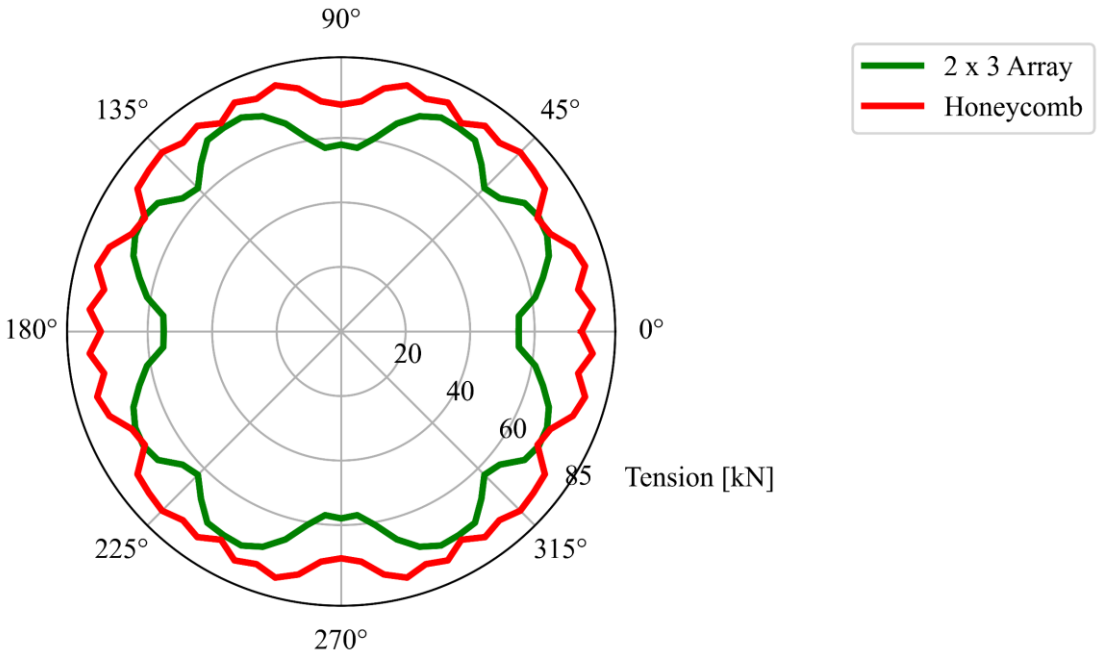

Figure 5- 17: The extreme tension in anchor lines of the 2 x 3 Array and Honeycomb farm.

In Figure 5-17, the extreme tension in anchor lines (ETAL) is indicated by the red line for the Honeycomb layout and the green line for the 2 × 3 Array layout. The ETAL values fluctuate more for the 2 × 3 Array layout compared to the Honeycomb layout due to varying drag forces on the fish farm with different flow angles. Therefore, the Honeycomb layout demonstrates a more predictable and steady distribution of extreme tension among the anchor lines, while the 2 × 3 Array layout experiences greater fluctuations. While the 2 × 3 Array layout experiences smaller or equal magnitude of the extreme tension in some flow angles, the Honeycomb layout utilizes 12 anchor lines to carry the environmental loads, whereas the 2 × 3 Array layout utilizes 14 anchor lines.

Overall, despite potential variations in the magnitude of extreme tension, the Honeycomb layout efficiently carries the environmental loads with fewer anchor lines, contributing to its structural stability and integrity.

In general, when comparing the two layouts, the Honeycomb layout has several advantages. For starters, its smaller covered area in the sea and lower exposure to environmental loads result in fewer mooring lines. This not only saves costs but also simplifies the installation and maintenance process.

Furthermore, the Honeycomb layout's geometric design also enables the control barge to be placed directly in the middle of the farm. This centralized location reduces the length and complexity of piping required for feeding and cleaning death fish tasks, resulting in material and installation cost savings.

In addition to the cost benefits, the reduced piping requirements in the Honeycomb layout also contribute to energy efficiency. With less piping, the need for electrical pumps is minimized, leading to lower energy consumption. This aligns with the goals of sustainability and environmental friendliness, making the Honeycomb layout an attractive option for those seeking more eco-friendly fish farming solutions.

Overall, the Honeycomb structure offers a cost-effective and efficient approach to fish farming, thanks to its compact design, reduced environmental impact, and optimized use of resources. These advantages make it a desirable choice for fish farm operators looking to optimize their operations while minimizing costs.

5.3 Summary

This study investigated the fluid structure interaction of two different fish farm layouts: the 2x3 Array layout and the Honeycomb layout. The research focused on flow field features, anchor line tensions, drag forces, and cultivation volumes. The main conclusions are as follows:

(1) The flow field inside and around the 2 × 3 Array layout farm repeats every 90° flow angle, while the flow field inside and around the Honeycomb layout farm repeats every 60° flow angle.

(2) At 65° flow angle, the 2 × 3 Array layout had higher flow velocities (0.62 to 1.04) inside the net cages, providing water exchange. At 5° flow angle, velocities ranged from 0.24 to 0.7, indicating poor water exchange. For the Honeycomb layout, flow velocities of 0.32 to 1.04 were observed at 55°, promoting water exchange. At 40°, velocities ranged from 0.22 to 0.97, indicating poor water exchange.

(3) The Honeycomb layout fish farm experiences the lowest flow velocity deviation among the six cages at flow angles of 15° and 75°. In contrast, the 2 × 3 Array layout shows the lowest velocity deviation among the six cages at a flow angle of 65°, indicating a consistent flow environment across the whole farm.

(4) In the 2 × 3 Array layout, the maximum drag force occurs at a flow angle of 60° and the net panels contribution vary between 82% and 90% of the total drag force with different flow angle. In the Honeycomb layout, the highest drag force is observed at flow angles of 15° and 75°. Overall, the drag force remains relatively stable across most flow angles, except for a diminishing trend between 15°-30° and 75°-90°. The drag force on the net panels contributes almost 85% of the total drag force on Honeycomb layout in all flow angles.

(5) The 2 × 3 Array layout achieves its minimum cultivation volume at a flow angle of 55°, while the Honeycomb layout experiences the lowest volume at flow angles of 15° and 75°. Except for the range of 0° to 15°, the cultivation volume of the Honeycomb layout is equal to or greater than that of the 2 × 3 Array layout.

(6) For the Honeycomb layout, the maximum ETAL value of 78.97 kN occurs at a flow angle of 75°, while the 2 × 3 Array layout reaches a peak of 73.19 kN at flow angles of 60°-65°. Honeycomb uses 12 anchor lines, while 2 × 3 Array requires 14.

Honeycomb shows a more predictable and stable tension distribution with fewer anchor lines.

(7) The Honeycomb layout offers a smaller covered area in the sea and lower exposure to environmental loads, making it a cost-effective and efficient approach to fish farming. Its compact design reduced environmental impact, and optimized use of resources contribute to its advantages in terms of structural stability and operational effectiveness.

Chapter 6

Conclusions and future work

In this thesis, numerical simulations using OpenFOAM and Code_Aster software are conducted to estimate the load on fish cages and the overall fish farm structure. Accurate load estimation is crucial for creating an optimal environment for fish growth in open sea conditions.

The first study in Chapter 4 focuses on investigating the influence of wake effects on downstream fish cages using a two-cage model. The flow field behind a permeable net structure and the estimated drag force on the downstream fish cage are analyzed. Different cage placements and solidities are examined, revealing that downstream fish cages can experience higher drag forces than upstream cages, when positioned between $\alpha = 30°$ and $\alpha = 70°$. Additionally, higher solidity levels can result in larger drag forces on the fish cage. These findings have important implications for optimizing fish farming systems to account for wake effects and minimize drag forces on the cages.

In Chapter 5, the second study introduces a coupling algorithm that combined OpenFOAM and Code_Aster to study fluid-structure interaction in fish farms. The focus is on evaluating the performance of fish farms with a 2×3 Array farm and a new Honeycomb farm design. The analysis considers various flow directions under pure current conditions, examining factors such as flow field characteristics, anchor line tensions, drag forces, and cultivation volumes. By comparing and analyzing these factors, valuable insights are gained regarding the efficiency and effectiveness of different fish farm designs.

The results of the numerical simulations emphasized the advantages of the Honeycomb layout. This design offers a smaller covered area in the sea, reducing exposure to environmental loads and promoting cost-effectiveness and efficiency in fish farming operations. The compact design not only minimizes environmental impact but also enhances structural stability and operational effectiveness by optimizing resource utilization. Overall, this study provides significant findings for constructing optimal fish farm layouts, improving their performance, and maximizing operational efficiency, ultimately contributing to better fish farming practices in open sea environments.

References

AKVA Group. (2023). 'Tubenet well received in the market'. Retrieved June 10, 2023, from https://www.akvagroup.com/blog/tubenet-well-received-in-the-market

Antonutti, R., Peyrard, C., Incecik, A., Ingram, D., & Johanning, L. (2018). Dynamic mooring simulation with Code_Aster with application to a floating wind turbine. Ocean Engineering, 151, 366-377. https://doi.org/10.1016/j.oceaneng.2017.11.018

ASC-Aqua. (2023). What is aquaculture? Aquaculture Stewardship Council. Retrieved from May 26, 2023, https://asc-aqua.org/learn-about-seafood-farming/what-is-aquaculture/

Bergheim, A. (2012). Recent growth trends and challenges in the Norwegian aquaculture industry. Latin American Journal of Aquatic Research, 40(3), 800-807. https://doi.org/10.3856/vol40-issue3-fulltext-26

Bi, C. W., & Xu, T. J. (2018). Numerical study on the flow field around a fish farm in tidal current. Turkish Journal of Fisheries and Aquatic Sciences, 18, 705-716.

Blevins, R. D. (2001). Flow-Induced Vibration. Krieger Publishing Company, Malabar, United States.

Bugrov, L. Y. (2006). The SADCO underwater fish-farming system. Underwater Technology & Ocean World, 1, 34-45.

Çengel, Y. A., and Cimbala, J. M. (2010). Fluid mechanics: Fundamentals and applications. McGraw-Hill Education, Singapore.

Cardia, F., & Lovatelli, A. (2015). Aquaculture Operations in Floating HDPE Cages: A Field Handbook. FAO and Ministry of Agriculture of the Kingdom of Saudi Arabia.

Chen, H., & Christensen, E. D. (2016). Investigations on the porous resistance coefficients for fishing net structures. Journal of Fluids and Structures, 65, 76-107.

Chen, H., & Christensen, E. D. (2017). Development of a numerical model for fluid-structure interaction analysis of flow through and around an aquaculture net cage. Ocean Engineering, 142, 597-615.

Cheng, H. (2017). Study on the Anti-current Characteristics of a New Type Gravity Fish Cage and Design Optimising (Master Thesis). Ocean University of China, Qingdao, China.

Cheng, H., Aydemir, O., & Ong, M.C. (2023). Wake effects on the drag force estimation of downstream fish cages. (OMAE2023)

Cheng, H., Huang, L., Ni, Y., Xu, Q., Zhao, F., Wang, X., & Liang, Z. (2018). Numerical and Experimental Study of SPM Fish Cage: Comparison and Validation. In Volume 7B: Ocean Engineering, V07BT06A053. ASME. https://doi.org/10.1115/OMAE2018-78204

Cheng, H., Li, L., & Ong, M. C. (2022). Comparative study of five commonly used gravity-type fish cages under pure current conditions. Ocean Engineering, 250, 110977.

Cheng, H., Li, L., Aarsæther, K. G., & Ong, M. C. (2020). Typical hydrodynamic models for aquaculture nets: a comparative study under pure current conditions. Aquacultural Engineering, 90, 102070. https://doi.org/10.1016/j.aquaeng.2020.102070

Cheng, H., Ong, M. C., Li, L., & Chen, H. (2022). Development of a coupling algorithm for fluid-structure interaction analysis of submerged aquaculture nets. Ocean Engineering, 243, 110208.

DeCew, J., Tsukrov, I., Risso, A., Swift, M. R., & Celikkol, B. (2010). Modelling of dynamic behavior of a single-point moored submersible fish cage under currents. Aquacultural Engineering, 43, 38-45. https://doi.org/10.1016/j.aquaeng.2010.05.002

Earthjournalism network. (2014, April 18). Environmental problems of aquaculture. Retrieved May 26, 2023, from https://earthjournalism.net/resources/environmental-problems-of-aquaculture

Endresen, P. C., Føre, M., Fredheim, A., Kristiansen, D., & Enerhaug, B. (2013). Numerical modeling of wake effect on aquaculture nets. In Proceedings of the ASME 2013 32nd International Conference on Ocean, Offshore and Arctic Engineering, OMAE2013-11446.

Ernst & Young AS. (2019). The Norwegian Aquaculture Analysis 2019. Accessed 10 June 2020, from https://www.ey.com/no.

Food and Agriculture Organization of the United Nations (FAO). (2018). Achieving Blue Growth. Building vibrant fisheries and aquaculture communities. Retrieved from http://www.fao.org/3/CA0268EN/ca0268en.pdf

Food and Agriculture Organization of the United Nations (FAO). (2022). The State of World Fisheries and Aquaculture 2022. Retrieved from https://www.fao.org/3/cc0461en/cc0461en.pdf.

Fredheim, A. (2005). Current forces on net structures (PhD thesis). NTNU, Trondheim, Norway.

Fridman, A. L. (1973). Theory and Design of Commercial Fishing Gear. Israel Program for Scientific Translations.

Gansel, L. C., McClimans, T. A., & Myrhaug, D. (2012). The Effects of Fish Cages on Ambient Currents. ASME Journal of Offshore Mechanics and Arctic Engineering, 134(1), 011303.

Halwart, M., Soto, D., & Arthur, J. R. (Eds.). (2007). Cage Aquaculture: Regional Reviews and Global Overview (FAO Fisheries Technical Paper). FAO, Rome. http://www.fao.org/docrep/pdf/010/a1290e/a1290e.pdf

Keith, H. G. and James, D., 2023. "Offshore aquaculture project underway in Hawaii," earthsky.org, posted 19 Oct 2011, Accessed 10 June 2023, https://earthsky.org/human-world/offshore-aquaculture-projectunderway-in-hawaii.

Knysh, A., Coyle, J., DeCew, J., Drach, A., Swift, M. R., & Tsukrov, I. (2021). Floating protective barriers: evaluation of seaworthiness through physical testing, numerical simulations and field deployment. Ocean Engineering, 227, 108707. https://doi.org/10.1016/j.oceaneng.2021.108707

Kristiansen, T., & Faltinsen, O. M. (2012). Modelling of current loads on aquaculture net cages. Journal of Fluids and Structures, 34, 218-235.

Lekang, O.-I. (2019). Aquaculture Engineering (3rd ed.). Wiley-Blackwell, Hoboken.

Li, L., Jiang, Z., Høiland, A. V., & Ong, M. C. (2018). Numerical analysis of a vessel-shaped offshore fish farm. Journal of Offshore Mechanics and Arctic Engineering, 140, 041201.

Løland, G. (1991). Current forces on and flow through fish farms (PhD thesis). NTNU, Trondheim, Norway.

Loverich, G. F., & Gace, L. (1998). The effect of currents and waves on several classes of offshore sea cages. In Charting the future of ocean farming (pp. 131-144).

Max Roser, Hannah Ritchie, Esteban Ortiz-Ospina, & Lucas Rodés-Guirao. (2013). World Population Growth. Retrieved from: https://ourworldindata.org/world-population-growth

Menter, F. R. (1992). Performance of popular turbulence models for attached and separated adverse pressure gradient flows. AIAA Journal, 30. DOI: 10.2514/3.11180

Menter, F. R. (1997). Eddy viscosity transport equations and their relation to the k-e model. Journal of Fluids Engineering, 119(4), 876-884. DOI: 10.1115/1.2819511

Menter, F. R., Kuntz, M., & Langtry, R. (2003). Ten years of industrial experience with the SST turbulence model. Heat and Mass Transfer, 4.

Moe-Føre, H., Endresen, P. C., Aarsæ ther, K. G., Jensen, J., Føre, M., Kristiansen, D., Fredheim, A., Lader, P., and Reite, K. (2015). Structural Analysis of Aquaculture Nets: Comparison and Validation of Different Numerical Modeling Approaches. Journal of Offshore Mechanics and Arctic Engineering, 137, 041201.

Morison, J. R., O'Brian, M. P., Johnson, J. W., and Schaaf, S. A. (1950). The force exerted by surface waves on piles. Journal of Petroleum Technology, 2, 149-154.

Nordlaks, 2023. "The Ocean Farm "Jostein Albert"," Nordlaks, Accessed 10 June 2023, https://www.nordlaks.no/en/havfarmen-jostein-albert/

NS 9415.E Marine Fish Farms—Requirements for Design. Dimensioning, Production, Installation and Operation. Standards Norway.

https://handle.standard.no/en/webshop/search/?search=ns9415

Okereke, M., & Keates, S. (2018). Finite element applications: a practical guide to the FEM process.

Overton, K., Dempster, T., Oppedal, F., Kristiansen, T. S., Gismervik, K., & Stien, L. H. (2019). Salmon lice treatments and salmon mortality in Norwegian aquaculture: A review. Reviews in Aquaculture, 11(4), 1398-1417. https://doi.org/10.1111/raq.12299

Patursson, Ø. (2008). Flow through and around Fish Farming Nets (Doctoral Thesis). University of New Hampshire, USA. https://scholars.unh.edu/dissertation/434

Patursson, Ø., Swift, M. R., Tsukrov, I., Simonsen, K., Baldwin, K., Fredriksson, D. W., & Celikkol, B. (2010). Development of a porous media model with application to flow through and around a net panel. Ocean Engineering, 37, 314-324.

RefaMed, 2023. "Fish farming technology for the open seas," Exhibition catalogue, Accessed 10 June 2023, https://refamed.com/gabbie_mare/tlc_system.html

Ryan, J. (2004). Farming the deep blue. Bord Iassaigh Mhara and Irish Marine Institue, Ireland.

Schlichting, H. (1979). Boundary-Layer Theory. Mcgraw-hill book company, New York, United States.

Scott, D. C. B. and Muir, J. F., 2000. “Offshore cage systems: A practical overview,” Option Mediterraneennes-International Centre for Advanced Mediterranean Agronomic Studies, p. 79-89.

Shainee, M., Leira, B. J., Ellingsen, H., & Fredheim, A. (2013). An Optimum Design Concept for Offshore Cage Culture. Presented at the ASME 2012 31st International Conference on Ocean, Offshore and Arctic Engineering, American Society of Mechanical Engineers Digital Collection, pp. 85–93. https://doi.org/10.1115/OMAE2012-83601

Shen, Y., Greco, M., Faltinsen, O. M., & Nygaard, I. (2018). Numerical and experimental investigations on mooring loads of a marine fish farm in waves and current. Journal of Fluids and Structures, 79, 115-136. https://doi.org/10.1016/j.jfluidstructs.2018.02.004

Sim, J., Cheng, H., Aarsæther, K. G., Li, L., and Ong, M. C. (2021). Numerical investigation on the cage-to-cage wake effect: a case study of a 4 × 2 cage array. Journal of Offshore Mechanics and Arctic Engineering, 143, 051301.

Skretting. (2023). Why is aquaculture important? Retrieved May 26, 2023, from https://www.skretting.com/en/transparency--trust/faqs/why-is-aquaculture-important/

Soto, D., & Brugere, C. (2008). The Challenges of Climate Change for Aquaculture. Retrieved from https://www.fao.org/3/i0305e/i0305e16.pdf

Sumer, B. M., and Fredsøe, J. (2006). Hydrodynamics around cylindrical structures. World Scientific Publishing, Singapore.

Tacon, A. G., and Halwart, M. (2007). Cage aquaculture: a global overview. FAO Fisheries Technical Paper. No. 498, Rome, Italy.

Tang, H. J., Yang, R. Y., and Huang, C. C. (2019). Numerical modelling of the mooring line failure induced performance changes of a marine fish cage in irregular waves and currents. In Proceedings of the ASME 2019 38th International Conference on Ocean, Offshore and Arctic Engineering, OMAE2019-95730.

The Nature Conservancy. (2017). The Aquaculture Opportunity. Retrieved from https://www.nature.org/en-us/what-we-do/our-insights/perspectives/the-aquaculture-opportunity/

The Ocean Foundation. (2022). Sustainable Aquaculture. Retrieved from https://oceanfdn.org/sustainable-aquaculture/

Tsarau, A., and Kristiansen, D. (2019). Application of Fhsim for the analysis of environmental loads on a complete fish-farm system. In VIII International Conference on Computational Methods in Marine Engineering, p. 271-284.

Tsukrov, I., Eroshkin, O., Fredriksson, D., Swift, M. R., & Celikkol, B. (2003). Finite element modelling of net panels using a consistent net element. Ocean Engineering, 30, 251–270. https://doi.org/10.1016/S0029-8018(02)00021-5

Turner, A. A., Jeans, T. L., & Reid, G. K. (2016). Experimental investigation of fish farm hydrodynamics on 1:15 scale model square aquaculture cages. Journal of Offshore Mechanics and Arctic Engineering, 138, 061201.

White, F. M. (1974). Viscous fluid flow. McGraw-Hill.

Wilcox, D. (1994). Simulation of transition with a two-equation turbulence model. AIAA Journal, 32, 247-255. DOI: 10.2514/3.59994

Wilcox, D. C. (1988). Reassessment of the scale-determining equation for advanced turbulence models. AIAA Journal, 26, 1299-1310. DOI: 10.2514/3.10041

Zdravkovich, M. M. (1997). Flow around circular cylinders Vol 1: Fundamentals. Oxford Science Publications, New York, United States.

Zhao, Y., Bi, C., Dong, G., Gui, F., Cui, Y., and Xu, T. (2013). Numerical simulation of the flow field inside and around gravity cages. Aquacultural Engineering, 52, 1-13.

Zhao, Y.-P., Li, Y.-C., Dong, G.-H., Gui, F.-K., & Teng, B. (2007). Numerical simulation of the effects of structure size ratio and mesh type on three-dimensional deformation of the fishing-net gravity cage in current. Aquacultural Engineering, 36(3), 285-301. https://doi.org/10.1016/j.aquaeng.2007.01.003